Hard Science – Doctoral School "B. Telesio" - XXII cycle

Science and Technologies in Mesophases and Molecular Materials STM^3

Settore disciplinare di afferenza: FIS07

PhD Thesis – 2009

"Mechanical properties of biopolymers studied at mesoscopic-scale with advanced optical techniques."

by Lara Selvaggi

Supervisor: Prof. R. Bartolino

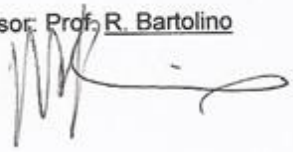

Coordinator: Prof. C. Versace

Tutors: Prof. A. Sasso, Dr. D. Cojoc, Dr. B. Zappone

Acknowledgment

I would like to first express my gratitude to my Professor A. Sasso for guiding me through my research in these years. His methodical approach and his valuable lessons for the future have given me an academic formation.

I thank my supervisor, Professor R. Bartolino, for his helpfulness and valuable advice I received through the course of my thesis.

I thank Dr. Dan Cojoc for the motivating discussions and the time spent in his laboartory in Trieste and Prof. Giacinto Scoles to welcome me in Trieste.

I would like to thank the members of the laboratory in Naples and Cosenza for their continuous presence in my experiments and the people in the TASC group for providing a great atmosphere in the office. I am specially indebted to Dr. Enrico Ferrari for countless exchange views and for his help and lessons in the laboratory. I also thank Dr. Giuseppe Pesce for tutoring me especially during my first steps in the laboratory of Naples and Dr. Bruno Zappone for his help during my work in the laboratory of Cosenza.

I would like to thank Dr. L. Santella, of Neapolitan zoological station “Anthon Dohrn”, for starfish oocytes supply and microinjection teaching and Dr. R. Carotenuto, of Biology Department in Federico II, for frog oocytes supply.

A special thank to Dr. Robson for his great help to correct my English in this thesis. Also you should thank him because he made this thesis more fluently and pleasant to reading!

Far from home, in Trieste, I received support from my lovable grandmother, aunt and cousins: thank you!

Finally I would like to express my gratitude and affection to my parents, my brother, my two little nieces and their mother. My brother is always present with his love and advice.

I dedicate this thesis to my unique mom and exceptional dad for their endless and unstinted support.

A special thanks is to my future adorable husband that has accompanied me everywhere and has given me force in any event.

“Three Rules of Work: out of clutter find simplicity; from discord find harmony; in the middle of difficulty lies opportunity.”

Albert Einstein

Table of Contents

Introduction

This thesis describes how optical techniques can be applied in a wide variety of biological investigations. They can be useful, for example, for cellular imaging function, mechanical properties of living cell study, protein filament structure analysis and biochemical characterization. This thesis reports results obtained in three different areas, chronologically followed one after the other:

1. microrheology in living cells;
2. multi-trapping by means of holographic techniques;
3. atomic force microscopy in biological protein.

Each of these areas has been investigated in different laboratories located next to scientific institutes:

1. University “Federico II” of Naples in collaboration with the Zoological Station “Anthon Dohrn” (Microrheology investigation in living starfish oocytes using Multiple-Particle-Tracking technique);
2. TASC laboratories of Trieste (Holographic diffractive-optical-elements to realize multi-optical-traps for red blood cells investigation and preliminary tomography application);
3. University of Calabria (Atomic Force Microscope to study gliadins filaments structure).

Each chapter reports the materials used and the sample preparation procedure, introduces the technique, gives information about the method and the setup developed for each experiment and reports the results. The third area about protein investigation is resumed in Appendix A.

1 Microrheology in living cells

Cells continuously adapt to changing conditions by transport molecules and signaling through intracellular regions with differing material properties, such as variation in viscosity and elasticity. To determine the contribution of local variation on cell structure and physiology, microrheology techniques are used. Microrheology describes how materials store and dissipate mechanical energy as a function of length scale. Complex fluids like mayonnaise, complex materials like plastics, and biomaterials like cells are viscoelastic systems so they can act both like fluids and like solids, depending on how forces are applied on them. Microrheology can describe the combined viscous and elastic properties of these materials. Whereas in macroscopic rheology stress-strain relationship are measured through mechanical deformation of bulk materials, in microrheology embedded probe motion is tracked and its relationship to the local environment inferred. Only small amounts of sample are required for this technique unlike conventional rheology which needs several milliliters of substance.

Initially, microrheology was used for the analysis of uniform complex fluids but an important challenge was to investigate materials containing structures heterogeneous in nature: they are structured on a range of length scales greater than that of their molecular arrangement. Investigations in the intracellular environment, which is far from an homogeneous mixture, are helpful to assess and interpret the dynamic local mechanical properties of cells, which impact all trafficking and communication processes that coordinate functional responses. Microrheology can be used in vivo for linking mechanical and structural characteristics of a cell with its biochemical properties. Cellular microrheology clarifies the concept of regional and integrated properties, structures, and transport in live cells.

Materials

1.1 Living cells as sample

A look at a living cell through the microscope reveals a constant traffic of small components like phospholipids vesicles and organelles, Fig.1. This traffic reflects the activity of intracellular transport networks. The internal microenvironments of cells are a complex, heterogeneous combination of flexible cytoskeleton macromolecules and viscous liquid containing small molecules, ions, molecular complexes and organelles (Luby-Phelps, 2000): one *ml* of cytoplasm may contain about 400 *mg* of proteins, lipids, nucleic acids and sugars (Guigas, 2007).

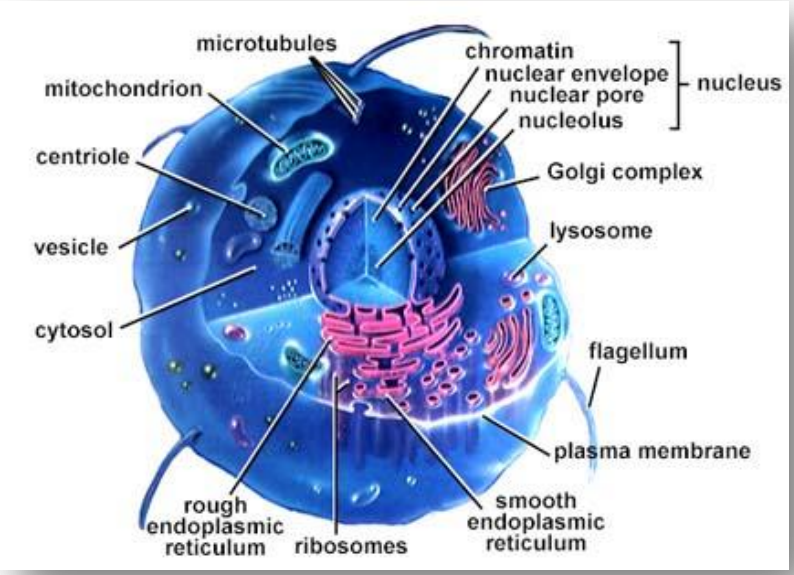

Fig. 1 Eukaryotic cell composition.

Cells continually remodel their internal structure, they crawl, change shape and divide, and thereby modify their mechanical properties. This constant adaptation requires the transport of molecules and signaling through intracellular regions with differing material properties, such as variation in viscosity or elasticity. To elucidate the dynamic and functional role of a cell it is essential to understand its material properties. Many experimental techniques show that cells have both elastic and viscous characteristics. A highly deformed but intact cell does not return to its origi-

nal shape, since energy has been expended on rearranging the cytoskeleton and other molecules. The extent of the elastic energy storage and viscous energy dissipation define the elastic and viscous components of the cell response, respectively (Weihs, 2006). Unlike most conventional materials, cells are highly nonlinear; their elastic behaviour depends on the mechanical properties of their environment (Jiang, 2006). Cells rely on components, such as the nucleus, mitochondria, Golgi and ribosomes, and perform tasks required for survival and adaptation in changing conditions. The intracellular environment is bounded by flexible plasma membrane and is organized into locally distinct collections of molecules and structures within a dynamic, filamentous cytoskeleton scaffold. The presence of membrane-bounded subcompartments confers an intrinsic inhomogeneity on the interior of a cell.

The cytoskeleton is the structure most responsible for the mechanical properties of the cell. It is a network of self-assembling polymeric protein fibers: microfilaments (F-actin), intermediate filaments and microtubules (Karen, 2007), Fig.2. Microfilaments are polymers 8 *nm* in diameter formed from the globular protein actin. Actin is very abundant in most cells, with a concentration of 4 *mg/ml* in a typical eukaryotic cell (Bray, 1975). Actin is the component of the cytoskeleton system that allows movement of cells and cellular processes. It works in conjunction or in tandem with other components of the system. Microtubules are polymers of the related globular proteins $\alpha-$ and $\beta-$tubulin. The sub-units self-assemble to form a rigid tube 25 *nm* in diameter. There are typically about 150 microtubules in a tissue culture cell and each is 50 to 100 μm in length (Hiller, 1978). They move vesicles, granules, organelles like mitochondria, and chromosomes via special attachment proteins. They also play a cytoskeleton role. Intermediate filaments are highly stable polymers of a broad family that includes vimentin, the cytokeratins, and the neurofilaments (Chou, 1997). The concentration of vimentin in a mammalian tissue culture cell is on the order of 150 $\mu g/ml.$ They may stabilize organelles, like the nucleus, or they may be involved in specialized junctions.

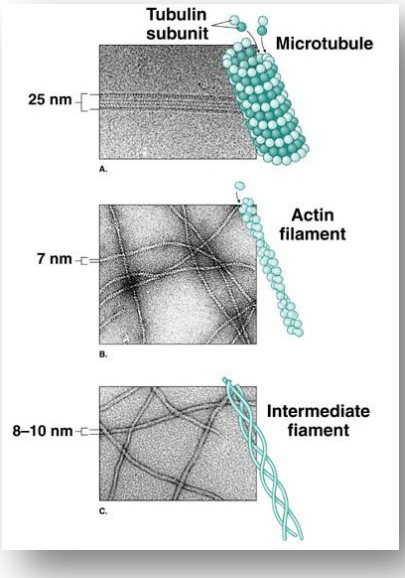

Fig. 2 Major protein filaments present in a eukaryotic cell.

All these three types of cytoskeleton filaments are physically interconnected and specific proteins regulate the length and total content of filaments or stabilize bundles by cross-linking one filament type to another. These proteins are presumed to be the immediate effectors of signal-initiated reorganization of the cytoskeleton. Moreover, individual cytoskeleton filaments are not isotropically distributed within the network: microfilaments form bundles known as stress fibers and the ends of the bundles are often fixed at specific sites; microtubules radiate from an organizing center, or centrosome, usually located near the cell nucleus; and intermediate filaments are often collinear with these microtubules, especially in the more peripheral regions of the cell. The inhomogeneities contributed by the cytoskeleton vary temporally as well as spatially. The assembly state and sub cellular distribution of all three types of cytoskeleton filaments are physiologically regulated. Well known examples of this include the disassembly of the radial array of microtubules and subsequent assembly of the microtubules spindle during mitosis as well as the reorganization of the actin cytoskeleton in response to growth factor stimulation (Luby-Phelps, 2000). Measurements of the mechanical behaviour of cells probe the contribution of constituent components to cell mechanics. Interest in the study of cell mechanical properties is presently increasing (Wang, 2008) although complexity and heterogeneity of cell structure, as well as its dynamics, complicate the investigation of viscoelastic responses inside it.

1.2 Starfish oocytes

Starfish eggs are stored in the ovary as immature oocytes that are arrested at the meiotic prophase. Maturation of starfish oocytes is reinitiated under hormonal stimulation and the oocytes become fertilizable. Starfish oocytes represent an attractive model system for investigating mechanical properties because they are transparent and large enough to allow both the observation of cell content and the microinjection of probes inside them. The fully grown immature oocytes have a spherical shape and are about 150-180 μ*m* in diameter. They contain a large clear germinal vesicle (GV), eccentrically situated, that measures about 50-80 μ*m* in diameter and contains a prominent nucleolus, Fig.3.

Fig. 3 Immature starfish oocyte.

Oocyte cortex, focused by Nomarski microscope, contains a layer of clear vacuoles ~2 μ*m* in diameter with smaller cortical granules interspersed among the vacuoles. Other organelles appear uniformly distributed throughout the remaining cytoplasm. Immature oocytes are surrounded by a single layer of follicle cells; with about 25 to 75 follicle cells associated with each oocyte. A follicle cell is less than 0.5 μ*m* thick. Follicle cells are separated 10-15 μ*m* from the oocyte surface by the jelly coat layer which appears like a tangled mat of fine fibres in Nomarski microscopy (Schroeder, 1983). In this study, ovaries containing prophase I arrested oocytes (immature oocytes) are removed from *Astropecten aranciacus* (*A.a.*) starfish (Fig.4A), by cutting an arm, and dipped in seawater. Oocytes dissected from ovaries by filtration process are washed in filtered artificial seawater (ASW: 500 *mM* NaCl, 8 *mM* KCl, 10 *mM* CaCl2, 12 *mM* MgCl2, 2.5 *mM* NaHCO3, titrated to pH 8.0 with

NaOH) and stored at 16°C for 40-50 *min* before use. *A.a.* starfishes live on sandy ground at a depth of around 20 *m* in the Gulf of Naples; its oocytes are collected in February-April. Oocytes are produced in the animal for only a few months per year and the ovulation period depends on the species. To avoid stopping experiments also oocytes collected from *Asterina pectinifera* (*A.p.*) starfish (Fig.4B) during the breeding season in September-October are also used. This starfish specie lives on stony ground at a depth of a few meters in the Sea of Japan. Both oocytes types are suitable for follow mechanical and morphological transformations that occur during hormone-induced maturation.

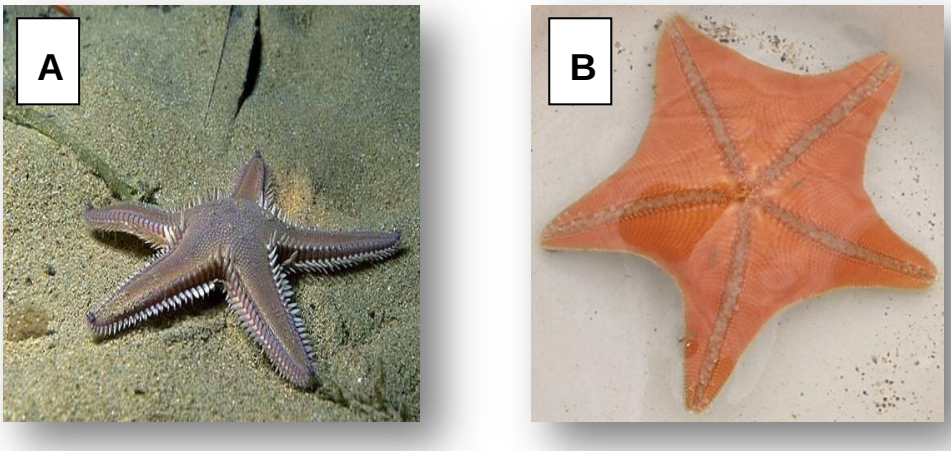

Fig. 4 A) Astropecten aranciacus starfish B) Asterina Pectinifera starfish.

1.2.1 Home-made sample chambers for starfish oocytes

Fully grown and spherical immature oocytes are selected by means of stereomicroscope and maintained in running seawater at 16°C. Oocytes are left in a Petri dish for about one hour before being gently placed in another chamber to start microinjection. Unlike other experiments with living cells (Yamada, 2000) (Tseng, 2002), we cannot incubate cells for long periods, since oocytes extracted from starfish ovaries survive only 7-8 hours. Two different chambers are used for microinjection and analysis, respectively. For microinjection, about 20 oocytes are moved into a home-made chamber, called in future *chamber* (Fig.5), composed of one square coverslip (22X22 *mm* No.1 thickness) and a little (10x3 *mm*) rectangular-shaped piece of glass linked to each other by wax to form a 45° angle, Fig.5. This angle is necessary to house oocytes without damage and to stop them during microinjection.

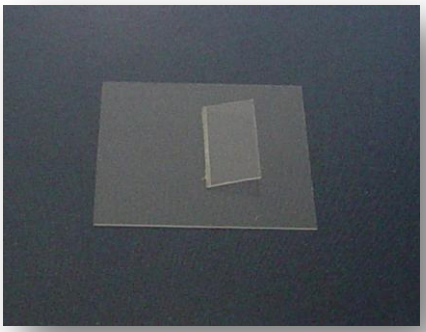

Fig. 5 Chamber for microinjection.

After microinjection cells are removed from the *chamber* and allocated to another home-made chamber, called in future just *Petri-chamber*, Fig.6. It consists of a Petri with a hole in the middle that is closed using a square coverslip (22X22 *mm*). Inside this coverslip is a double layer of sticky-tape, 200 μm thick, that glues a little (5x5 *mm*) square-shaped piece of glass. The edge of this glass slightly protrudes out of the sticky-tape to take oocytes under it. This *Petri chamber* houses immature oocytes immersed in about 1 *ml* of seawater. It is an helpful way to avoid cell movements during acquisition and in particular during hormone addition.

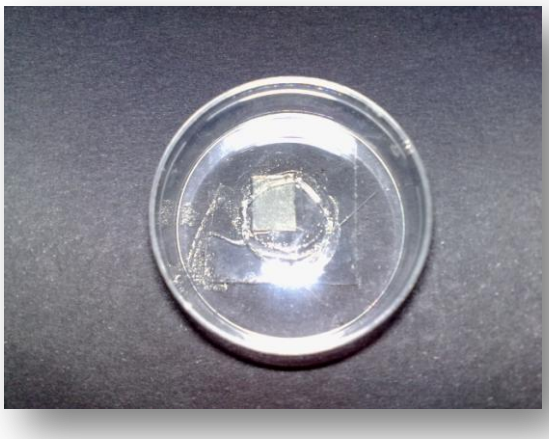

Fig. 6 "Petri chamber" for analysis.

1.2.2 Maturation in starfish oocytes

Prophase-arrested oocytes when removed from starfish ovaries are metabolically quiescent; in response to a maturation-inducing hormone, oocytes resume

meiosis and undergo nuclear disassembly in a process referred to as germinal vesicle breakdown (GVBD), Fig.7. Due to the high cell cycle synchrony and the rapid hormone response, starfish oocytes provide an excellent model for the study of cellular activation. GVBD begins about 50 *min* after hormone treatment; its onset is signaled by the breakdown of the nuclear envelope. Nuclear envelope disassembly can be recognized by the more irregular nature of nuclear periphery. At 75-80 *min* after hormone addition the cytoplasm is well blended with nucleus content, the nucleoplasm, and GVBD is considered complete (Stricker, 1991).

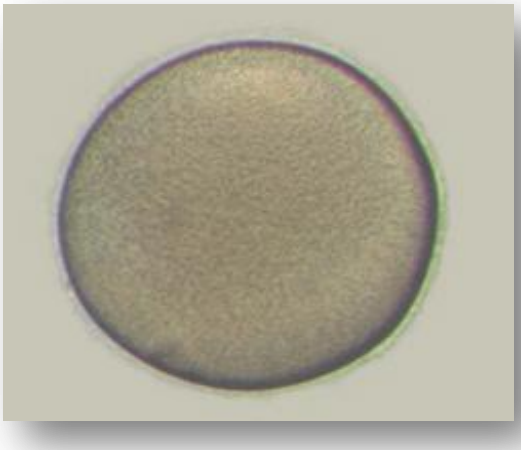

Fig. 7 Mature starfish oocytes.

In this experiment oocyte maturation is promoted by adding 10 *µl* of 1-MA (Sigma Chemical Co., St. Louis, MO) to a Petri dish housing immature oocytes and 1 *ml* filtered sea water. During maturation a reorganization of all cell content occurs and large movements of all oocyte constituent can be observed. Scanning Electron Microscopy and Immune Fluorescence Microscopy have established that 1-MA immediately stimulates the transient appearance of prominent microvilli on the oocyte surface caused by the rapid assembly and disassembly of the filamentous actin bundles in their inner cores (Schroeder, 1983) (Schroeder, 1981) (Otto, 1984). This is a fast response that occurs within 1 *min* after the addition of 1-MA. An equally rapid change in response to 1-MA is the quick release of intracellular Ca^{2+} in the cytoplasm and the nucleus (Santella, 1994). Following these early events, 1-MA then induces more extensive reorganization of cytoplasm actin network and drastic changes in the phosphorylation state of numerous proteins (Labbè, 1989) (Masui, 2001) (Prigent, 2004). In parallel, intracellular organelles such as the endoplasmic

reticulum (ER) undergo structural changes (Jaffe, 1994) (Terasaki, 1994).The chaotic motion inside oocytes during maturation prevents any acquisition. All measurements on mature oocytes are performed at least one hour after the hormone addition, when the GVBD is concluding.

1.2.3 Endogenous grains and micro-particles as probes

The motions of appropriately sized probes embedded within cells provide an evaluation of the local, non-bulk, viscoelastic properties of heterogeneous cellular regions. The choice of particles or organelles as probes must proceed with rigor. The organelle approach is usually more qualitative as to size and rigidity; moreover optical properties of probes are undefined. The advantage of endogenous particles as probes is that no cell microinjection or deformations are needed; completely non invasive measurements of cell mechanics can be obtained. On the contrary, the drawback of endogenous granules over injected beads is that the first must be spherical and rigid like beads to satisfy Stoke's law. Usually, endogenous particles are lipid storage granules with spherical shape, about 300-500 *nm* in diameter, and are present in many cell types. For example, COS7 cells are rich with highly refractive granules just like polystyrene particles and transmission electron images show that these granules are also spherical. Yamada et al. demonstrated the appropriateness of endogenous granules as probes by suspending polystyrene beads and granules partially purified from COS7 cells into the same gelatin solution. They used fluorescent beads to identify particles. From their laser-tracking results it is impossible to distinguish lipid-storage granules from polystyrene beads; both types of particles give identical viscoelastic spectra for gelatin (Yamada, 2000).

1.2.4 Particles size and surface chemistry

In microrheology and microstructure characterization, the size of the probe particles is the length scale at which the material is probed. If chemical interactions between tracers and polymers are negligible, it is possible to characterize tracer motions based only on probe size relative to the native structural sizes of the network. Varying probe diameter with respect to these native lengths gives qualitatively different information about network mechanics. Thus, the choice of the particles that will serve as probes is critical and must be made carefully. A high level of monodispersity (coefficient of variation less than 5%) is essential because the dynamics of Brownian probes, and hence the displacements, depends on their radius, on the time scale of observation and on the mechanical nature of the probed material. In

general, the amplitude of the tracer motion is inversely proportional to the material's stiffness: bigger probes exhibit slower dynamics and for a given time scale of observation, undergo smaller displacements. Moreover, the generalized Stoke's Einstein relation, derived in section 1.6.1, is valid only if the particles move in a continuum. This means that any structural changes in the material must be occur at a length scale much smaller than the probes' diameters. So particle size must be chosen according to the mesh-size of the medium in which it is embedded. In fact, as shown in Fig.8, for chemically inert particles of radius *a* >> network mesh-size ε, bead motion is related to the linear viscoelastic response of the medium in which particles move. For particles resistant to protein adsorption with *a* << ε, bead motion does not reflect bulk viscoelasticity but is sensitive to solvent viscosity. Finally, for sticky particles that adsorb protein with *a*<< ε, bead movement reflects network fluctuations. So the ability to characterize and modify surface interactions, as well as tracer size, is crucial for the interpretation of complex biomaterials.

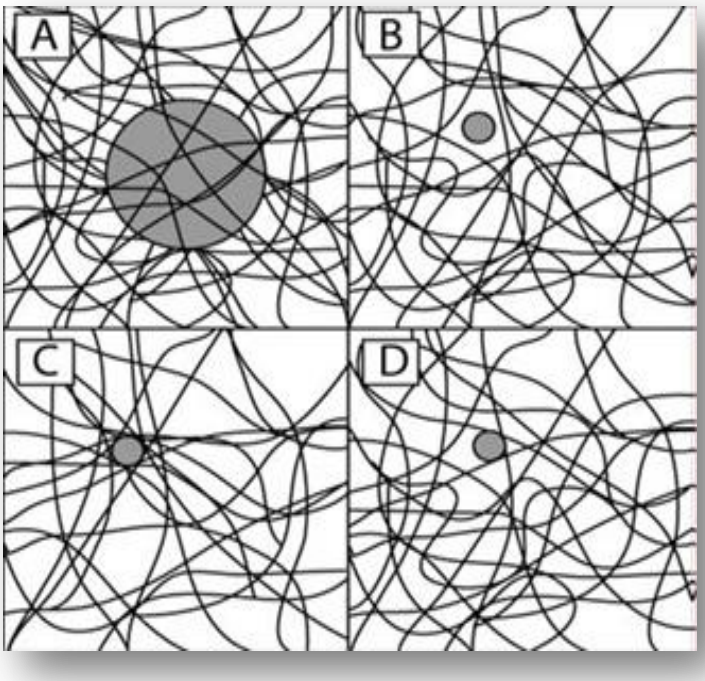

Fig. 8 How particle size and surface chemistry affect network mechanics. A) α>>ε implies that MSD is related to the linear viscoelastic response for chemically inert particles; B) α<<ε, for beads resistant to protein adsorption, implies that MSD is sensitive to the viscosity of the solvent but does not reflect the bulk viscoelasticity; C) α<<ε, for sticky beads that adsorb protein, implies that the bead movement reflects network fluctuations; D) α<<ε, for beads that adsorb a small amount of protein, leads to hydrodynamic interaction with the adsorbed network which implies uncertainty in data interpretation.

Microinjection

For microrheology measurements of network viscoelasticity, the particles must not only be large in comparison with all structural length scales but must also be sufficiently resistant to protein adsorption to prevent the local modification of network architecture and introduction of small heterogeneities (Valentine, 2004). The range of particle size that can be used is also limited by other factors related to the technique. The size of the probe particles is limited in standard video microscopy to optical wavelengths (~0.5 μm), as this is the diffraction-limited resolution of an optical microscope. Fluorescent particles can be used to decrease the probe size (~0.1 μm). The minimum traceable particle size, for the charge-coupled device used in our setup, is 100 *nm* and the detection of small displacement is limited by the spatial resolution of the tracking technique. As discussed in section 1.4, the minimum displacement detectable with our setup is 15 *nm*. Commercialized microspheres are available in a wide variety of dyes, sizes, and surface chemistry. In this study, only red fluorescent particles (Duke Scientific Corporation, Palo Alto CA) diluted in water D_2O with a final concentration of 10^{12} *particles/ml* are used to perform Multiple Particle Tracking measurements. These particles are 400 *nm* in diameter. In a cell, the mesh-size of the cytoskeleton network is estimated to be of the order of several tens of nm (Tseng, 2002), hence smaller than the size of our probes.

The surface chemistry of the probe is an equally important parameter, and it has been the subject of several studies in the recent years (McGrath, 2000) (Valentine, 2004) (Chae, 2008). Polystyrene plain particles (PS) are naturally uncharged and hydrophobic, but it is possible to modify them with a variety of surface functionalization. Most common functions include carboxylate modification for which the particle surface is decorated with carboxyl groups COOH, resulting in hydrophilic and negatively charged probes at pH greater than 4 and uncharged below. Both PS and COOH particles have the ability to bind strongly to any molecule with hydrophobic character, including proteins, nucleic acids and many small biomolecules. Amine-modified probes are hydrophilic particles with positively charged amine groups NH_2 stable for pH below 9 at which the surface charge is not neutralized. Tseng et al., in a microrheology study that quantifies the local mechanical properties of living Swiss 3T3 fibroblasts cells, used two different functionalized particles, carboxylate (COOH) and amino (NH_2) beads, to investigate the surface chemistry effect. They found that amine-modified microspheres, injected in the cells, underwent a nonrandom motion with bursts of direction through the cytoplasm possibly due to coupling of the microspheres to microtubules motor proteins. These rapid unidirectional intracellular movements were absent using negatively charged particles and

the positively charged particles velocities were about 20 times higher than found with negatively charged particles (Tseng, 2002).

In this thesis several types of negatively charged micro-particles injected in living oocytes are tested. Carboxylate-modified (CLM), aldheyde-modified (ALM) and sulfate (S) coated particles are used to check possible effect of beads surface chemistry in starfish oocytes cytoplasm. Since the oocyte cellular pH is essentially neutral (~ 7.0), all functionalized particles do not change surface behavior. The choice of probes surface chemistry depends on material under study, but usually chemically inert particles with the least possible influence on the material properties are sought. It is also possible to use other functionalization such as coating of the probes with bovine serum albumin (BSA) protein, to reduce protein adsorption or decorating the particle with a layer of poly(ethylene glycol) (PEG), a hydrophilic and uncharged polymer, which blocks any available protein binding sites. The origin of protein resistance in PEG-coated surfaces is generally attributed to steric repulsion forces. PEG-coated beads possess hydrophilic and neutrally-charged surfaces that minimize protein adhesion by reducing hydrophobic or electrostatic interactions, so PEG-coated particles are sensitive to changes in viscosity and microstructure. In particular, PEG-coated beads adsorb significantly less protein than bare carboxylate-modified (CLM) spheres or probes coated with BSA (Valentine, 2004). Chae et al. investigated the dependence of F-actin microrheology on probe surface chemistry using diffusing wave microscopy. They found that polystyrene probes pre-adsorbed with BSA interact more weakly than plain polystyrene (PS) beads with the surrounding polymer network; in particular BSA reduces particle-actin adhesion over untreated probes (Chae, 2008). To investigate the effect of surface chemistry on actin adsorption by polystyrene particles, McGrath et al. used polylysine-coated polystyrene particles (PLY-PS) to amplify actin binding and BSA to generate particles that would not adsorb actin. Moreover, they examined actin binding by bare CLM and silica beads and examined the role of surface charge using amino and plain polystyrene particles. With the exception of BSA-coated particles, all other beads adsorbed significant amounts of actin and at all frequencies. BSA particles report the lowest moduli among the chemistries studied, and PLY-PS particles report the highest moduli (McGrath, 2000). Recently, Wang et al. and Lai et al. have shown that PEG is a muco-resistant polymer. They used two different PEG molecular weights (MW) to functionalize polystyrene particles, PEG-2kDa and PEG-10kDa, and demonstrated that high MW PEG can increase muco-adhesion. Usually, uncoated polystyrene particles are muco-adhesive due to polyvalent hydrophobic interactions. Coating particles

with PEG-2kDa chains led to a greatly increased percentage of diffusive particles in contrast to PEG-10kDa, which exhibits muco-adhesive properties. PEG surface coverage is also fundamental for transport mode analysis; it depends on particle size, since a higher degree of curvature may require greater PEG coverage. Low coverage of 2-kDa PEG is inadequate to prevent hydrophobic interactions between the PS core and mucins, while higher surface PEG coverage blocks hydrophobic adhesive interactions. Thus, low PEG MW and high PEG surface coverage are both required for rapid mucus penetration of coated particles (Lai, 2007) (Wang, 2008). Finally, it is important to keep in mind that particles should be uniformly dispersed in the material to be probed. Depending on the interactions between the material and the probes, but also on the interparticle interactions, beads can form aggregates. It is usually possible to distinguish aggregates of two or more beads and to discard them from the tracking.

Theory and Methods

1.3 Microinjection

Microinjection is a useful way to introduce micro-probes into cells where phagocytes or endogenous particles like lipid granules, mitochondria and vesicles cannot be used. The microinjection setup consist of an optical microscope (Zeiss Axioskop) fitted with a Zeiss 10X microscope objective for both whole oocyte and glass tip observation; a lateral support (Narishige MO-155) that allows micrometric x-y-z movements of the holder, keeping the glass capillary for use with microinject particles; and an electronic or manual micro-injector, Fig.9.

Fig. 9 Microinjection setup.

The electronically micro-injector is a pneumatic system that requires only parameters setting like pressure and emission time. Instead, the manual micro-injector is like a syringe with a long plastic tube containing distilled water and ending in the holder. Syringe handle rotation permits regulation of water pressure inside the tube and consequently microinjection time and beads stream. This second system (Fig.10) requires a lot of experience, but the advantage is that moving the handle to increase (clockwise rotation) or reduce (counter clockwise rotation) pressure is possible to clear the glass tip from beads aggregates that usually create after glass tip breakdown.

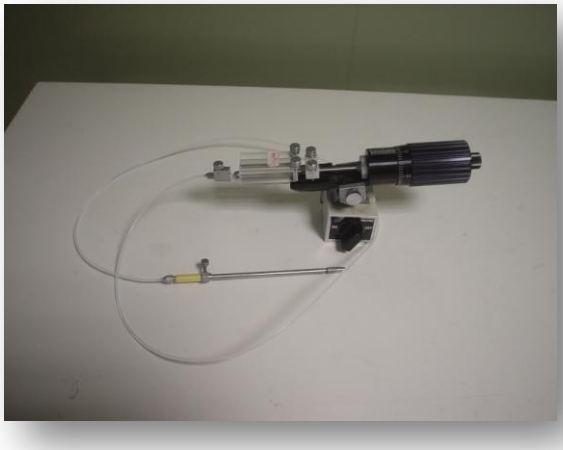

Fig. 10 Manual injector.

A cylindrical glass capillary (Fig.11), 0.87 *mm* inner diameter and 1 *mm* outer diameter, is mechanical stirred by means of a Puller. A solution of water and beads is used to load ¾ of the capillary. The ¼ remaining is filled with mineral oil to assure that distilled water from the holder cannot mix with the bead solution. After that, a glass capillary is loaded into the holder (Fig.12) and the tip is lightly broken by knocking it against a small piece of glass in the *chamber*. For this and for microinjection, it is necessary that the glass capillary and the oocytes are in the same field of view.

Fig. 11 Glass capillary.

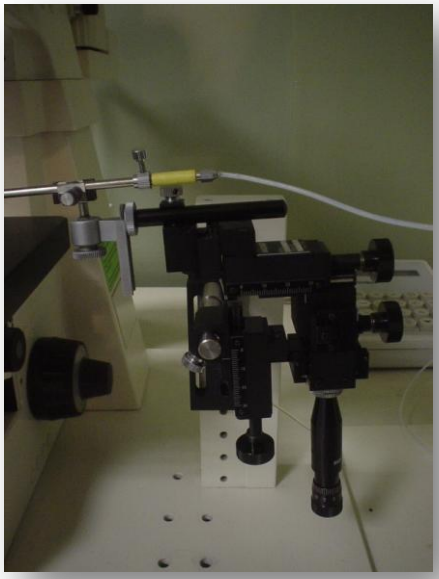

Fig. 12 Lateral support for microinjection.

When the tip starts penetration inside the oocyte membrane, and the cell is in working order, its membrane bends under tip pressure until the tip completely penetrates the cell (Fig.13A). At this time beads release occurs as fast as possible, and the tip is quickly removed to avoid cellular membrane injury. If any damage occurs the cellular membrane recovers its shape immediately. Microinjected particles can be observed in fluorescence in Fig.13B.

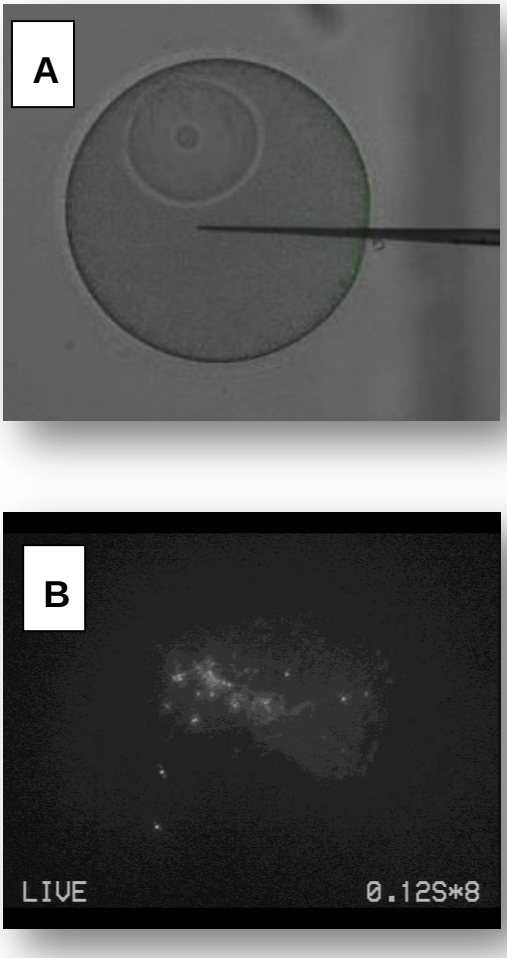

Fig. 13 A) Immature oocyte during microinjection B) Fluorescent particles microinjected inside an immature oocyte .

1.4 Brownian motion

In 1828 Robert Brown observed, through a microscope, the irregular motion of pollen grains suspended in water. It was not until Einstein's work in the early 1900s, however, that the origin of this irregular motion was found to be the result of collisions with molecules that were so small as to be invisible in a light microscope. Jean Perrin in 1908 was able to establish the validity of Einstein's equation by showing that the mean square displacement is proportional to time with a constant of proportionality that describes the frictional dissipation of the particles. The so-called Brownian motion thus appeared as the best candidate to experimentally checking the discontinuity of matter hypothesis. In a system at thermodynamic equilibrium where no external forces are applied, particles suspended in a liquid undergo translational

and rotational diffusion due to forces exerted by molecules in the surrounding medium (Einstain, 1956).

Particles diffuse freely through a liquid typically exhibiting a “random-walk” that is non-directional and characterized by a Gaussian distribution in step size (Weihs, 2006). This random walk is propelled by thermal fluctuations as the probe particles interact with cellular structures and the liquid surrounding them. If we observe such a particle for a time interval *t*, we will see it displaced by a position vector *r*. If we repeat this over and over again, we can compute the average displacement during time interval *t*, and as long as no other forces act, we should find that the average walk is zero, $< r^2 >= 0$. As can be seen in Fig.14, the motion of single particles appears to be random. Recording the Brownian motion of a particle in a complex fluid is possible to distinguish different situations: constrained motion (a), sub-diffusive motion (b), diffusive motion (c) and super-diffusive motion (d). In our experiments only sub-diffusive and pure diffusive motions have been analyzed. Even if few cases, constrained and super-diffusive particles motion have been discarded. In Fig.15B particle movements are recorded in a complex fluid, and for this reason the motion is more constrained, as can be seen at 10 *s* and 100 *s,* than the motion of a particle in a viscous fluid, Fig.15A.

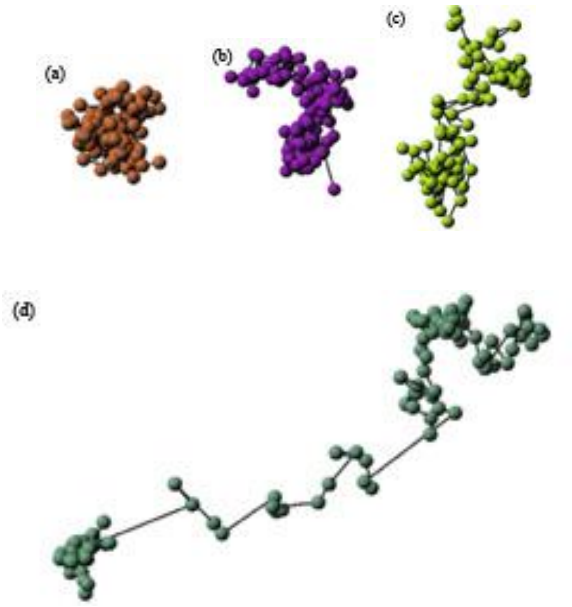

Fig. 14 Typical particle trajectories recorded with a 60X microscope objective in 100 s.

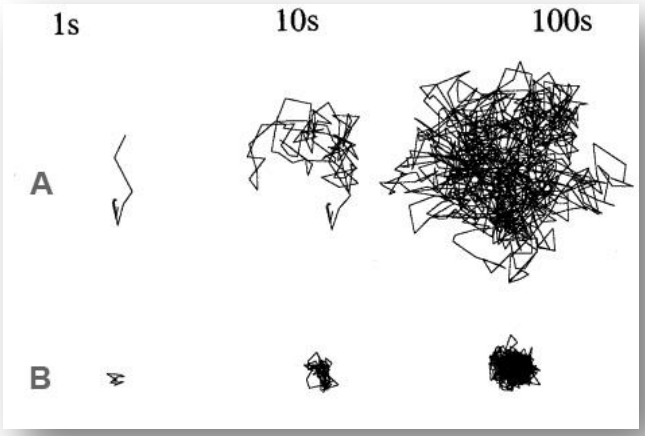

Fig. 15 Brownian trajectories: (A) in a pure viscous fluid and (B) in a viscoelastic fluid.

Tracking the Brownian motion of colloids was first done about a hundred years ago to demonstrate the molecular nature of matter. Today's scientists perform particle tracking experiments to assess the structural and mechanical properties of complex material at micron length scale.

1.5 Microrheology as rheology evolution

Rheology studies the viscoelasticity of materials. Microrheology extends this definition to consider how the dynamic behaviour of these materials changes with length scale. Rheology measurements quantify the bulk or average responses of liquids and flexible materials to deformation or mechanical forces. It has the advantage of being able to quantify how materials store and dissipate energy and thus directly relate to every day macroscopic observables. However, classical rheology equipment, even if miniaturized, cannot be used to probe the microenvironment within individual live cells because stresses are applied and responses are measured through mechanical fixtures that would have to be artificially inserted into a cell, thereby disrupting its structure (Weihs, 2006). The power of microrheology lies in the fact that individual tracer beads probe microenvironments and the motion of the individual tracer particles reflects the local mechanical response of the surrounding material (Valentine, 2001). This probing technique has received much interest in the last few decades due to the importance of a material's local properties in its function and in its macro-scale characteristics. These new assessments are especially relevant in soft matter sciences like biophysics.

Rheology is the study of the deformation and flow of a material in response to an applied stress, Fig.16. Simple solids store energy and provide an elastic response, whereas simple liquids dissipate energy through viscous flow. For more complex viscoelastic materials (polymers, colloids, and biological materials), rheological measurements reveal both the solid-like and fluid-like responses which generally depend on the time scale at which the sample is excited (Larson, 1999).

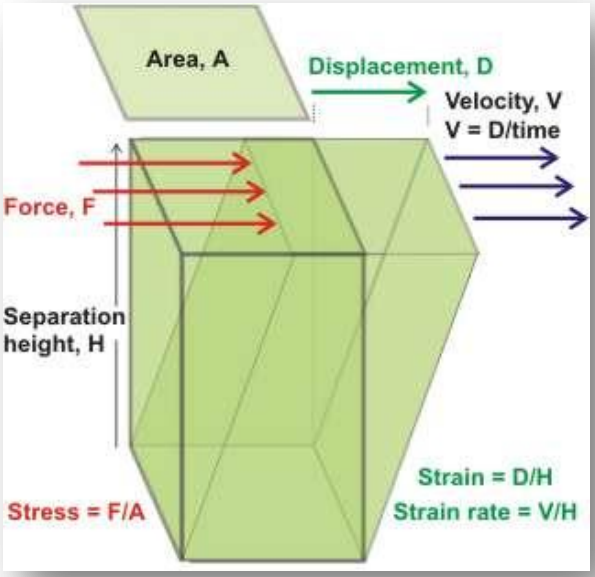

Fig. 16 Deformation and flow of a material in response to an applied stress.

Traditionally, rheological measurements are performed on several milliliters of material in a mechanical rheometer (e.g. a cone-and-plate geometry rheometer) by applying a small amplitude oscillatory shear strain $\gamma(t) = \gamma_0 \sin(\omega t)$ and measuring the resultant shear stress $\sigma(t)$. In the viscoelastic linear regime (or regime of small amplitude straining, typically $\gamma_0 << 1$), the shear stress is proportional to the amplitude of the applied strain γ_0 and is itself sinusoidal varying in time. It can be represented as:

$$\sigma(t) = \gamma_0 \left[G'(\omega) \sin(\omega t) + G''(\omega) \cos(\omega t) \right]$$

In the above equation, the term proportional to $G'(\omega)$ is in phase with the strain, while the term containing $G''(\omega)$ is in phase with the rate of strain $\dot{\gamma}(t) = \frac{d\gamma}{dt}$. $G'(\omega)$is called the storage modulus and represents storage of elastic energy, and $G'(\omega)$ is

called the loss modulus and represents the viscous dissipation of that energy. The complex shear modulus $G^*(\omega)$ is defined as $G^*(\omega) = G'(\omega) + iG''(\omega)$ (Bird, 1987).

Rheology measurements, important for industrial application, have given valuable insight into the structural rearrangements and mechanical response of a wide range of materials, in particular soft materials and complex fluids. However, conventional mechanical techniques are not always well-suited for all systems. Typically, milliliter sample volumes are required in rheology measurements, precluding the study of rare or precious materials, including many biological samples. Moreover, conventional rheometers provide a measurement of the averaged bulk response but do not allow for local measurements in inhomogeneous systems. To address these issues, a new class of measurement techniques has emerged. These have come to be called microrheology methods and probe the material response on micrometer length scales, using micro-liter sample volumes (Mason, 1997a) (MacKintosch, 1999). These methods typically use embedded micro-sized mechanical probes to locally deform the medium, and information is extracted from their motion. An outline of specific advantages of microrheology techniques over rheology techniques, based on considerations of the length scale, time scale, and energy/force scale at which they operate, has shown the following (Waigh, 2005):

- *High frequency response*: since the probe has low inertia it is possible to perform high frequency measurements of the material response by using methods such as Optical Tweezers (OT) and Diffusing Wave Spectroscopy (DWS). There are no prospects for such large frequency ranges using conventional bulk rheometers due to the large forces and torques required.
- *Minimization of sample volumes*: the amount of sample required to measure a complete viscoelastic spectrum is significantly reduced from some milliliters in traditional rheology to a few micro-liters in microrheology. This cuts cost and increases flexibility.
- *Length scale*: the sample viscoelasticity can be characterized by probing at micrometer length scales. This is important in heterogeneous materials where viscoelasticity varies from point to point in the sample (Tseng, 2001). Moreover, by changing the size of the probes, it is possible to characterize the hierarchical structures encountered in complex fluids at various length scales of observation (Solomon, 2002).

- *Non-invasive probes*: in passive microrheology only thermal energy (k_BT) of the order of a few *pN* acts on colloidal probes, providing a delicate probe that allows the study of the structure and dynamics of fragile soft matters such as intracellular cells properties without disrupting their components.
- *Agreement with bulk rheology*: microrheology measurements are in agreement with bulk rheology values even if many questions are still open on how the sample chemistry and heterogeneity relates to this agreement (Dasgupta, 2002) (Mason, 1995) (Mason, 1997a). A required condition is that the relative size of the probes must be bigger than the structural length scale (mesh-size) of the complex material in order to treat the medium as a continuum around the embedded probes.

1.5.1 Microrheology techniques

Microrheology techniques are dynamic techniques able to explore the viscoelastic response of a complex fluid at a mesoscopic scale using tracer microparticles embedded in the sample, Fig.17.

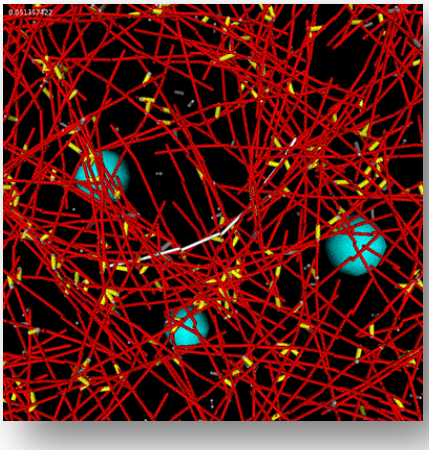

Fig. 17 Embedded micro-sized mechanical probes to locally deform the medium and extract information from their motion.

Microrheology allows for measuring viscoelasticity at higher frequencies, above 1 *kHz* or even up to *MHz*, because inertia of both the probe and embedding medium can be neglected at such small length scales (Levine, 2001) (Peterman, 2003). They are usually classified as active and passive, depending on whether the

strain is recovered after an externally applied stress or on whether the medium deformation are caused by the thermal energy k_BT, respectively. Passive techniques, like Multiple Particle Tracking (MPT), Laser Particle Tracking (LPT) and Diffusing Wave Spectroscopy (DWS), are typically more useful for measuring low values of predominantly viscous moduli, whereas active techniques, like Magnetic Tweezers (MT) and Atomic Force Microscopy (AFM), can extend the measurable range to samples containing significant amounts of elasticity. Active techniques involve the use of optical or magnetic forces to move probe particles and apply local stress to complex materials. Although active measurements can be extremely useful, especially in stiff materials where large stresses are necessary to obtain a measureable strain, large particles are required to apply sufficiently well-controlled forces to the material, preventing the application of this technique to very small length scales.

To measure cell mechanics, cells are usually deformed by many techniques (Kasza, 2008). Whole-cell deformations use torsion pendulum (Eichinger, 1996), parallel plates (Thoumine, 1997), and micropipette aspiration (Hochmuth, 1993). Smaller mechanical probes of cells include micro-needles (Felder, 1990) (Nicklas, 1983), cell pokeres (Petersen, 1982) and atomic force microscopy (Radmacher, 1996) (A-Hassan, 1998). Magnetic forces are applied to particles within living cells (Bausch, 1999) (Valberg, 1985) (Crick, 1950), and attached to the surface of living cells (Bausch, 1998) (Wang, 1993). So far, optical forces are only applied to deforming soft sub-cellular structures, such as plasma membrane (Kuo, 1992) (Schmidt, 1993). Mechanical measurements using direct deformations are slow and often invasive. Deformations can be so large as to be nonlinear. To overcome these limits, passive microrheology techniques, which involve only the observation of the thermal fluctuations of the probe particles, are used. In this case there are no limits on particle size, but the material must be sufficiently soft to allow detectable motion of particles moving with only thermal energy.

1.5.2 Comparison between active microrheology techniques

Active microrheology techniques allow measurement analogues to conventional mechanical rheology techniques in which an external stress is applied to a sample and the resultant strain is measured to obtain the shear moduli; however, in this case, micron-sized probes locally deform the material and probe the local viscoelastic response. Magnetic Tweezers (MT) fall in the ‘active’ category of microrheology techniques because they involve the manipulation of magnetic particles embedded in the sample by an external magnetic field. Microrheology measurement

by magnetic beads was pioneered in the early 1920's and has been used to measure the mechanical properties of gelatine, cellular cytoplasm, and mucus (Breuer). Because of technical difficulties in generating high local magnetic fields, field gradients, and the lack of spherical magnetic beads, quantitative measurements were possible only with large beads, 10 μm in diameter, and in large cells such as urchin eggs (Hiramoto, 1969). Viscoelastic properties of smaller cells such as macrophages were measured by torsional deformations achieved by magnetic twisting of magnetic beads (Valdberg, 1987) (Valberg, 1987). Developments in colloidal engineering, video microscopy, and position sensitive detection have promoted the emergence of several high-precision magnetic-particle micro-rheology techniques.

Recently a magnetic bead micro-rheometer, also known as Magnetic Tweezers, has been developed. It combines the use of strong magnets to manipulate embedded super-paramagnetic particles with video microscopy to record the displacement of the particles upon application of constant or time-dependent forces (Bausch, 1999) (Amblard, 1996) (Ziemann, 1994). In this case strong magnetic fields are required to induce a magnetic dipole in the super-paramagnetic beads, and magnetic field gradients are applied to produce a force. The resultant particle displacements, obtained using video recording techniques, measures the viscoelastic response of the surrounding material with a spatial resolution of 10 *nm* and a time resolution of 0.04 *s*. Magnetic Tweezers are capable of generating forces in the *nN* range on super-paramagnetic beads with diameters smaller than 5 μm. They have been used to investigate the microscopic dynamics of several materials that are not easily probed with traditional bulk techniques, including networks of actin filaments, living fibroblasts, macrophages, and endothelial cells (Breuer). Compared with other techniques that allow local measurements of viscoelasticity from the outside (Radmacher, 1996) (Daily, 1984), MT allows local measurements inside and outside living cells. Magnetic Tweezers also have the advantage over their optical counterparts in that (a) they do not generate heat in the examined sample, (b) can have an uniform force field over the entire field of view, and (c) can orient objects regardless of their geometry (Strick, 2003). They do have the disadvantage that it is difficult to make multiple independent traps. In addition to the magnetic tweezers method, a number of other magnetic-particles techniques have been developed to measure material response.

For example, Twisting Magnetometry (TM) measures the response of magnetic inclusions in a viscous or viscoelastic medium to the brief application of a

strong external magnetic field (Valberg, 1987). The strong field aligns the magnetic moments of the inclusions, which can be magnetic colloidal particles or aggregates. When the field is turned-off, the aligned magnetic moments give rise to a measurable magnetic field, called the 'remnant field', which decays as the moments become randomized. The decay can be interpreted in terms of the local viscosity. A modification of the TM, called Magnetic Twisting Cytometry, has been used to apply mechanical stress directly to cell surface receptors using ligand coated magnetic colloidal particles that are deposited on the surface of a living cell. When the twisting magnetic field is made to vary sinusoidally in time, bead displacement can be interpreted in terms of the local viscoelastic response (Fabry, 2001).

Optical tweezers (OT), first developed by Ashkin (Ashkin, 1992), are another active microrheology technique that employ a highly focused laser beam to capture and manipulate small dielectric particles. Unlike MT, OT apply force vey locally, and the forces typically range between o.1 and 100 *pN*. Two main forces are exerted on trapped particles: the scattering force, also called radiation pressure, which acts along the direction of beam propagation, and the gradient force, which arises from induced dipole interactions with the electric field gradient and tends to pull particles toward the focus. A high numerical aperture objective lens, used to focus the laser beam in the sample, allows the gradient force to dominate and forms a stable three-dimensional trap. Moving the focused laser beam forces the particle to move, applies local stress to the surrounding medium, and probes the rheological response (Breuer) (Svoboda, 1994). Optical tweezers use single particles and provide for local measurements in inhomogeneous materials. With respect to video-based magnetic particle manipulation techniques, OT investigates higher frequency; however, forces are limited to the *pN* range, and local heating can occur as well as local phototoxic effects in biological systems.

Atomic Force Microscopy (AFM) is another active technique used to study the structure and local mechanical response of soft materials, biological materials in particular, with a sub-nanometer resolution. This is explained in details in Appendix A. It has been used to measure the local elasticity or viscoelasticity of thin samples such as gelatine, living cells, and polyacrylamide gels. An AFM is used in constant-force tapping mode for both imaging and elasticity measurements. The deflection of the cantilever is measured as it approaches the sample for each elastic measurement. In viscoelastic samples, AFM technique can be modified to obtain viscosity in-

formation by measuring the relaxation of the tip into the sample. As in all active manipulation techniques, the strain amplitude and driving frequency can be varied.

Finally, the Oscillating Rod Rheometer (ORR) is an acoustic active technique that allows determination of both acoustic and rheology parameters of gels and fluids. An oscillating glass-fibre sensor serves as sensor for the viscosity of the surrounding fluid. Small displacements, 1-100 *nm*, are caused by the glass rod oscillating at its resonance frequency. They are analyzed by a phase-sensitive acoustic microscope. Alterations of the elastic modulus of a fluid change the propagation speed of a longitudinal acoustic wave. So ORR simultaneously allows calculation of the volume elasticity of a fluid from measurements of the velocity of longitudinal ultrasonic waves and determination of the dynamic viscosity from the oscillations of a glass rod immersed in the viscous fluid (Wagner, 1999). This technique allows the study of sample quantities as small as 10 μl with temporal resolution greater than 1 *Hz*. In comparison with other rheometers, such as plate-plate or plate-cone rheometers, the oscillation of a glass rod acting as a sensor for viscosity causes a shear wave that is equivalent to the dimension of the rod and thus can propagate its full extent through the surrounding fluid with extremely small strain.

1.5.3 Comparison between passive microrheology techniques

Passive microrheology techniques uses the Brownian dynamics of particles embedded in the sample to measure the viscoelastic response. Materials must be soft enough to allow detectable motion of particles that move with only thermal energy, k_BT. The Brownian motion of a probe particle immersed in a network is directly related to the network's mechanical properties. Particles exhibit larger motions when their local environments are less rigid or less viscous. The mean-square-displacement (MSD) of the particle's trajectory is used to quantify its amplitude of motions over different time scales.

Diffusing Wave Spectroscopy (DWS) is a light-scattering-based technique which probes the linear rheology properties of biopolymer networks noninvasively (Palmer, 1998) (Petka, 1998). This technique is based on the measurements of the autocorrelation function of the light multiply scattered from microspheres embedded in the network. Using the autocorrelation function and the generalized Stokes-Einstein equation, the MSD of the probing particles is calculated. From MSD the viscoelastic moduli of the network are extracted. This technique has been used largely by Palmer et al. to measure the viscoelastic moduli of networks of highly purified,

uncross-linked F-actin (Plamer, 1999) and by Mason et al. to measure the elastic properties of several representative complex fluid samples (Mason, 1997b). Unlike Single-Particle-Tracking (SPT), which monitors the displacement of only one particle at a time, DWS monitors many thousands of microspheres simultaneously, which allows for superior statistics. Moreover, with DWS, frequencies up to 1 MHz can be explored, which is four orders of magnitude larger than possible with mechanical rheometers, Fig.18.

Laser Tracking Microrheology (LTM) is another passive technique that measures the fluctuation spectrum of a probe particle embedded in a complex fluid using the laser light forward-scattered from a single particle with a quadrant diode. LTM provides the same viscoelastic spectra as mechanical rheometers without applying external forces to the sample. Despite many molecular methods for cytoskeleton structure analysis, current biophysical methods lack the speed and resolution to monitor mechanics in living cells and so cannot adequately test molecular models. LTM quickly characterizes mechanical properties over the 5-decade range of frequencies (Yamada, 2000). Laser Tracking techniques have a high sampling frequency and can also explore a large frequency range from 10 *Hz* to tens of *kHz* instead of the few *Hz* explored using Video Tracking (VT) techniques. Moreover, the sensitivity is about 1-2 *nm* in LTM versus 10 *nm* in VT.

Laser Interferometry (LI) is another accurate technique to measure particle fluctuations. The laser beam is split in two oppositely polarized components and focused on the probe particle. The relative change in polarization upon scattering provide information on the particle displacement. Using linear response theory (Schnurr, 1997), local values of the viscoelastic response are determined, without actively straining the sample. This method has the advantage that the displacement detection is biaxial, has higher resolution than the standard arrangement, and is independent of the position of the laser focus on the specimen plane (Waigh, 2005). Unlike tracking microrheology techniques limited by the spatial and temporal resolution of video microscopy, LI in a light microscope provides high resolution (less than 1 *nm*) and bandwidth (from 0.1 *Hz* to 20 *kHz*). Laser interferometry has been largely used to study semi-flexible polymer systems like F-actin solution (Schnurr, 1997) and fd virus (Addas, 2004).

The viscoelastic response of a medium can be also measured with fluorescent methods such as Fluorescence Correlation Spectroscopy (FCS) and Fluores-

cence Recovery After Photobleaching (FRAP). For example, FCS has been used to investigate the diffusion behaviour of many inert gold nano-particles in the cytoplasm and nucleoplasm of cancerous cells such as HeLa and HepG2 cells and in healthy cells like THLE, under various stress conditions. Frog egg extract has also been tested (Guigas, 2007). This technique has the advantage of using small particles instead of particle tracking techniques restricted to the use of large beads with diameters of about 100 *nm* and also limited in time resolution. Luby-Phelps et al. used FRAP to measure the viscosity of cytoplasm of Swiss 3T3 cells, without the application of mechanical stress that damages or disrupts cytoplasm structure (Luby-Phelps, 1986) (Kole, 2004). This technique measures fluorescence recovery in a photo-bleached region of the sample due to the diffusion or drift of a large number of molecules. Fluorescence Recovery After Photobleaching measurements are based on the behaviour of large ensembles of particle probes with a spatial resolution of ~0.5 μm. In contrast, SPT observes motion over a spatial range (~10 *nm*) at least one order of magnitude smaller than that accessible to FRAP.

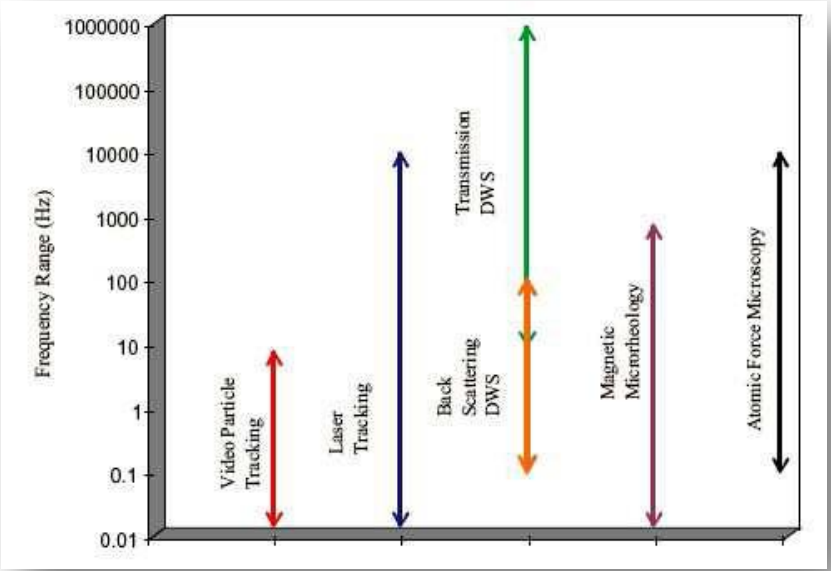

Fig. 18 Comparison between working frequency range in active and passive microrheology techniques.

1.6 Particle Tracking techniques

Particle tracking techniques directly derive from the experimental studies of Perrin and are probably the most commonly used passive microrheology methods to investigate intracellular mechanics in living cells (Kole, 2005). Probe particles are embedded in a viscoelastic sample and its properties are extracted from the thermal fluctuation spectra measured using digital video-microscopy. In passive measurements, the key parameter is the mean-square-displacement of the tracer particles, and this can be measured by various methods. Single-Particle-Tracking uses a single probe particle to measure highly localized mechanical response with high spatial and temporal sensitivity. Because this method uses a single probe instead of averaging over an ensemble, it is well-suited to studying local microenvironments (Valentine, 2001). By contrast, Multiple-Particle-Tracking techniques characterize the motions of a large collection of particles allowing for better statistics and easer analysis of sample heterogeneity (Tseng, 2001).

Recently, a novel method called Two-Point-Microrheology (TPM), is replacing traditional microrheology techniques (Crocker, 2000). This new technique is based on cross correlating the thermal motion of pairs of embedded tracer particles, removing most of the uncertain interpretation and overcoming the limitation of conventional microrheology. In fact, it does not depend on the size or shape of the tracer particle; moreover, it is independent of the coupling between the tracer and the medium. Two-Point-Microrheology has the disadvantage that, like all methods based on Brownian motion, it can be confounded by active intracellular processes. Since TPM probes a three-dimensional structure much larger than the tracers, it is best suited to measure the microrheology of the thick central body of the cell, avoiding the thin structures, such as cell cortex or nuclear envelope (Crocker, 2007).

1.6.1 Multiple-Particle-Tracking technique

To investigate the mechanical response of starfish oocyte cytoplasm, we chose the Multiple-Particle-Tracking technique because it is a type of functional microscopy that can test the local, time-dependent mechanical and structural properties of living cells. Moreover, unlike SPT it is not a time-consuming method for the generation of ensemble average MSDs and MSD distributions over a whole specimen. In an SPT measurements, numerous observations of the stochastic motion of individual particles must be characterized statistically to yield the appropriate time

average transport properties. In contrast, the participation of many particles provides an ensemble average of their diffusion behaviour in a single MPT measurement. This allows us to directly probe and characterize heterogeneous microenvironments even in samples that are dynamically changing in time so that consecutive experiments are not possible. Also the DWS technique, as previously noted, probes the motion of several thousands of particles simultaneously and allows for the collection of very low-noise MSD spectra, from which rheology data can be generated over a wide frequency range. However, much information is lost because DWS measurements are intrinsically ensemble-averaged, and therefore, cannot be used to measure MSD distribution (Apgar, 2000). In any event, we did not overly increase the number of probe particles (not more than 30 beads for each field of view) to avoid particle-particle interactions and to avoid artefact geometric deformation of the fluorescent trace of a given particle in focus by fluorescent particles out of focus.

In our experiments MPT collects and analyzes the distribution of Brownian displacements of micro beads injected into the cytoplasm of living cells to spatially map local viscoelastic properties. The thermal energy k_BT creates a random force with an order of magnitude of k_BT/a on each bead, where *a* is the radius of the bead. This force (<< 1 *pN*) creates a local dynamic deformation of the viscoelastic medium next to the particle, which affects the particle's displacement, itself measured by video particle tracking. The dynamics of particle motion are usually described by the time-dependent mean-square-displacement, $\langle \Delta r^2(t) \rangle = \langle [x(t+\tau) - x(t)]^2 + [y(t+\tau) - y(t)]^2 + [z(t+\tau) - z(t)]^2 \rangle$ that is calculated from the three-dimensional trajectories of the centroids of the particles, where τ is the time scale. In purely viscous material, MSDs of particles vary linearly with time; in purely elastic media MSDs are constant, regardless of time. When particles diffuse in viscoelastic media the $\langle \Delta r^2(\tau) \rangle$ becomes non-linear with time and can be described with a time dependent power law, $\langle \Delta r^2(\tau) \rangle \sim \tau^{\alpha}$. The slope of the log-log plot of the $\langle \Delta r^2(\tau) \rangle$, α, is called the diffusive exponent. It describes the mode of motion a particle is undergoing and is defined for physical process between $0 \leq \alpha \leq 1$.

The motion of particles in a medium can be also quantified with the diffusion coefficient *D*, which is a measure of how rapidly particles execute a thermally driven random walk. Diffusion coefficient illustrates the relation between $\langle \Delta r^2(t) \rangle$ and the local viscoelasticity of the medium. The simplest rheology model is that of a Newtonian (purely viscous) fluid, where the viscosity η is related to the diffusion coefficient by the Stoke-Einstein equation; thus $D = k_BT/6\pi\eta a$. Brownian motion in such an

environment is described as a random walk in *d* dimensions, displaying a MSD $\langle \Delta r^2(t) \rangle = 2dDt$ (α=1 indicates a simple diffusion). Such behaviour is observed, for example, in water or glycerol. Non-Newtonian environments are characterized by a memory effect in the drag coefficient or equivalently a time-dependent viscosity. Thermal motion in such a medium shows an anomalous sub-diffusion (α<1) and the diffusion coefficient becomes $D = k_B T / 6\pi\eta(t)a$. Such behaviour is observed generally in polymer and membrane systems. For a non-dissipative Hookean solid of elastic modulus G, the MSD of the particles is independent of time so $\langle \Delta r^2(t) \rangle = A$, where $A = k_B T / \pi G a$ is a constant.

Assuming that inertial effects are negligible, the viscoelastic moduli are related to MSD by (Mason, 1995):

$$G(s) = \frac{k_B T}{\pi a s \langle \Delta r^2(s) \rangle}$$

where *s* is the Laplace frequency, k_B Boltzmann's constant, T the absolute temperature, *a* the radius of the particle, and $\langle \Delta r^2(s) \rangle$ the unilateral Laplace transform of $\langle \Delta r^2(t) \rangle$. For this equation to be valid, three criteria must be satisfied: rigid particle, spherical particle, and a network well-approximated as a viscoelastic continuum. Requirements for spherical and rigid particles derive from a generalization of Stoke's law as a complex function for the particle's resistance to motion within viscoelastic materials. To satisfy the continuum approximation, the particle must be much larger than the mesh-size of the network (Yamada, 2000). The viscoelastic moduli are the real and imaginary parts, respectively, of the complex modulus G^*, which is the projection of $G(s)$ in Fourier space (Mason, 1997a).

1.6.2 Experimental Setup for Multiple-Particle-Tracking

The video microscopy setup consists of an inverted epifluorescence microscope (Olympus IX70) supplied by a *60X* water immersion, infinity-corrected objective (Olympus, UPLAPO W3), with a numerical aperture *NA*=1.2, Fig.19. The spatial resolution is limited by the diffraction limit to 100 *nm*. The microscope is equipped with two light sources: a halogen and a mercury lamp. The light beam coming from the mercury lamp passes through an excitation filter that transmits only a certain range of wavelengths. Within this range, the illumination is reflected by a dichroic filter towards the sample, through the objective, to excite the fluorescent probes. The probes emit a signal that returns through the objective to the dichroic filter, that is

transparent at the emission wavelength. A final emission filter is placed on the optical path before the visualization ports of the microscope to block any stray transmitted excitation light. We used red-fluorescent particles that matches rhodamine fluorescent spectrum. A charge-coupled-device (CCD) camera (Hamamatsu C5985) is attached to the side port of the microscope. The CCD resolution is 768X494 *pixels* and the maximum frame rate is 30 *fps*. The output of the camera is connected to the computer to data analysis.

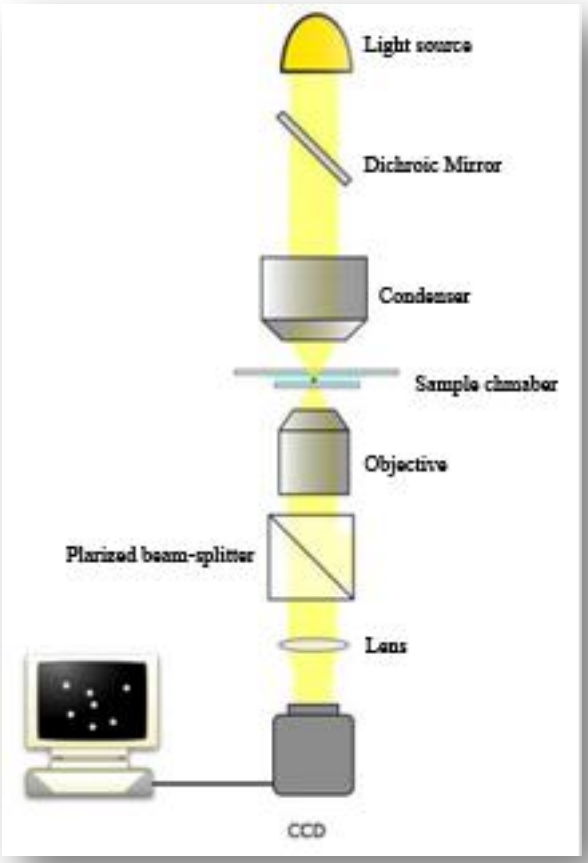

Fig. 19 Experimental setup for Multiple-Particle-Tracking

We recorded images at a video rate of 20 *fps,* which means that each frame was captured every 0.05 *s*. Therefore, the viscoelastic properties of the sample can be characterized up to 20 *Hz*. The field-of-view in the focal plane of our objective is about 100 *μm* x 80 *μm*. Images are captured for a movie length of about 100 *s*. About 20-30 particles are presented in each movie. The movies are saved as **.avi* files and then transformed in **.pgm* images. These types of file are directly readable

by the image processing software *Image J,* which works in *a Java* environment. This software allows the removal of noise from the image using a threshold filter, calculates the centroid of the particle, and assigns one trajectory to each particle. Trajectories information is collected in a file **.txt*. This is subsequently analyzed by home-made programs, which work in *Matlab 7,* to obtain the coordinates of the particle centroid and the MSD of each trajectory.

1.6.3 CCD calibration

To know the *x* and *y* displacements of the probe particle, the feedback system has to be calibrated. The minimum displacement detectable with our setup is about 15 *nm* and is measured by recording the motion of a 400 *nm* microsphere stuck on the coverslip, as was also done by Apgar et al. (Apgar, 2000). We move the microsphere for 7-8 steps, each 500 *nm*, along the *x* direction for the full length of the CCD region. For each step an image is recorded. Then we move 2 μm along the *y* direction and start again with the movements along the *x* direction. In this way we record the bead position in all of the active region of the CCD. For each row the centroid of the microsphere is calculated and reported as a function of the displacements. A linear fit of the curve gives us the CCD calibration factor (Fig.20). However, CCD pixels are not perfectly square so we calculate the calibration factor along both *x* and *y* directions and average them to obtain the final calibration factor in $\mu m/pixel$. For a 60X water immersion microscope objective, the calibration factor is 0.093 $\mu m/pixel$.

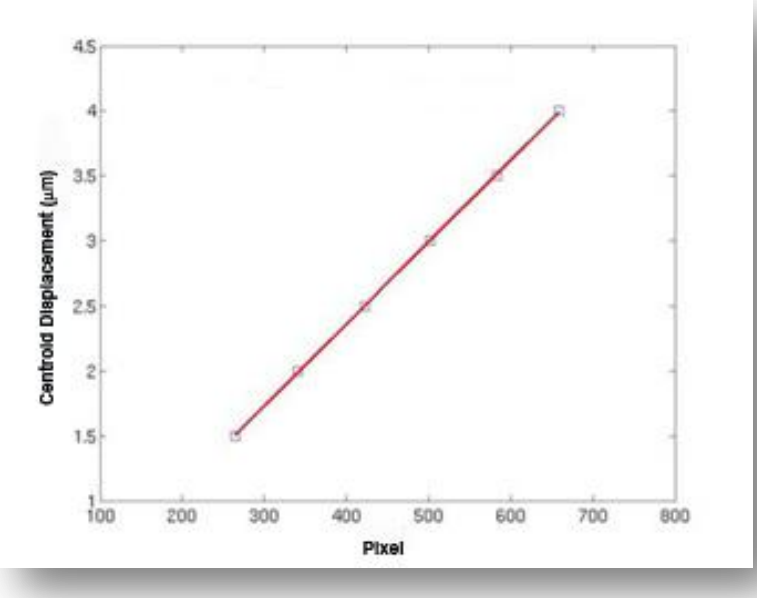

Fig. 20 CCD calibration plot.

1.6.4 Data storage and analysis

Several algorithms are involved in Multiple-Particle-Tracking analysis. In particular four steps are necessary to correct defects in each single image, to calculate particle centroid, to remove 'false' positions that do not correspond to particle and to correlate particle position in a frame with particle position in the previous or the next frame.

1.6.4.1 Image Restoration

A good image may also content artefacts that limit particle localization. "Shading" and "snow" are the names of the two main defects present in an image. They involve intensity variation in the background brightness, inducing difficulties in particle detection. It is important to correct these imperfections to make clearly visible particles on the background. To do it, a threshold filter is applied to the image to reduce both high spatial frequency (*shading*) and low spatial frequency (*snow*) while keeping the intermediate frequencies that contain the interesting information. After this process fluorescent particles appear as bright spots in a dark field, like stars in a night sky (Fig.13B).

1.6.4.2 Calculus of Particle Centroid

Each fluorescent particle image is characterized by a Gaussian intensity profile with a circular symmetry along the particle diameter. Particle localization algorithms detect these light zones and use a Gaussian mask, which surrounds the particle, to find the centroid of this intensity profile. To achieve a sub-pixel resolution the mask must be a little greater than the particle diameter. Usually nanometre spatial resolutions of 5-10 *nm* are obtained. Each particle image (**.pgm* file) has a resolution of 768X494 *pixels*. Using *Image J*, we make a stuck of the image sequence, select the region containing the fluorescent particles in each image, and save the stuck, digitalized at 8 bit of resolution, as **.tiff* file. In each selected region there are more or less 10-20 micro-particles.

The region image is stored into a square matrix, M_{ij}, whose values range from 0 (black) to 255 (white). By applying the threshold filter, the maximum contrast between particles and background is achieved: the beads appears as a white circles on a dark background. Micro-particles centroids can now calculated as previously

described. Particles centroids are obtained using an *Image J* (NIH, Bethesda, MD) plug-in, *Particle Tracker* (Sbalzarini, 2005) (Crocker, 1996), which reveals particle traces recorded by video-microscopy systems. This software requires two parameters: the bead diameter in pixels and the brightness fraction over which the absolute maximum of intensity is revealed as a particle. These parameters are saved for all frames. Then other two parameters, *link range* and *displacement*, are given to obtain the best values to link particle position in each frame. After this, the program displays the trajectory of each particle and saves the information in a **.txt* file. Then the analysis continues with two other home-made *Matlab* routines: the first estimates the Brownian trajectories for each particle and the second calculates the mean-square-displacement averaged over all particles. By extending Brownian trajectories analysis to a large number of trajectories recorded at different locations in the cytoplasm of several cells and computing the ensemble-averaged MSD, we obtained an estimation of the average viscoelastic response of the cytoplasm.

1.6.4.3 'False' Position Elimination

Usually centroid algorithm reveals the absolute maximum of intensity as a possible particle, but some of these maxima could be intracellular structures with low contrast or simply CCD noise. So it is fundamental to distinguish real particles from false particles. Software can do this based on differences in morphology, dimension and intensity. For example, both small spots and large spots have to be discarded because they are image residuals and intracellular structures respectively.

1.6.4.4 Linking Positions

The bead positions are matched frame by frame to identify each particle and generate its trajectory. Frame-by-frame matching assumes that the closest particle in the next frame is the same particle. This is a reasonable assumption because the change in position frame by frame was very small compared with the spacing between beads. To do it, the software needs the *maximum displacement* of a particle between two subsequent frames. In this way a particle that moves between two frames with less than the *maximum displacement* is considered the same particle and the two positions are linked to obtain the trajectory. If the displacement is greater than the *maximum displacement,* the algorithms reveals two distinct particles. It could happen that one or more particles are crossed. In this case it is difficult to identify them in all frames so the software requires another parameter, the *link*

range. The *link range* is the number of frames that the software will consider to assign the right trajectory to each particle. Moreover, it could happen that particle trajectory is momentarily out of focus. In this case there is a frame gap in which the particle is not found, so trajectory is divided into two trajectories. In this situation, a *memory function*, which memorizes the last particle positions, can restore the trajectory if the particle absence is not too great.

1.6.5 Error sources in Multiple Particle Tracking

Several common sources of error such as random error, systematic errors and dynamic error are present in particle tracking instruments, (Crocker, 2000). While some of these error sources can be eased by the use of high quality equipment, most errors are due to irreducible physical limitations on imaging detector performance and illumination brightness.

1.6.5.1 Random error: CCD noise

The accuracy of particle localization lead to an high quality measurement of cellular microrheology. Some noise in a CCD depends on the details of its construction and electronics, but there are also physical limits on the performance of all CCDs due to the discrete nature of light itself. Whenever imaging a sample, there will be statistical fluctuations in the number of photons detected by the camera even under ideal conditions. These fluctuations are irreducible and lead to random errors in the reported brightness of individual pixels. In general, using a higher illumination will reduce this error, but is ultimately limited by detector saturation.

A CCD record the precise coordinates of all incoming photons arriving from a microscope. If a single photon is detected the position of a circular particle of radius *a* (set to be at zero) can be determined to +/- *a*, Fig.21b. If more photons are detected a cloud is perceived. This limits the potential position of the particle reducing measurement error to $\sigma_{x=}\sigma_{y=} \pm \frac{a}{\sqrt{N}}$, where *N* is the number of photons (Fig.21c). Well-made cameras approach this physical limit of performance when they are operating at illumination levels near the maximum allowed by detector saturation. Rather than averaging the positions of individual photons, it is better to determine the tracer's position by calculating the centroid of an intensity distribution. Provided that the tracer image is spread over a sufficient number of pixels to reasonably represent the tracer's brightness distribution, the error in the centroid positions is precisely the same as that in the previous example.

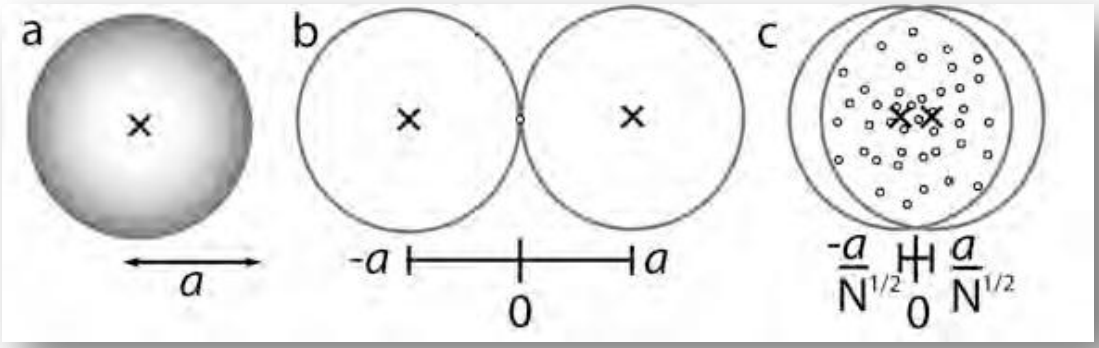

Fig. 21 Schematic example to explain a random error for a circular particle of radius 'a' whose centre is marked by an 'x' (a).

1.6.5.2 Systematic errors

Dividing the image of a small tracer into pixels could introduce systematic errors into the computed particle positions. One form of systematic error is 'pixel biasing' the tendency of the algorithm to round the centroid position to the nearest pixel. One source of pixel biasing is a too low magnification. This problem occurs if the tracer image is smaller than 1 *pixel,* but it can largely be avoided by use the proper magnification ensuring that single tracer images appear more than 3-4 *pixels* in diameter.

This error also commonly occurs during calculation of the centroid. When computing the centroid of a single tracer image, most algorithms mask off pixels outside some radius to avoid contributions from other nearby particles. Error is introduced if the background of the image is not zero at the edge of the mask. Physically, common image defects such as diffraction rings and out of focus background particles, or user errors such as specifying too small of a mask size, can cause this problem. For images relatively free of obvious defects, it is usually possible to reduce this error to less than 0.1 pixels by using a suitably large mask size.

Another source of systematic error is due to the fact that the individual detectors corresponding to each camera pixel are not equally sensitive to light. This typically introduces a systematic error between the physical and measured position that is a few percent of a pixel, and which varies randomly with location in the field of view. This error can be largely eliminated by calibrating each pixel in the camera us-

ing a uniformly illuminated specimen (an empty bright field), and then numerically correcting all pixel intensity values by division against the calibration image.

For microrheology using large ensembles of particles, the contribution of all these systematic errors can often be ignored because many measurements are squared and averaged together to compute an MSD; so the deviations will largely cancel.

1.6.5.3 Dynamic error

Another form of error that affects measurements of tracers' random motion is due to systematic underestimation of tracer motion when finite exposure times are used (Savin, 2005). This error is absent when the duration of the exposure is infinitesimal compared to the time interval between successive movie frames. If the particle moves significantly during the camera exposure, the measured centroid reports the time-averaged position during the exposure, Fig.22. Because random walks tend to loop back on themselves, this time averaging effect artificially reduces the amplitude of the mean squared displacement. This selective reduction of short lag time MSD value will make diffusive Brownian motion look super-diffusive (the MSD will increase more rapidly than linearly with time) at short lag times.

Using a short shutter time, the position at a given instant is recorded, for example at t=0.5 τ and t= 1.5 τ (black crosses). With a long shutter time, the time averaged location of a tracer is found, for example t intervals from 0-1 τ and 1-2 τ (gray crosses). The distance between time-averaged locations is systematically less than for instantaneous ones, Fig.22.

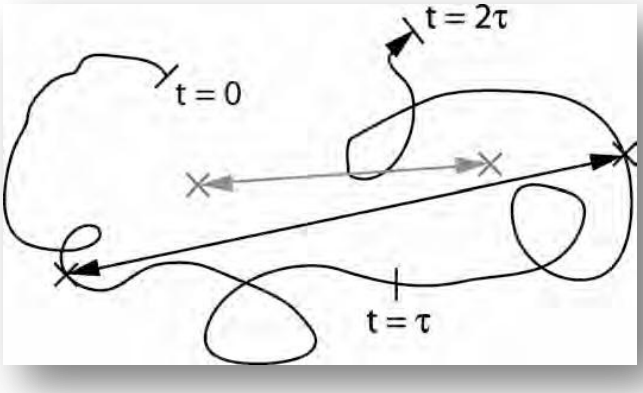

Fig. 22 An example of dynamic error in a random walk trajectory.

To minimize dynamic error is necessary to reduce the exposure time. Obviously, the solution is to use the longest exposure possible that will not introduce dynamic error. Crocker et al. find that if the amplitude of the mean-squared motion *during* the exposure interval is less than a quarter of the mean-squared motion *between* exposures, then the underestimation of MSD caused by dynamic error will be less than 10%. For tracers undergoing simple diffusive Brownian motion, this corresponds to an exposure time no longer than one quarter the time interval between frames, e.g. 1/200 *sec* for acquisition speeds of 50 *fps*, (Crocker, 2000).

Finally, thermal expansion can cause the stage or sample chambers to slowly translate across the camera field of view during long experiments, often by several pixels. This sample drift represents another source of uncertainty.

1.6.5.4 Errors on the MSD

Particle tracking errors lead to several perturbations in measured MSDs due to the contribution from random position measurement error which contribute additively to the value of the physical MSD:

$$\langle \Delta x^2 \rangle_{measured} = \langle \Delta x^2 \rangle_{physical} + 2\sigma_x^2$$

where σ_x is the standard deviation of the random position measurement error.

At short lag times, where the MSD is small, the measured MSD will start to flatten and appear sub-diffusive if the physical motion approaches the precision of the MSD. Conversely, if dynamic errors are significant, the MSD can appear super-diffusive at very short times. Another common artifact is that MSDs will tend to flatten at long times. This is due to particle loss from the imaging plane. While we image in two dimensions, particles diffuse in three dimensions and at long times will diffuse out of the imaging plane, (Crocker, 2000)

Results

1.7 MPT results in living starfish oocytes

For this investigation, only immature oocytes are microinjected. Microrheology investigations in mature oocytes are made by adding 1-MA hormone to previously microinjected immature oocytes. Because of the chaotic movement of oocyte content during the GVBD process, all measurements on mature oocytes are made at least 90 *min* after the hormone addition, i.e. when maturation is concluded. During acquisition of Brownian trajectories, we check that oocytes are immobile. Particle trajectories are monitored from several distinct cells (N>20) using different kinds of bead surface chemistry (PEG, CLM, ALM and PS) and size of 400 *nm* (diameter). In our experiments we have found that bead chemistry has a little influence on the results of microrheology measurements. Beads with diameters greater than the mesh-size of the cytoskeleton network (several tens of nano-meter, (Koster, 2009)) are used to satisfy the approximation of continuum medium in the Stoke-Einstein equation. All measurements in the present experiment are made at room temperature (about 21°C).

1.7.1 MSD in Astropecten aranciacus immature oocytes

Several trajectories are recorded for each Neapolitan oocyte and the MSD is calculated from each trajectory. Fluorescent PEG micro-beads are used as first probes. Figure 23A shows MSDs of about 600 trajectories collected from about 20 examined oocytes, while Fig.23B shows the ensemble average over all oocytes. As can be seen, measurements display a large fluctuation, which is typical for heterogeneous media like cell cytoplasm. All MSD curves show a clear change in the slope around $\tau = 0.3$ *s*; this reflects the fact that the motion of microspheres inside cytoplasm is influenced by the environment with different time scales. In particular, the average curve reported in Fig.23B shows that at times longer than $\tau \sim 0.3$ *s*, the ensemble average MSD grows linearly with time ($\alpha \sim 1$), proving that bead motion is essentially diffusive. At times shorter than $\tau \sim 0.3$ *s* the exponent becomes $\alpha \sim 0.5$ (sub-diffusive motion).

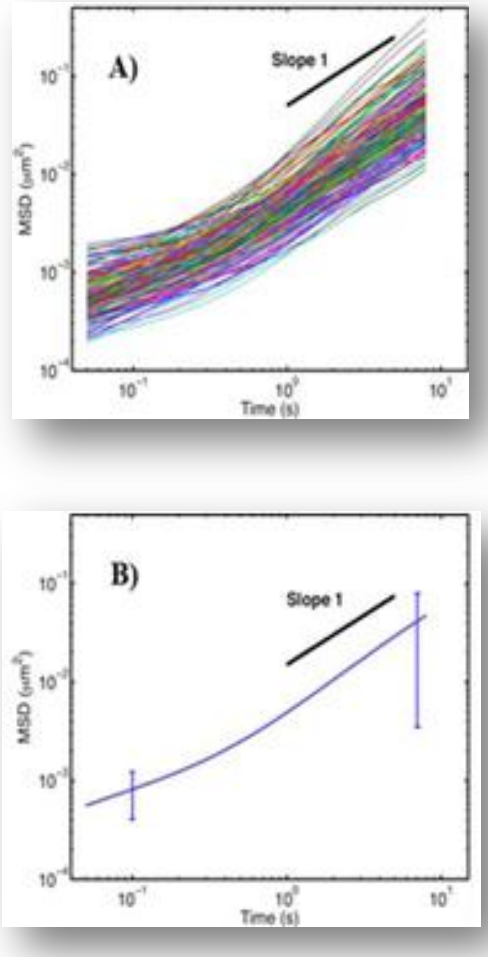

Fig. 23 MSDs of PEG beads inside immature oocytes of A.a. Panel A and B show respectively the all computed MSDs and the ensemble average MSD over all curves.

All curves of Fig.23A follow approximately the same viscoelastic trend; at short times trajectories sub-diffuse; at long times they begin free diffusion. Evidently, as is typical for biological materials, oocytes are heterogeneous systems in which viscoelastic properties change locally. The error bars in Fig.23B indicate the standard deviation as estimated from the histograms shown in Fig.24.

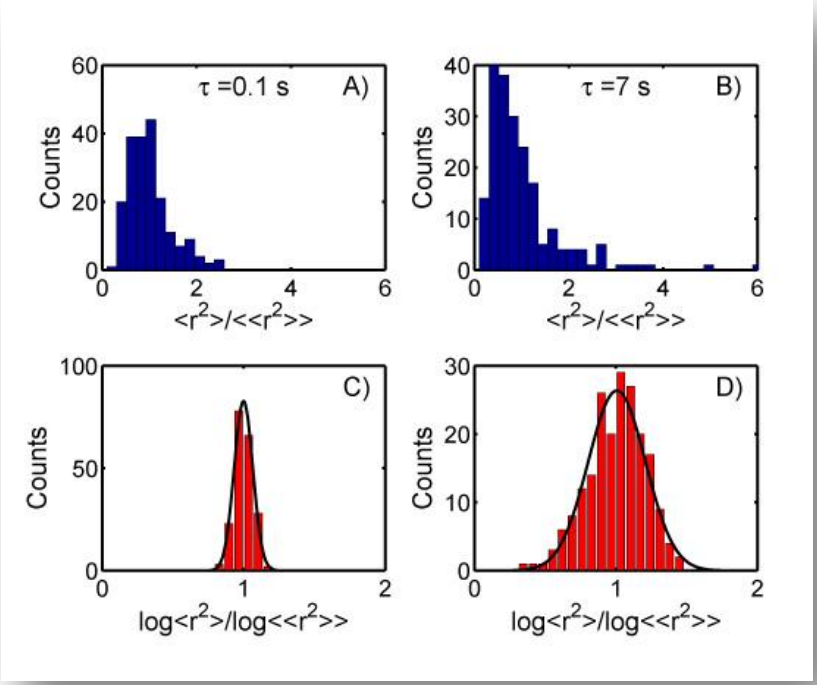

Fig. 24 Histograms of MSDs at given lag time, normalized to the average MSD at the same time for PEG beads inside immature Neapolitan oocytes. Panel A and B show histograms at short and long time respectively. Panel C and D show the same histograms computed using logarithmic values. Solid lines represent fits with Gaussian line shape.

Figure 24 shows the MSDs $<r^2>$ histograms at two lag times: τ ~ 0.1 *s* where bead motion is sub-diffusive and τ ~ 7 *s* for diffusive regime (panel A e B, respectively). MSDs are normalized to the ensemble average MSD $<<r^2>>$ at the same time. The distributions in Fig. 24A and B have a marked asymmetric profile rather than a Gaussian one. Panels C and D of Fig. 24 show the same histograms of panels A and B but computed using their logarithmic values; in this case the shape is closer to a Gaussian profile. In other words, the MSDs seem to not follow a normal distribution as their log-values do. This log-normal distribution, also observed by Citters et al. and Hoffman et al. (Citters, 2006) (Hoffman, 2006), is not yet fully understood and has recently attracted interest since it is involved in many fields of science (Limpert E., 2001). Moreover, by comparing the distribution in Fig.24 (A and B or, better, C and D), a greater enlargement can also be noted in the curve's distribution at long time scales. This behavior is in agreement with the theory of Brownian motion which, for Gaussian distributions, predicts that the standard deviation increases as $t^{0.5}$ (Rahman, 1964).

To study whether bead surface chemistry significantly affects particle motion inside living oocytes, fluorescent micro-particles functionalized with different chemical groups are used. Neapolitan oocytes are injected with CLM, ALM, and S microbeads. Figure 25 shows the observed ensemble average MSDs. The curves are qualitatively similar, proving that the interaction's particles-environment is essentially the same even though some slight differences in MSD slope are noted: at short time scales, CLM beads show an α value ~0.5 highlighting a more elastic behaviour in respect to S and ALM beads, which have an α value between 0.7 and 0.8.

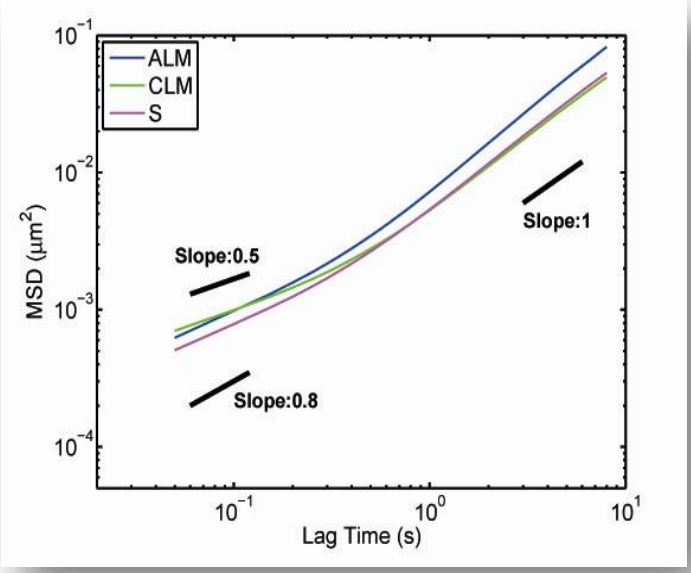

Fig. 25 Ensemble average MSDs for CLM, ALM and S micro-particles injected in the cytoplasm of A.a. immature oocytes.

From other collected data we compare the viscoelastic properties of immature oocytes coming from two different starfish species: *Astropecten aranciacus* and *Asterina pectinifera*. Figure 26 shows the average MSDs for CLM beads in immature oocytes of the two species. At long time scales MSDs of both species have a free diffusion ($\alpha \sim 1$) while at short time scales *A. a* shows a slope $\alpha \sim 0.5$ lower than *A.p.* slope $\alpha \sim 0.8$. This highlights a more elastic behaviour in Neapolitan oocytes at short time scales. Another diversity between *A.a.* and *A.p.* oocytes consists in a different relaxation time (see arrows in Fig.26), i.e. the time when the two regimes cross in the MSD. In general, this time indicates a characteristic time which marks the passage from an elastic to a viscous behaviour, and typically, it is estimated

from the frequency-law of the loss and storage moduli G' and G". In the time domain the relaxation time denotes the transition from sub-diffusive (viscoelastic) to diffusive (viscous) regimes. In our case we find that in Japanese oocytes the relaxation time is ~ 1 s, which is quite greater than ~ 0.3 s in Neapolitan oocytes. Since the cytoskeleton of a cell is a very complex structure consisting of intricate networks of different filaments it is rather hard to compare this numerical result with standard polymer models (Doi, 1994). In any event, our observation seems to confirm the powerful of MPT, which is able to evidence differences in the cytoskeleton organization of the two starfish species.

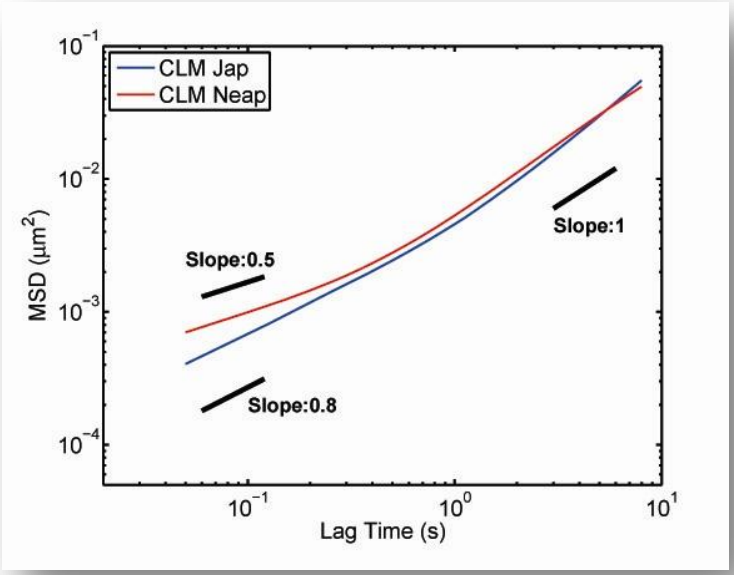

Fig. 26 A comparison of average MSDs relative to CLM micro-beads injected inside immature oocytes of Astropecten aranciacus and Asterina pectinifera.

1.7.2 Changes during Maturation in Astropecten aranciacus oocytes

Maturation represents a significant process accompanied by changes in mechanical properties and in cytoplasm organization. Hiramoto et al. (Hiramoto, 1976) showed changes in the rigidity of starfish oocytes while Heil-Chapdelaine et al. (Heil-Chapdelaine, 1996) and Kyozuka et al. (Kyozuka, 2008) observed changes in F-actin organization. The first step in this investigation is to visualize F-actin filaments in immature oocytes by microinjecting 50 μM Alexa Fluor 488- conjugated phalloidin and then visualize with confocal microscopy after 10 *min* incubation. Subsequently

the maturation process is induced by adding 1-MA hormone to immature oocytes and then taking confocal images to evaluate the GVBD effect on F-actin network.

The fluorescent confocal image of *Astropecten aranciacus* immature oocytes shows that F-actin is uniformly present throughout the whole. In addition, Figure 27A and B exhibit a dense network of filaments underneath the plasma membrane and inside the cytoplasm. Figure 27C and D depict the same oocyte one hour after the 1-MA addition. At this stage of maturation, the nuclear envelope is essentially disassembled and the nuclear compartment is weakly visible. Now the F-actin is drastically reduced. As is clearly visible, in the central region actin seems to be organized in thick bundles, while close to the cortical region, the actin is depleted with respect to immature oocytes. The same results have been obtained in Japanese A.p. starfish oocytes (data not shown).

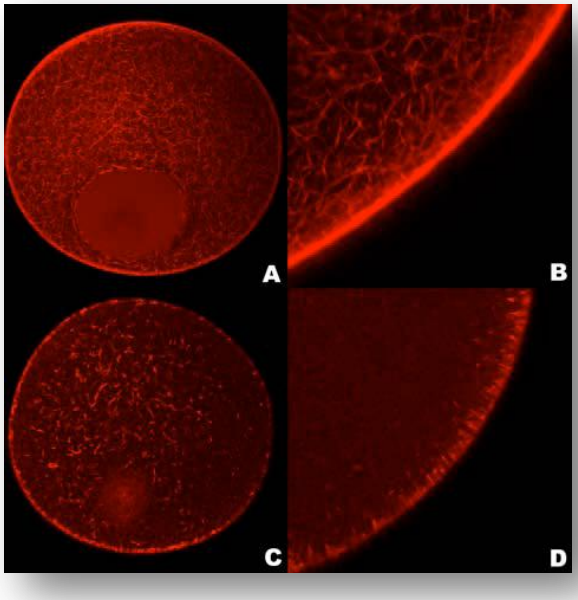

Fig. 27 Confocal image of F-actin network in an immature oocyte (A) and in a mature oocyte (C). Magnified image of cortex in immature oocyte (B) and in mature oocyte (D).

On basis of these observations, we investigate changes in the mechanical properties of cytoplasm by means of MPT. We start with immature oocytes microinjected with PEG beads and monitor their motion. Then we add 1-MA hormone to the same oocytes set and again record the PEG beads' thermal motion after 90 *min*,

when the dramatic mix of cytoplasm and nucleoplasm is concluded. Figure 28 shows the MSDs of immature and mature Neapolitan *A.a.* oocytes.

Unlike immature oocytes, MSDs of mature oocytes grow almost linearly with time for all investigated time scales. At short time average MSDs slope is ~0.9 in mature oocytes against ~0.4 in immature oocytes. Moreover, compared with immature oocytes, in mature oocytes a larger extent of motion is present (see y-axis in Fig.28) indicating that the beads are slightly less constrained. These results seem to suggest that mechanical response in mature oocyte cytoplasm is dominated by viscous dissipation. The actin network re-organization, shown in Fig.27, is likely one of the main factors responsible of this behavior. However, the complex structure of the cytoplasm cannot exclude the possibility that other cellular constituents concur to the mechanical changes. For this purpose, the addition of drugs (Latrunculin A and cytocalcin) able to disrupt selectively different filament families could provide further information on their role in oocytes cell mechanics.

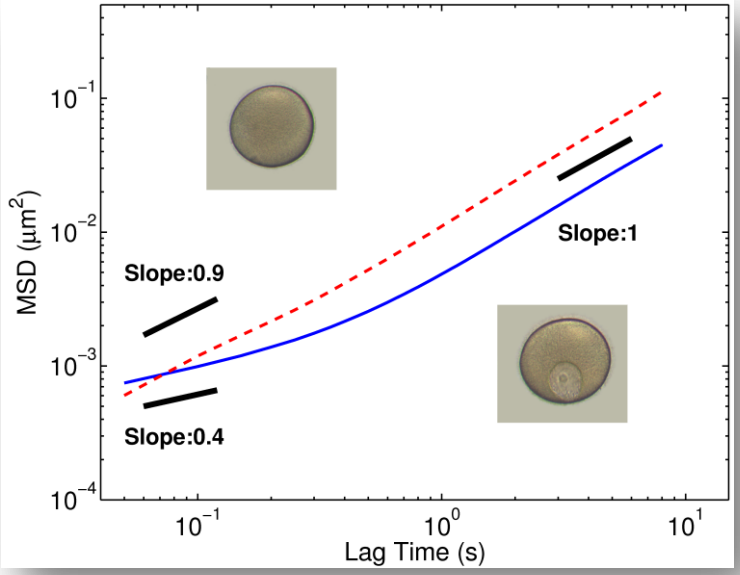

Fig. 28 Ensemble average MSDs in Neapolitan oocytes (immature: solid line / mature: dashed lines) injected with PEG micro-beads.

Finally, diffusion coefficient *D* is estimated for both starfish species, also in the case of mature oocytes. This is done using the slope values of MSDs at long lag time, when motion is essentially diffusive ($\alpha \sim 1$). The *D* values estimated from our measurements range from 0.004 to 0.01 $\mu m^2/s$. The viscosities η, for different situa-

tion, are then easily calculated from the diffusion coefficients using the Stokes-Einstein formula: $D=k_BT/6\pi\eta a$. Table 1 resumes all values of viscosity. *Astropecten aranciacus* immature oocytes show a greater viscosity compared with *Asterina pectinifera* oocytes: 0.75 *Pa·s* and 0.55 *Pa·s*, respectively. Moreover, *A.a.* oocyte cytoplasm viscosity decreases after maturation from 0.75 *Pa·s* to 0.31 *Pa·s*. In the literature, Daniels et al. (Daniels, 2006) found $\eta \sim 0.1$ *Pa·s*. in *C. elegans* developing embryos, while others analyze fibroblast cytoplasm (Panorchan, 2003) or simply cell extract viscosity (Valentine, 2005), but a direct comparison with our results is impossible because of the great differences from cell to cell.

Table 1: Viscosity values.

Materials	Viscosity (***Pa·s***)	Temperature (***°C***)	Beads diameter (***nm***) PEG
Water	1×10^{-3}	20	400
***A.p.* immature cytoplasm**	0.55	20	400
***A.a.*immature cytoplasm**	0.75	20	400
***A.a.* mature cytoplasm**	0.31	20	400

Conclusion

Viscoelastic properties of living starfish oocytes are inferred from the thermal fluctuations of embedded micro-beads inside the cytoplasm by means of the MPT technique. In the past, many studies have been made involving whole-cell deformation induced by micropipette aspiration or by compressing disk. Unlike traditional rheology, no forces are applied to actively deform oocytes during MPT measurements, so it is possible to investigate mechanical changes that occur after 1-MA hormone-induced maturation without modifying oocyte shape. Maturation involves

morphological transformation in cell structure and mechanical changes in the cytoplasm. Maturation is a crucial step toward fertilization. Oocytes move from a quiescent stage, when removed from the ovaries, to an active stage, just after GVBD. A quantitative estimation of viscoelastic properties in oocytes before and after maturation is essential to understanding cell response to physiological stimulation like hormones.

In our experiments mature oocytes are found to be less rigid than immature ones because microspheres diffuse more freely in mature than in immature oocytes. This is clearly shown by the comparison of the average MSD in Fig.28, which indicates that the curves for mature oocytes always run above those of immature oocytes. Our results are in agreement with the previous rheology measurements of Nemoto and Hiramoto. The loss in stiffness inside oocytes during maturation seems to relate to F-actin reorganization as shown in Fig.28 and as revealed by fluorescence confocal microscopy images of cytoplasm of intact oocytes fixed and stained with amounts of rhodamine-phalloidin (Heil-Chapdelaine, 1996), Fig.27. The F-actin changes are likely to be responsible for general morphological changes occurring in oocytes as a whole in the process of maturation. Our findings suggest that changes in starfish oocyte viscosity correlate with several basic cytoplasmic processes occurring at maturation. This conclusion opens new prospects for exploring the complex process of fertilization.

For the work carried out in this section I acknowledge Prof. A. Sasso, Dr. G. Pesce and Dr. L. Santella.

2 Multi-Trapping by means of diffractive optical elements

In recent years there has been a significant body of research conducted into extending the capabilities of optical trapping systems. An obvious approach is to modify trapping systems so that instead of creating just one or two traps, whole arrays of optical traps are generated. In this chapter the multiple-trapping technique based on Diffractive Optical Elements (DOEs) projected to a Liquid Chrystal Spatial Light Modulator (LCSLM) is presented. Applications of multiple trapping are interesting mainly in the field of cell manipulation. Multiple tweezers can be constructed simply by increasing the number of laser light sources or splitting a single laser beam in two, if only two traps are desired, or as many as necessary (up to hundreds have been demonstrated). A more flexible way of creating multiple tweezers from a single light source is to time-share the laser beam among a set of positions in the specimen plane (Cojoc, 2004). The typical time-shared optical traps are based on Acousto-Optical Deflectors (AODs) used to scan the tweezers. In an AOD, first order diffracted light is generated by sending the laser beam through a density grating in a crystal, created by a traveling acoustic wave at ultrasound frequencies. The deflection angle of the first order light, and therefore the tweezers position, is determined by the acoustic frequency driving the crystal. If the light is scanned quickly, the rapidly “blinking” individual traps mimic the effect of steady illumination because the dwelling time of the laser on each spot is enough to prevent the particle diffusion out from the trap. The bending and the time sharing of the beam allows the trapping of tens of beads in a field of tens of *μm* with an arbitrary configuration and intensity distribution. Because the AODs are computer controlled, the number and relative strengths of the traps, their spatial patterns, as well as the scanning rates can all be chosen with great flexibility without the need to change any optics. The main drawback of AODs is the restriction to planar patterns of traps. The splitting of the beam obtained by using a diffractive beam-splitter can overcome this limit. Such a beam-splitter can be implemented as a computer generated DOE.

The usage of specific design methods, based on iterative algorithms (Cojoc, 2002) or on the propagation and superposition of spherical waves (Cojoc, 2004), allows us to calculate phase-only DOEs able to generate complicated pattern of traps organized not only in plane but also in volume. Using e-beam lithographic techniques DOEs with high quality can be fabricated. Nevertheless, these optical ele

ments are static and can therefore be used only for multiple trapping without any possibility of moving the trapped particles together or independently (Garbin, 2005). The full utility of the DOEs in the field of laser trapping and micro-manipulation is realized when a computer addressed liquid crystal spatial light modulator LC-SLM (Holoeye, Hamamatsu Photonics) is used to project sequences of trap-forming DOEs almost in real time (Emiliani, 2005) so that by slightly displacing the traps from one pattern to the next the particles are transferred along arbitrary three-dimensional (3D) trajectories.

Section 2.1 introduces the sample preparation and the materials used. Section 2.2 reports a brief introduction to the basic theory of Optical Tweezers. The methods developed for multiple trapping by means of spatial light modulator (SLM) based technique and the algorithms used to calculate diffractive optical elements (DOE) projected to the SLM are described in section 2.3. Section 2.4 described the setup used for multi-view microscopy and optical manipulation. Finally, results achieved by using the multiple trapping technique are reported in section 2.5.

Materials

2.1 Sample preparation

In these experiments three kind of samples are involved: beads solution for testing 3D arrays, red blood cells (RBCs) for optical manipulation with multiple tweezers, and irregularly shaped pieces of glass from a break at one capillary end, which accidentally entered the sample chamber.

Beads in solution are prepared diluting 10 *µl* of 4.8 *µm* diameter 10% w/v silica particles (Bangs Laboratories) in 15 *ml* distilled water.

Human RBCs from a healthy female donor (me!) are prepared using about 3 *µl* of fresh blood diluted in 1.5 *ml* isotonic phosphate buffered saline (PBS) solution containing 15 *µl* ethylenediaminetetraacetic acid (EDTA) 0.5 *M* to avoid blood coagulation and 2.5 *mg* human serum albumin (HSA) to avoid RBCs aggregation. RBCs solution cannot be stored so fresh RBCs are used for each experiment.

Each sample substance is inserted in a square borosilicate glass capillary (100 *μm* inner side, 50 *μm* wall from CMS Microcells) attached on a narrow cut coverslip through a 50 *μm* sticky tape.

Theory and Methods

2.2 Optical tweezers

An effective optical tweezers set-up can be created with a handful of standard optical components. This instrument usually starts with a commercial optical microscope but adding extensive modifications. Optical Tweezers (OT) use light to manipulate microscopic objects (Ashkin, 1970). An OT applies forces in the *pN*-range and measures displacements in the *nm* range of objects ranging in size from 10 *nm* to over 100 μ*m*. Figure 29A shows a laser beam focused by a high-quality microscope objective to a spot in the specimen plane. This spot creates an "optical trap" able to hold a small particle at its centre. The forces felt by this particle consist of the light scattering and gradient forces due to the interaction of the particle with the light, Fig. 29B (Ashkin, 1986).

The basic principle behind optical tweezers is the momentum transfer associated with bending light. Light carries momentum that is proportional to its energy and in the direction of propagation. Any change in the direction of light, by reflection or refraction, will result in a change of the momentum of the light. If an object bends the light, changing its momentum, conservation of momentum requires that the object must undergo an equal and opposite momentum change. This gives rise to a force acting on the object. When this light interacts with a bead, the light rays are bent, and the sum of the forces from all such rays can be split into two components: $F_{scattering}$, the scattering force, pointing in the direction of the incident light (z, see axes in Fig. 29B), and $F_{gradient}$, the gradient force, arising from the gradient of the Gaussian intensity profile and pointing in x-y plane towards the centre of the beam (dotted line). The gradient force is a restoring force that pulls the bead into the centre. If the contribution to $F_{scattering}$ of the refracted rays is larger than that of the reflected rays then a restoring force is also created along the z-axis, and a stable trap will exist. Incidentally, the image of the trapped sample can be projected onto a quadrant photodiode to measure *nm*-scale displacements.

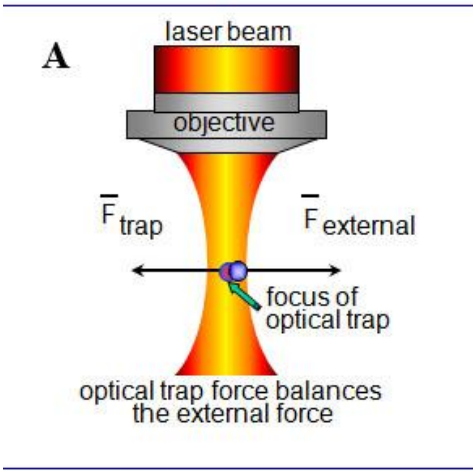

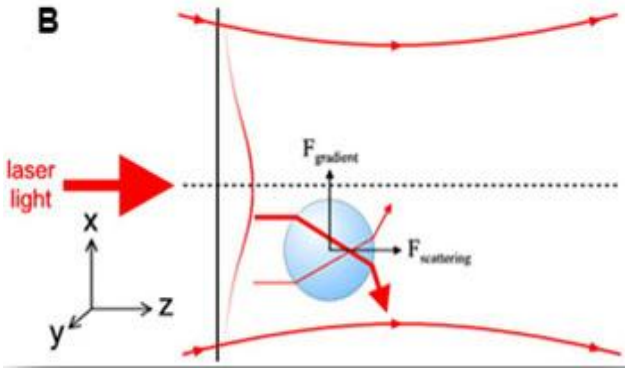

Fig. 29 Optical Tweezers Principles: (A) a laser beam focused by an objective to a spot in the specimen plane; (B) forces felt by trapped particles.

Optical Tweezers have been used to trap dielectric spheres, viruses, bacteria, living cells, organelles, small metal particles, and even strands of DNA. Applications include confinement and organization (cell sorting), tracking of movement (bacteria), application and measurement of small forces, and altering of larger structures such as cell membranes. Several guides exist detailing how to build a basic system, such as that by Block (Block, 1998). A comprehensive guide on how to construct a dual-beam tweezers system has been provided by Fallman and Axner (Fallman, 1997).

2.3 Holographic Optical Tweezers: DOE and LC-SLM

The introduction of holographic optical elements into optical tweezers set-ups has multiplied the possibilities of this technology for precisely trapping, moving, and manipulating micro-particles. First, static diffractive optical elements generated by computer and manufactured by photolithography enabled the simultaneous creation of several optical traps (Dufresne, 1998) (Dufresne, 2001). Conversion of the static trap arrays into dynamic light patterns by displaying the diffractive optical elements onto spatial light modulators was the next logical step (Reicherter, 1999) (Curtis, 2002). The use of laser beam shaping through diffractive optical elements enables the formation of complex optical trapping configurations. Exciting applications have been demonstrated, ranging from cell biology to colloidal sciences. Typically, holographic optical tweezers systems utilize a high numerical-aperture microscope objective to form an array of trapping sites in the objective's focal plane. It is possible, using iterative computer algorithms, to calculate the phase-only hologram that must be displayed on the liquid crystal spatial light modulator device to achieve the desired distribution of optical traps. Many experiments can benefit from the use of two or more optical traps to simultaneously trap more than one particle.

2.3.1 DOE design

Diffractive optical elements (DOEs) are optical elements that influence the wave field by diffraction (Cojoc, 2004 (2)). They can be designed to modulate the amplitude, phase, or polarization of an incoming beam. However, phase-only modulation has become the preferred mode for applications to optical tweezers because amplitude modulation implies diverting some of the incident beam energy from the desired output amplitude/phase distribution. Optical diffractive elements diffract only a portion of the incident light into the intended modes and directions. In these experiments only phase modulation holograms have been used, and these kinds of DOEs have a maximum theoretical efficiency of 40%. Phase modulation can be achieved through relief modulation, Fig.30. This technique allows us to generate arrays of spots disposed in different planes along the optical axis and to control the local phase.

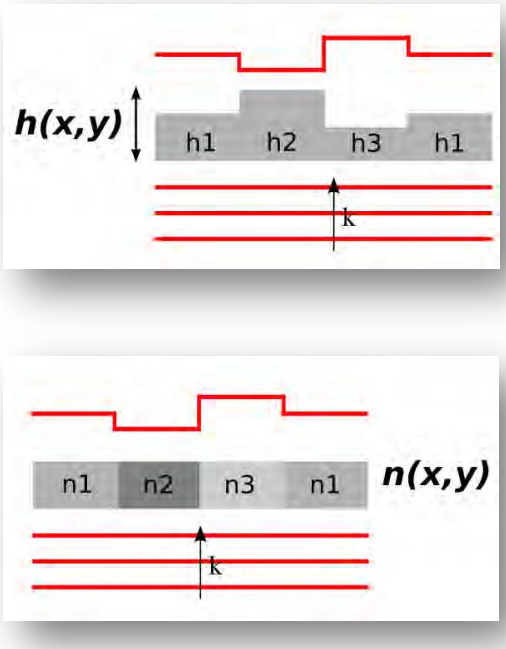

Fig. 30 A phase diffractive optical element encodes a pattern of phase shifts in thickness (A) or refractive index (B) modulation. A lane wave incident on the optical element acquires a spatially modulated phase.

When a wave front first enters the material, it is uniformly slowed to a speed $v = c/n$, where c is the speed of light in vacuum and n is the material's refractive index. Parts of the wave front traveling through thinner regions of the optical element propagate outside the material at speed c, while sections remaining in the material are further delayed, with a phase delay proportional to the extra thickness of material. Consequently the relative phase at $x = (x, y)$ is proportional to the thickness, $h(x)$:

$$\phi(x) = 2\pi(n-1)\frac{h(x)}{\lambda}$$

Similarly, phase delays can be encoded in a pattern of controlled variations of the index of refraction $n(x)$. The thickness h of the optical element is constant, and different segments of the wave front undergo different phase delays according to the different optical path lengths $\Delta(x) = n(x)h$. The computer-generated phase-modulation pattern can be etched on a transparent substrate (refractive index n) in surface relief with conventional lithographic processes (Dufresne, 2001). Using electron-beam lithography, DOEs with high spatial resolution and high spatial-bandwidth product can be generated (Cojoc, 2002). Holographic patterns can also be trans-

ferred to a spatial light modulator which imposes a prescribed amount of phase shift at each pixel in an array by varying the local optical path length. The use of computer-generated holograms in combination with spatial light modulators allows very quick hologram change, at video-frame rate or faster, which in turn allows dynamic trapping.

2.3.2 Phase retrieval using iterative algorithms: 2D DOEs

Phase retrieval using iterative algorithms allows us to find an optimum phase function or the DOE when a certain intensity distribution is desired in a plan after the DOE. Scalar diffraction approximation can be applied when the minimum structure size of the DOE, δ, is greater than the wavelength, λ ($\delta>2\lambda$). Ray tracing (Cojoc, 2002) and phase retrieval iterative algorithm (Garbin, 2007) are techniques to design DOEs under these assumptions. In order to provide high transmission efficiency, a phase-only DOE described by its phase function, $\phi(x)$, is considered. The main problem to be solved using iterative algorithms is to find the optimum phase function of the DOE, which, illuminated by a given beam, produces a desired intensity distribution in a plane after the DOE. Illuminating the DOE with a collimated beam, the diffracted field at a distance *z* after the DOE is given by:

$$E_0 = P_z\{A_g(x)exp[i\phi(x)]\}$$

where $A_g(x)$ is the amplitude of the illuminating beam in the plane of the DOE, and $P_z\{\cdot\}$ is the propagation operator (Fourier transform for far-field propagation, Fresnel transform for intermediate planes or angular spectrum propagation for near-field).

The goal is to calculate the phase function $\phi(x)$ of the DOE that produces an intensity distribution $I_0(x) = |E_0(x;y)|^2$ proportional to the desired intensity distribution $I_0(x)$. Phase retrieval using iterative algorithms starts with the initialization of the diffracted field $E_0(x;y) = A_0(x,z)\exp[I_0(x,z)]$. Since the phase is free, some different distributions have been tested to initialize the phase function: random, constant, Gaussian. Randomly generated distribution was found to give the best result. One cycle of the iterative algorithm follows the sequence:

- back-propagate the field $E_0(x;z)$ to the DOE plane using the inverse transform;

- replace the amplitude of the resulted field by the amplitude of the illuminating beam, $A_g(x)$, while the phase is kept unchanged;
- propagate the field at the distance z;
- replace the amplitude of the resulting field by the desired amplitude, $A_{0i}(x)$, and calculate the mean square error (MSE) between the desired and obtained intensities.

Repeating this cycle, the MSE decreases monotonically until the change of the MSE becomes insignificant and the iterative algorithm is stopped. The phase, calculated in the second step of the last iteration cycle, represents the phase function of the DOE.

2.3.3 Spherical wave propagation and superposition: 3D DOEs

The techniques based on iterative algorithms allow us to obtain DOEs with very good performances for 2D intensity distributions. To achieve 3D intensity distributions, the spherical wave propagation and superposition approach is used (Cojoc, 2004) (Moradi, 2007). The assumption is made that the DOE, illuminated by a set of point sources, generates a set of spots arranged in a prescribed configuration. This approach allows direct calculation of the DOE, avoiding the use of iterative algorithms. Assuming that both light source and generated pattern can be described by point sources that emit spherical waves, the phase function is derived from the propagation and superposition of the spherical wave fronts in the plane of the DOE (Cojoc, 2001). If the DOE is a thin element described by the transmittance function $t(x) = \exp[i\phi(x)]$ and $W_{in}(x;0)$ is the complex amplitude of the incident wave, the complex amplitude of the output wave after the DOE will be: $W_{out}(x\,0) = t(x)W_{in}(x;0)$, where $z=0$ denotes the DOE plane. For a given input-output pair of waves satisfying the condition $|W_{in}(x;\,0)| = |W_{out}(x;\,0)|$ the phase function is given by:

$$\phi(x) = \{\arg[W_{out}(x;0)] - \arg[W_{in}(x;0)]\} \bmod 2\pi$$

If $\{P_s(x_s;z_s), s = 1 : N_s\}$ is the set of N_s points describing the source and $\{P_g(x_g;z_g), g = 1 : N_g\}$ the set of N_g points describing the generated spots, the expression for the incident and output wave fronts at the point $P_e(x_e;0)$ in the DOE plane will be:

$$W_{in}(x_e;0) = \sum_s a_s \cos\psi_{s,e} \frac{\exp(ikr_{s,e})}{r_{s,e}}$$

$$W_{out}(x_e;0) = \sum_g a_g \cos\psi_{g,e} \frac{\exp(ikr_{g,e} + \varphi_g)}{r_{g,e}}$$

where $a_{s(g)}$ are constants representing the strength of the point source, $\cos\psi_{s,e=}{}^{z_s}/_{r_{s,e}}$ is the obliquity factor, $r_{s,e} = P_sP_e$ is the distance between the source point P_s and the element P_e of the DOE, $r_{g,e} = P_gP_e$ is the distance between the source point P_g and the element P_e of the DOE and k is the wavelength number $k = {}^{2\pi}/_{\lambda}$. The number of the sampling points N_e is limited by the scalar diffraction approximation to: ${}^{D}/_{2\lambda} < N_e < {}^{D^2}/_{\lambda z}$, where D is the lateral size of the DOE and z the distance from the source plane or the plane of the generated spots to the DOE. Figure 31 shows a sequence of desired spots distribution (A), DOE calculation (B) and reconstructed output distribution (C); while Fig.32 shows some examples of DOEs, calculated using the spherical waves propagation method, which generate two- and three-dimensional configurations of focused laser spots.

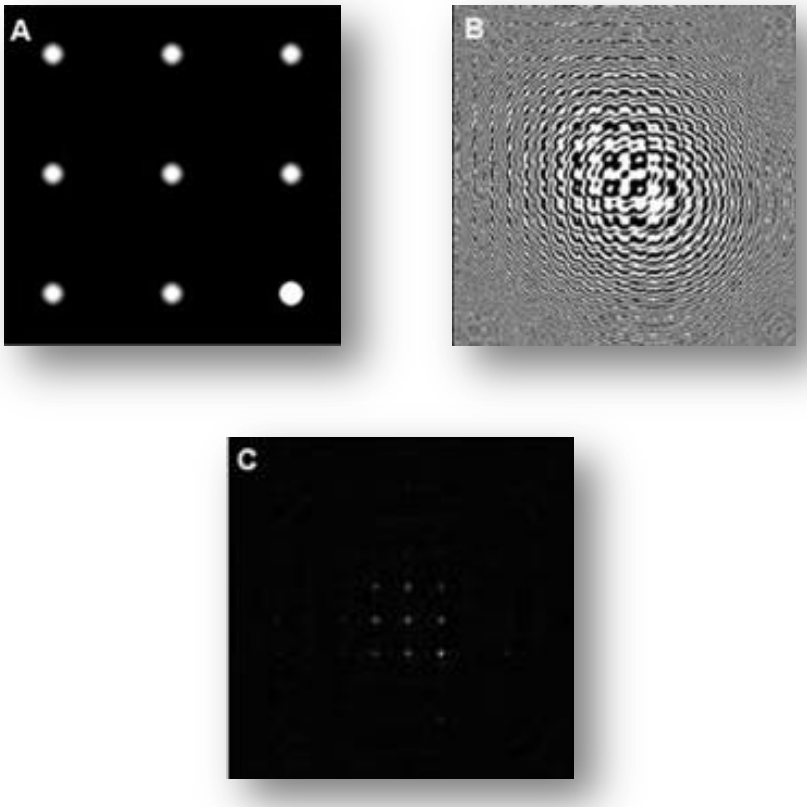

Fig. 31 Desired output intensity distribution (A). DOE calculated with the spherical wave approach (B). Reconstructed output intensity distribution, computer simulated (C).

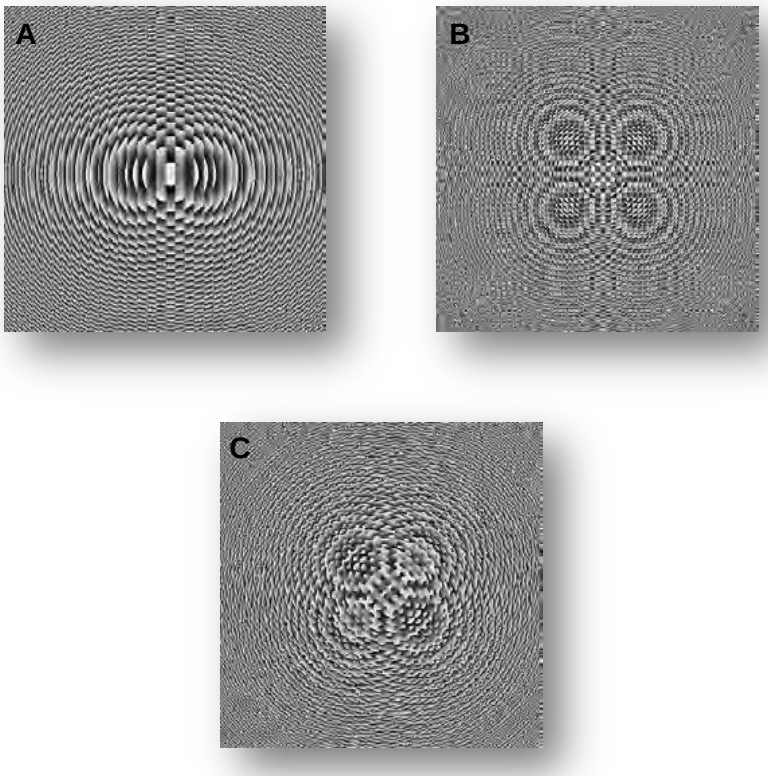

Fig. 32 DOEs calculated using the spherical waves approach. The DOE in (A) generates two spots and the DOE in (B) four spots; in both cases the generated spots are arranged in a two-dimensional array. The DOE in (C) generates five spots, arranged in three-dimensional configuration.

2.3.4 LC-SLM: design and operation

An SLM imposes a prescribed amount of phase shift at each pixel in an array by varying the local optical path length. Typically, this is accomplished by controlling the local orientation of molecules in a layer of liquid crystal. Liquid Crystal SLMs, commercially available, can be broadly divided into two groups: devices that are electronically addressed and devices that are optically addressed. Moreover, the choice of liquid crystal material is significant: ferroelectric liquid crystal devices can be fast, operating in the *kHz* regime, but are limited by the small number of grayscale levels, or bit depth, that can be achieved. Nematic devices, on the other hand, are much slower, with refresh rates of the order of ~ 10 *Hz*.

Nematic devices are popular however because they offer far greater bit depth than ferroelectric devices, allowing more complex holograms to be displayed. Nematic SLMs are also generally more efficient than ferroelectric devices in terms of the proportion of light sent into the first diffraction order. This can be an important consideration for holographic optical trapping. Spatial light modulators can be reflective or transmissive, the choice depending largely on the nature of the application. In this work an electrically addressed nematic LC device, constructed on a reflective substrate, has been used. Since nowadays the minimum pixel size for SLMs is around 6 *μm*, with a maximum fill factor of 95%, and the number of pixels is limited to about 2 *Mpixels*, the quality of the diffracted pattern is lower than that obtained with DOEs fabricated by means of e-beam lithography. This is the price to be paid for dynamic control of the trapping array configuration. However, for many applications there is a good compromise between dynamic control and the quality of the generated trapping pattern.

An SLM was first used in 1999 by Reicherter et al. (Reicherter, 1999). They used a modified spatial light modulator, adapted from a display projector, to create two-dimensional arrays of traps using simple phase-only hologram. Trapping was extended to two planes through the addition of a lens by Liesener et al. (Liesener, 2000). Subsequently, Curtis et al. (Curtis, 2002) extended this method, realizing full dynamic control over a three-dimensional trap distribution. This method can be extended to the creation of arrays of optical vortices (Cojoc, 2005), enabling the trapping of low-index particles in three dimensions.

When a computer addressed liquid crystal spatial light modulator LC-SLM is used to project sequences of trap-forming DOEs, almost in real time, particles are moved along three-dimensional trajectories, overcoming AOD limitations to planar configuration of traps. On the contrary, the main SLMs drawbacks are, in fact, that LC-SLM are typically pixel devices and have a finite resolution. The first problem that the ‘pixelisation’ introduces is due to diffraction. A considerable amount of light is lost to the multiple diffraction orders an SLM generates. Fortunately, efficiencies remain high enough to enable optical trapping. Another side-effect of the finite resolution of an SLM is aliasing. Aliasing can lead to a loss of fidelity in the system as the intensity is distributed elsewhere than the desired trap locations. This can lead to a reduction in the trapping strength and may correspondingly limit the effectiveness of three-dimensional optical tweezers.

2.3.5 Electrically addressed SLMs (EASLM)

Electrically addressed SLMs typically consist of a layer of liquid crystal sandwiched between a transparent electrode and a patterned silicon substrate. The image on an electrically addressed spatial light modulator is created and changed by shining light encoded with an image on its front or back surface. A photo-sensor allows the EASLM to sense the brightness of each pixel and replicate the image using liquid crystals. In this work the electrically-addressed device was manufactured by Hamamatsu and is a phase programmable modulator (PPM) (X8267 model), Fig.33.

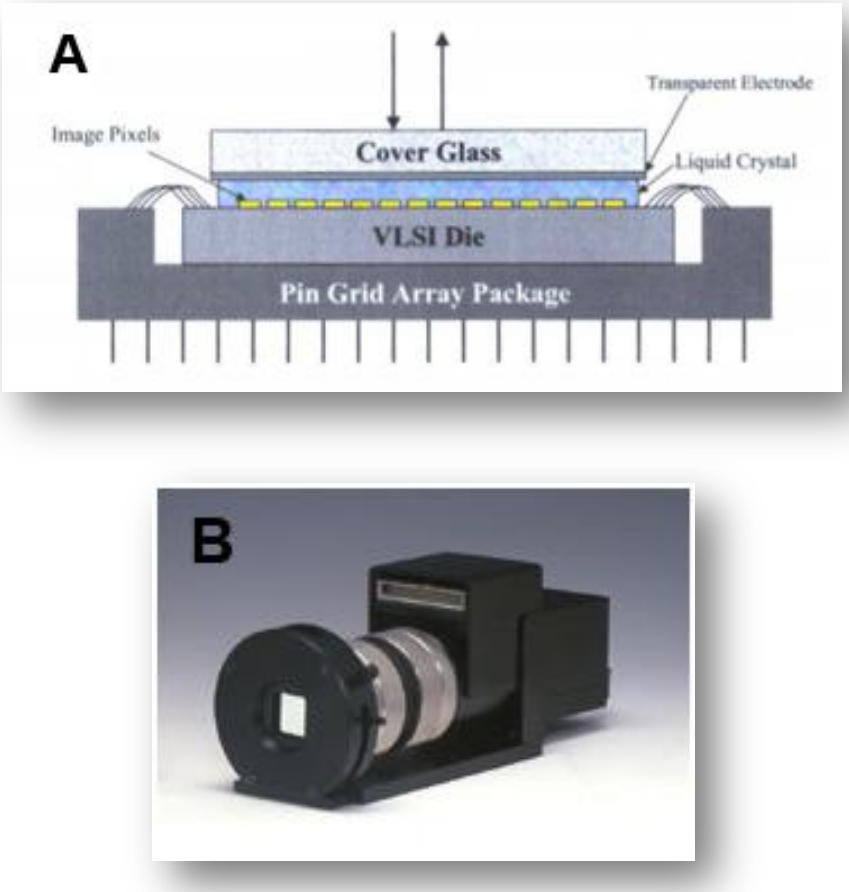

Fig. 33 (A) A cross-section of a LC-SLM; (B) A photo of the device.

The silicon substrate is manufactured as a electrically-addressable array of pixels. The voltage at each pixel is determined by the corresponding pixel value in an 8-bit grayscale image array sent to the device from the computer. The voltage sets up a localized electric field across the liquid crystal layer. If no electric field is

applied, the liquid crystal molecules align in the nematic phase. This is characterized by the molecules, which are rod-like in shape, all pointing in generally the same direction. Their alignment can be controlled by creating suitable microstructures on the walls of the device during fabrication. The device contains a transparent electrode on one side of the cell and a reflective pixel array of electrodes on the other. Applying a voltage across these electrodes sets up an electric field across the liquid crystal layer. The molecules are polar and so will tend to align with an applied electric field. The final degree of molecule rotation is determined by the competition: the strength of the desire of the molecules to retain their natural semi-ordered nematic phase versus the strength of the applied electric field. For light incident upon the device, the effective refractive index of the liquid crystal layer changes as the molecules rotate. The effective path length and the phase of the light as it exits the device can therefore be controlled by varying the electric field and therefore the degree of rotation of the liquid crystal molecules. Figure 34 shows how a nematic liquid crystal device operates.

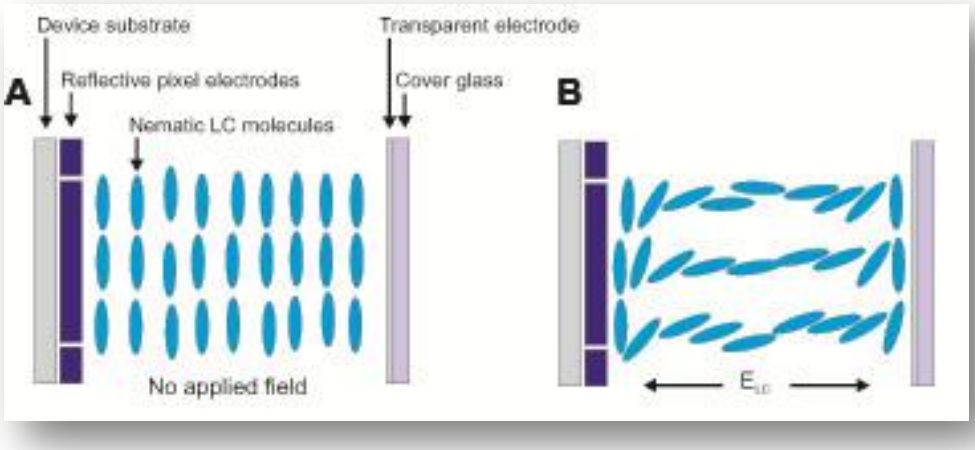

Fig. 34 Illustration showing the principle behind the device. (A) With no applied field, the elongated liquid crystal molecules form a nematic phase, with orientation determined by the fine structure of the chamber walls. (B) The polar molecules align with an electric field created by applying a voltage across the electrodes.

The Hamamatsu LC-SLM used in the our experiments allows a very good phase modulation (absolute phase shift > 2π, and more than 64 intermediate phase levels), covers a wide range of wavelengths (the total range, using different modules, is 400- 1500 *nm*) and has a good spatial resolution (12.5 *μm*) and SBWP

(1025x768). The main drawback is the relatively low frame refreshing rate (60 Hz) characteristic of all nematic LCDs.

2.4 Multi-View Microscopy and Optical Manipulation setup

The setup shown in Fig.35 is based on a conventional single-beam gradient force trap path which uses a high NA objective (MO1) (Olympus LUM Plan Fl 100X, water immersion, NA=1, WD= 1*mm*) in inverted position and takes advantage of a second objective with moderate NA (MO2) (Olympus SLC Plan Fl 40X, NA=0.55, WD=7 *mm*) to monitor the sample volume from a direction orthogonal to the trapping objective MO1. The trapping optical path (red path) is composed of the fiber laser source (LS) (IPG Photonics YLM-10) which delivers a collimated linearly polarized CW laser beam at 1064 *nm*, the phase programmable modulator (PPM) (Hamamatsu PPM-X8267), the dichroic mirror (DM) and the trapping objective (MO1). The wave-front of the trapping beam is shaped by the computer generated DOEs addressed to the PPM to generate multiple traps in 3D geometries and animate them in real time through a Matlab (MathWorks) programmed Graphical User Interface (GUI) which is also used to handle the imaging.

The conventional imaging path is composed by the fiber illumination source (I1), trapping objective MO1, mirror M, tube lens (TL1) and CCD camera (C1) (DVC 1412AM-T2-LV). The second imaging path, orthogonal to the first, is composed of the fiber illumination source (I2), lateral objective MO2, tube lens (TL2) and CMOS camera (C2) (EPIX Silicon Video 1281). The trapping objective MO1 is mounted on a nano-focusing piezo-stage (Physik Instrumente P-725) which enables axial displacement with 2 *nm* resolution. The relative position of the two microscope objectives MO1 and MO2 is illustrated in Fig.35B. Since the inclusion of the lateral objective, the conventional sample chamber built with two microscope coverslips has been replaced by a square borosilicate glass capillary (100 *μm* inner side, 50 *μm* wall from CMS Microcells) attached to a narrow cut coverslip through a 50 *μm* sticky tape (inset Fig.35A).

The sample chamber is then positioned on a bridge-shaped metallic support connected to a three-axis motorized stage (Physik Instrumente M-111.1DG) to move the sample chamber with 100 *nm* resolution and allow fine positioning of the sample under investigation in the field of view of both MO1 and MO2 microscope objectives.

The glass capillary can also be connected to a micro fluidic circuit with syringe pumps to control the flow of the fluid in which the samples are suspended. This configuration allows to illuminate and acquire transmission images from two orthogonal observation directions while performing multi-trapping through the trapping objective MO1. Since the total efficiency of the optical trapping path for the 1064 *nm* wavelength is estimated to be 15%, a maximum power of 150 *mW* reaches the sample for an output laser power of 1 *W*. The heating of the sample originated by the laser beam absorption is estimated from the literature to be in the order of 10°*C* per *W* of laser power (Dholakia, 2006). Therefore the maximum increment of the temperature in the trapping environment is estimated to be 1.5*ºC*.

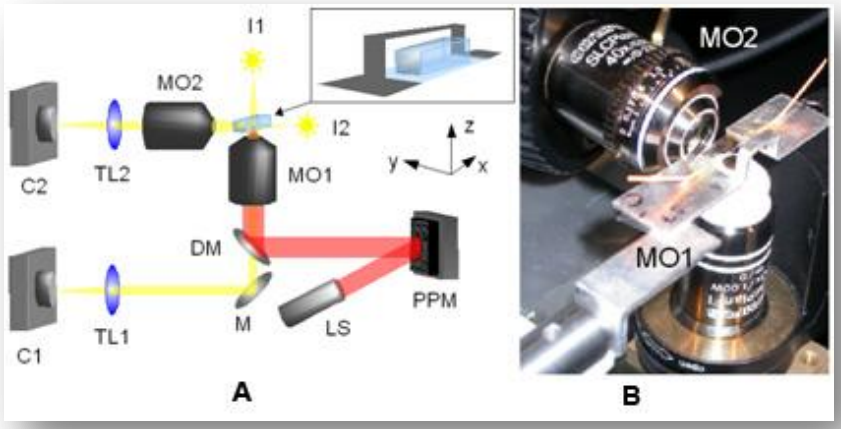

Fig. 35 (A) Schematic of the multi-view optical tweezers setup (not to scale). The red path corresponds to the trapping laser while yellow indicates the imaging paths. I1,I2: illumination, MO1,MO2: microscope objectives, DM: dichroic mirror, M: aluminium mirror, TL1, TL2: tube lenses, C1, C2: cameras, LS: laser source, PPM: programmable phase modulator. In the inset a detail of the sample chamber is represented; (B) A picture of part of the setup showing the two microscope objectives and the sample cell.

2.4.1 Trap stiffness calibration

Trap stiffness calibration was performed using the drag force method (K. C. Neumann, 2004). A single 4.8 *μm* diameter silica bead was trapped inside the capillary and positioned using the piezo-collar at 50 *μm* height from the bottom glass surface in order to minimize the effect of a near surface on the drag force. Different known drag forces were applied to the bead by moving the three-axis stage at a constant speed along the long axis of the capillary. Forces corresponding to each velocity were calculated using the Stokes drag force equation, $F=6\pi\eta rv$, where η=0.001 *Pa s* is the viscosity of the fluid, *r* is the radius of the bead and *v* is the ve-

locity of the fluid. The displacement of the bead from its equilibrium was measured from the images with an accuracy of about 20 *nm*. Then the stiffness of the trap was calculated, according to the elastic behaviour of an optical trap, as $k=F/x$.

To prove the effect of the squared sample chamber on the quality of the trap, the trap stiffness was measured in two different conditions: using first a conventional sample chamber with two coverslips and then using the sample chamber described above. The laser beam had to pass, in the second case, through the coverslip, the adhesive tape and the bottom wall of the capillary (50 *μm* thickness) and therefore a loss in the trap strength was expected. This was confirmed by the experimental results shown in Fig.36. Keeping the laser power constant, larger displacements of the bead from the equilibrium position were observed when using the squared capillary sample chamber (Fig.36A, fluid velocity – bead displacement curve).

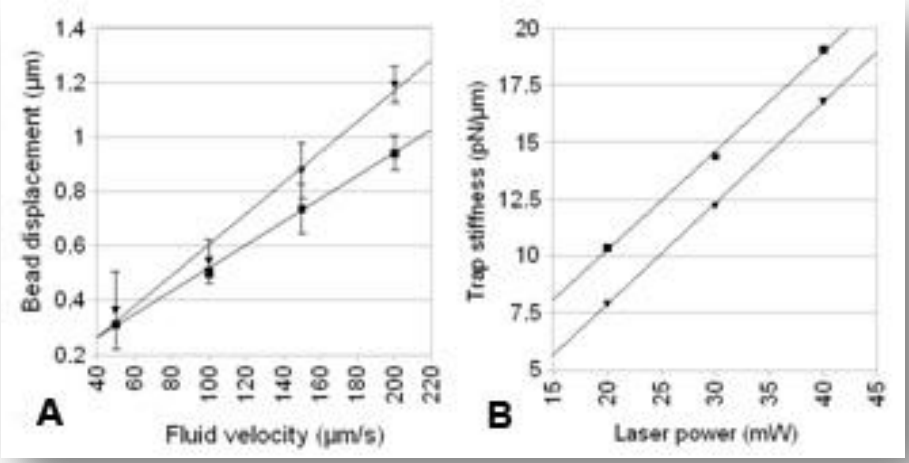

Fig. 36 Trap strength for a 4.8 μm silica bead in the conventional sample chamber (squares) and in the squared capillary sample chamber (triangles). (A) Beads displacement as a function of the fluid velocity; laser beam trapping power: 20 mW. (B) Calculated stiffness at different laser intensities.

The loss in strength can be evaluated as trap stiffness loss, which in the case of a laser power of 20 *mW* at the specimen plane dropped from 10.4 $pN\ \mu m^{-1}$, when using the coverslip only, to 7.9 $pN\ \mu m^{-1}$, when using the sample cell. The same measurements were performed at different laser intensities, showing that in both conditions the increase of the trap stiffness while increasing the power is the same (~0.44 $pN\ \mu m^{-1}\ mW^{-1}$) even if the two trends are separated on average by 2.5

pN μm^{-1} (Fig.36B). This means that the losses in the trapping performances due to the sample cell design, required for having multi-view capabilities, can be compensated by just increasing the laser power about 28%.

2.4.2 DOE calibration

The distance between the SLM and the microscope objective (MO) first principal plane is D. The laser beam is reflected and modulated by the SLM in an array of spots focused on the plane F_{SLM}. This plane is imaged by the microscope objective at a distance z from its focal plane F_{MO}; f_{SLM} and f_{MO} are the focal lengths of the DOE implemented on the SLM and of the objective (Emiliani, 2005). From the scheme in Fig.37, by applying the conjugation equation written in focal coordinates for the MO, we have:

$$zz' = -f_{MO}^2$$

where:

$$z' = f_{SLM} + f_{MO} - D$$

Introducing this equation into the previous equation, we obtain a simple expression which relates the focal length f_{SLM} to the axial trapping position z:

$$f_{SLM} = D - f_{MO} - \frac{f_{MO}^2}{z}$$

Once the two fixed parameters D and f_{MO} are known, the last equation allows us to derive for each position of the trapping plane, z, the focal length, f_{SLM} and *vice-versa*. The values for D and f_{MO} were obtained by fitting the experimental curve shown in Fig.38 to experimental data of different focal length DOEs (f_{SLM}) and their focus z. From the fitting of the curve, we derived the following values: D=777 *mm* and f_{MO}=1.28 *mm*.

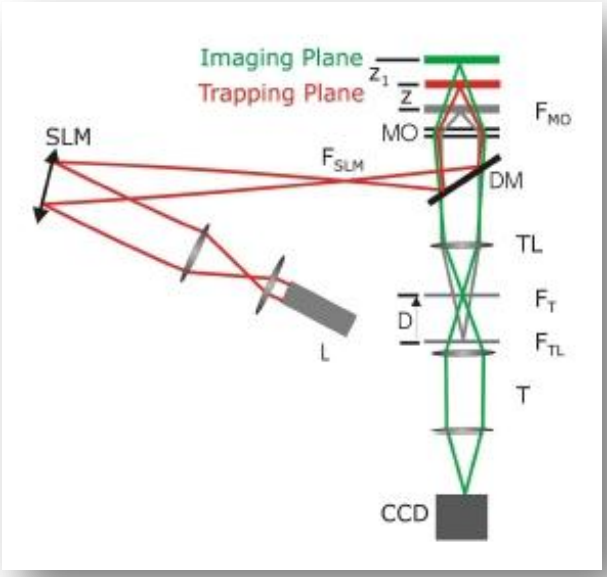

Fig. 37 Schematic of the trapping (red line) and the imaging (green line) beam paths.

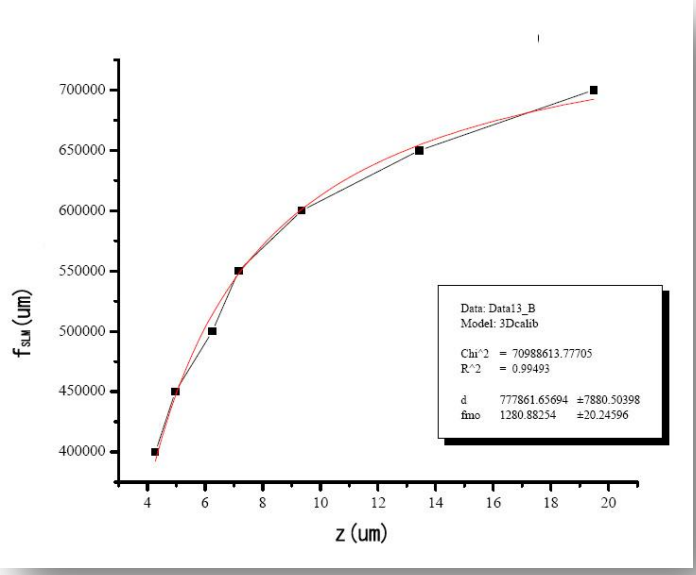

Fig. 38 Calibration curve of the DOE focal length versus the trapping plane position.

Results

2.5 Optical Manipulation results

Using DOEs we demonstrated multiple trapping into a distribution of laser spots that can be organized in planar and volume configuration. Moreover, since the SLM is a dynamic device, we could manipulate the trapped particles in real time. In these investigations, beads solution are involved to test the dynamic manipulation of 3D arrays of traps. Trapping is then extended to RBCs which are trapped and rotated inside the glass capillary on different axes of rotation. Since the home made sample cell can be easily integrated into a micro-fluidic system, the setup can be used as it is to investigate the viscoelastic properties of RBCs (Svoboda, 1992) (Abkarian, 2007) (Bambardekar, 2008) or, more in generally, cell membranes while they are under a shear flow. The tomography of the trapped beads array and the RBC is also reported. Finally, manipulation of a irregularly shaped objects is also shown to demonstrate the effortlessness achieved in trapping by using an approach based on DOEs implemented on a PPM driven by a GUI.

2.5.1 Optical manipulation of multiple-beads in 3D arrays

Two-dimensional and three-dimensional arrays of trapped beads, obtained by calculating and addressing a DOE to the PPM through the GUI, can be positioned inside the sample chamber using the three-axis motorized stage. The stage moves the entire capillary while the beads array remains fixed by the laser in the field of view of both microscopes. The position along the optical axis of the trapping microscope can be refined by moving the microscope objective piezo-collar. Moreover, the dynamic manipulation of the array through the PPM is fully exploited by generating in real time a number of DOEs which control the position of each individual trap along a custom trajectory as well as the strength of each one (Moradi, 2007), dramatically increasing the number of configurations that can be achieved.

Figure 39a shows the sketch of a 3D array of four 4.8 *μm* beads (represented in dark gray) which are then imaged through the lateral objective (Fig. 39b) and the trapping objective (Fig. 39c). The light gray bead represented in Fig. 39a is an alternative position encoded in a DOE for the left-top bead as shown in Fig. 39d-e. Fig. 39f-o shows selected frames from a 180° rotation lasting 4 seconds around the optical axis of the trapping objective.

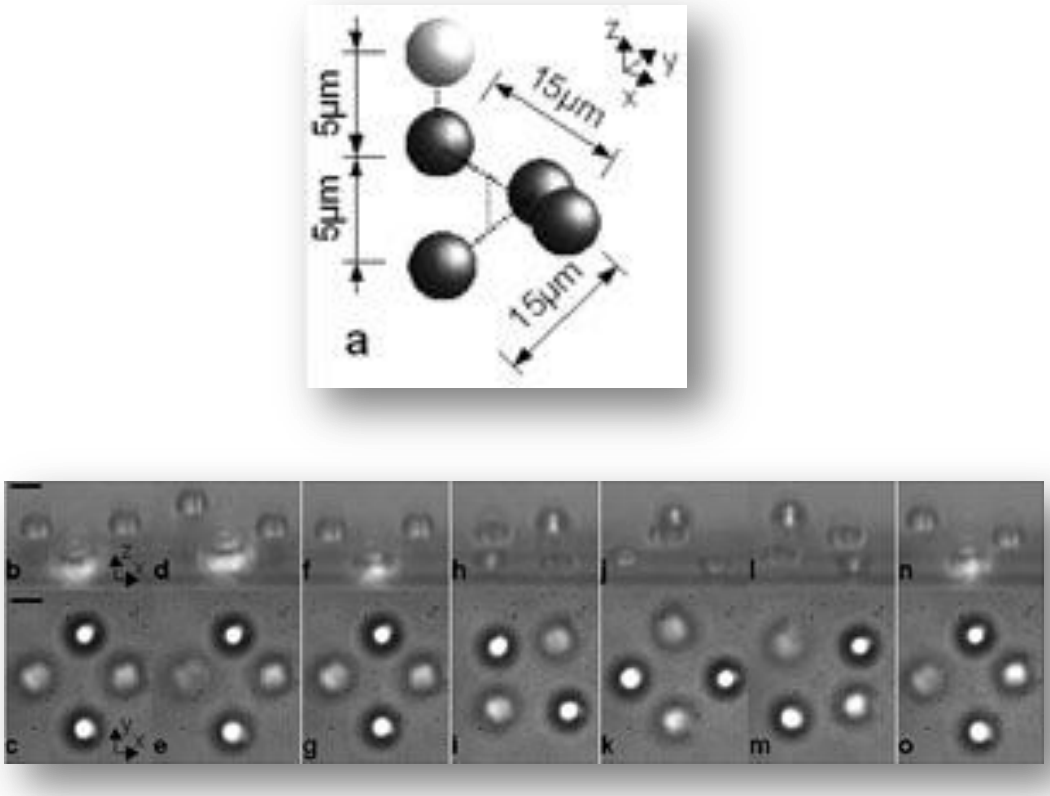

Fig. 39 Manipulation and multi-view microscopy of a 3D array of 4.8 μm silica beads. (a) A sketch of the array configuration. The light gray bead represents an alternative position for the bead as shown in panels d-e; (b-c) lateral view, b, and bottom view, c, of the array depicted in a; (d-e) individual bead displacement: the top-left bead in panel d is in the position represented by the light gray bead in panel a; (f-o) lateral view and bottom view pictures of a 180° rotation around the optical axis of the laser. All scale-bars are 5 μm.

2.5.2 Optical manipulation of RBCs with multiple tweezers

When non-spherical objects are manipulated, they tend to position their major axis of symmetry along the optical axis of the trapping laser. However, the alignment of the object along any axis can be obtained by changing the laser intensity profile (S. K. Mohanty, 2004) or using multiple trapping (Cojoc, 2005). Hereafter we combine lateral imaging with multiple-trapping of individual particles having a disk like shape such as red blood cells (RBCs), Fig.40.

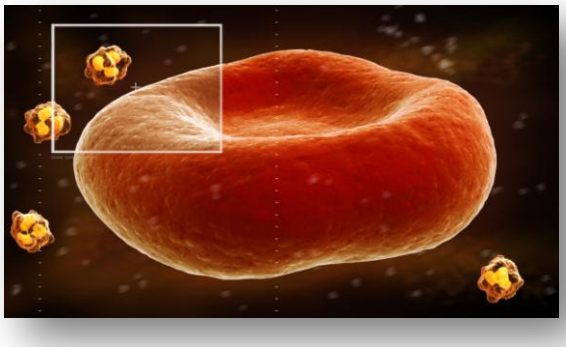

Fig. 40 A red blood cell.

Figure 41 show the manipulation of a RBC trapped by a 2D array of four traps configured in a square inscribed in the trapped disk and having the side of 5 *μm*. Figure 41a-j shows lateral and bottom pictures of the trapped RBC while the trapping array plane is perpendicular to the bottom surface of the capillary and it is rotated around the optical axis of the laser. Figure 41k-l shows a RBC trapped by the same array but having the plane parallel to the sample cell bottom and then tilted (Fig. 41m-n) by 15°.

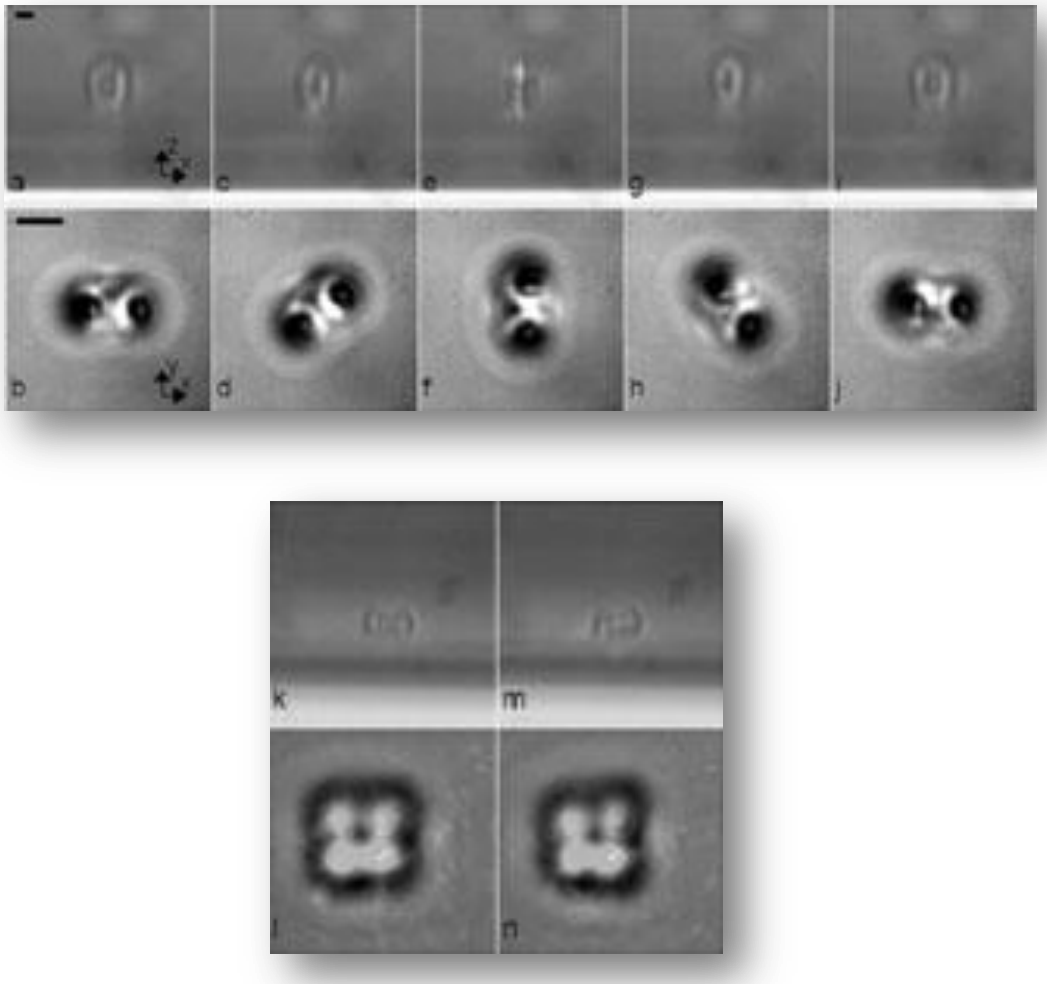

Fig. 41 Multi-axis rotation of a trapped RBC. (a-j) Lateral view (top) and bottom view (bottom) of the 180° rotation around the optical axis of the trapping objective: selected frames from a four-seconds sequence (media 2); (k-l) the RBC trapped horizontally in relation to the bottom surface of the sample cell; (m-n) the same RBC tilted by 15°. All scale-bares are 3 μm.

The advantage of having two orthogonal views while manipulating in three dimensions non-spherical shaped objects like RBCs is evident: the real placement of the cell in relation to the surrounding micro-fluidic environment would be difficult to appreciate and control using only the conventional transmission imaging path that most optical tweezers setups use.

2.5.3 Optical manipulation of arbitrarily shaped objects

Let us extend the multi-trap combined with multi-view imaging to an object with an irregular shape (Fig.42). A piece of glass is trapped by two traps positioned trough the GUI to be coincident with the two top corners of the object and by a third trap on the bottom of the grain to increase stability. By maintaining the configuration of the traps array while changing the angle around any rotation axis, the entire glass grain can be rotated to image the object from different points of view through the lateral microscope (Fig.42a,c). The ability to manipulate an irregular object, given very precise information about its position in the 3D space of a micro-fluidic environment has a great potential in the field of assembly of nano/micro-structures driven by optical tweezers (K. Castelino, 2005).

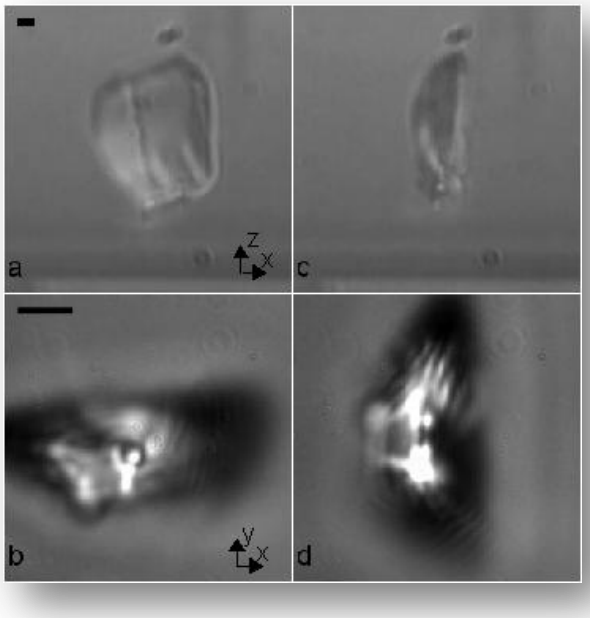

Fig. 42 Positioning of a irregularly shaped glass piece. (a-b) Lateral, a, and bottom, b, pictures of the trapped object; (c-d) the object is rotated 90°. All scale-bars are 3 µm.

2.5.4 Optical tomography of samples rotated by multiple tweezers

Another potential application of the instrument is the tomography approach to the reconstruction of 3D volumes from 2D images (Fauver, 2005). In fact, the rotation of one or more trapped objects with a very well defined angle, obtained as described above, and the simultaneous acquisition of images from the lateral microscope allow the three dimensional reconstruction of the sample volume.

Figure 43a-c shows three lateral images from the same plane selected from a set of 36 where two trapped 4.8 *μm* beads are rotated 360° around the optical axis of the laser by 10° each frame. All the lateral images are processed using TOMOJ (TOMOJ Plugin, Institute National de la Santé et de la Recherche Médicale, U759, France, http://u759.curie.u-psud.fr/softwaresu759.html), which is available as a plugin for *Image J* (National Institute of Health, USA, http://rsbweb.nih.gov/ij/index.html), obtain the 3D volume reconstruction. Fig. 43d-f shows three different sections of the calculated volume corresponding, from top to bottom, to the lines drawn in Fig.43a. Similarly, the lateral images from the same set depicted in Fig.41, representing a complete rotation of a RBC, were processed to obtain a 3D volume of the RBC. A section of this volume, parallel to the sample cell bottom slide, is shown in Fig. 43h and has to be compared with the real image from the same sample acquired from the trapping objective (Fig. 43g).

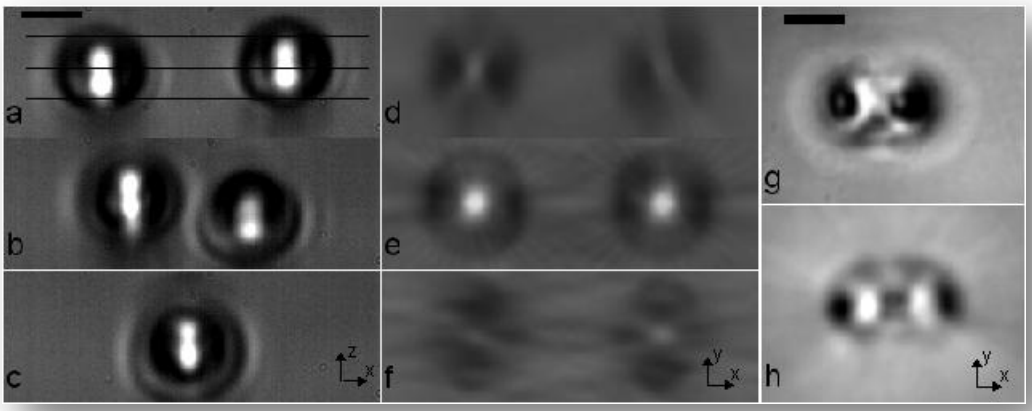

Fig. 43 3D volume reconstruction from lateral transmission images of rotating samples. (a-c) Three images from a set representing the rotation around the optical axis of the laser of two 4.8 μm beads; (d-f) three sections of the 3D volume corresponding to the lines depicted in a (top=d, middle=e, bottom=f); (g) A transmission image from the trapping imaging path of a trapped RBC; (h) a section from the 3D volume reconstructed from rotation images shown in Fig. 33. All scale-bares are 5 μm.

Conclusion

We have explored how phase DOEs to carry out new and complex optical functions in microscopy. The holographic optical tweezers setup benefits from a relatively high-resolution, lateral-view microscope, which allow fine positioning of the

trapped objects within a micro-fluidic chamber and gives a feeling for the real 3D volume in which the optical tweezers is operating.

The instrument has wide-spread applications in diverse fields of research: nano-technology, where the inspection and characterization of micro-fluidic devices is an issue and the use of optical tweezers as a tool for bottom-up assembling of complex 3D architectures from individual nano-objects is a challenge; and in cell biology, where biophysical characterization of cells under a shear flow is of great interest and where topographic 3D imaging techniques could complement the more expensive confocal or multi-photon microscopy. The combination of state-of-the-art trapping capabilities with a computer user interface gives us a state-of-the-art tool for manipulation and force characterization.

For the work carried out in this section I acknowledge Dr. D. Cojoc and Dr. E. Ferrari.

Appendix A

Nanoscale characterization of gliadin proteins adsorbed on solid surfaces

Wheat grains comprise water-soluble starch (polysaccharides) and water-insoluble gluten made of storage proteins: glutenins and gliadins. When wheat flour is mixed with water to obtain the dough used to make bread, pasta and other food products, storage proteins give the dough viscoelastic properties that are crucial for dough processing such as leavening and baking. Storage proteins have been extensively studied in light of applications in agricultural and the food industry. However, the mechanism of gluten accumulation are not well understood at the molecular scale (Banc, 2007). In developing grains, glutenins and gliadins are secreted from the cell in the form of micrometer-sized organelles that contain up to 80% protein. Understanding the formation of such organelles, their interactions with and passage through the cell membrane, and their organization outside the cell could lead to a better control of the quality of wheat flour in terms of nutritional properties and processability. This study is also relevant to medicine as gliadins are central to the pathogenesis of celiac disease, a multi-factorial disease affecting approximately 1 out of 100 individuals in the European population, that is believed to result from a deregulated immune response to wheat gliadin.

Storage proteins belong to the extracellular matrix where biological interactions with other molecules are limited. We can therefore neglect these interactions and focus on the physical-chemical properties of the protein that lead to molecular structure and self-assembly at the nanometer scale. Following this approach, storage protein may find applications outside the domain of food science, for example as biocompatible and biodegradable plastic materials and edible films (Yang, 2007).

We have used Atomic Force Microscopy (AFM) to study the surface adsorption and self-assembly of gliadins on a mica surface from various solvents. We worked in collaboration with Laurence Navailles and Amélie Banc of the Centre de Recherche Paul Pascal of Bordeaux (CRPP), who kindly provided the purified proteins. Our work followed a series of optical microscopy and dynamic light scattering studies conducted at the CRPP on the self-assembly of gliadins in water solutions and at air-water interface (Banc, 2007). These studies have shown that gliadins form ho-

mogeneous monolayer at the air-water interface. At high molecular areas, these proteins are low folded and secondary structures are oriented flat relative to the interfacial plane.

Our aim was to visualize these aggregates when they become adsorbed on a solid surface of mica and to reveal possible aggregation structures peculiar to the protein-surface interaction. Our results, although preliminary, show that gliadins aggregate in large globular objects in water solutions and adhere weakly to the mica substrate. In mixtures of water and ethanol, gliadins form layered droplets and extended multi-layers which are clearly due to a strong interaction with the surface, likely combined with an amphiphilic character of the protein. Adsorbed gliadins show interesting morphological analogies with surfactant multi-layers and the bi-continuous structures formed by block copolymers during microphase separation.

Materials and sample preparation

Gliadins are divided in three groups, α–, γ– and ω–types, on the basis of their amino acid sequences (Shewry, 1990) (Jones, 1959). The α– and γ–types have a molecular weight MW=30-40 *kDa* and consist of two distinct domains: a N-terminal repetitive domain rich in glutamine and proline residues, and a non-repetitive C-terminal domain containing intramolecular disulfide bonds. The C-domain is also more hydrophobic than the N-domain and could give the protein an amphiphilic character. ω–type gliadins have a molecular weight MW=40-80 *kDa* and consist of a single repeated sequences rich in glutamine, proline and phenylalanine without cysteine residues for disulfide bond formation (Tatham, 1995).

The molecular composition and dimensions of different gliadins determined by X-ray diffraction are summarized in Table 1: α-and γ-gliadins are more compact structures than the ω-gliadins, but ω–gliadins are globally more polar (Banc, 2007). X-ray diffraction shows a certain anisotropy of the molecular shape, with length L and diameter $d<L$ (Table 1).

Appendix A

Protein	MW (kDa) (molecular weight)	R_g (nm) (gyration radius)	d (nm) (diameter)	L (nm) (length)	L_c (nm) (contour length)
γ–gliadin	30-40	3.80	3.25	12.5	17.7
ω–gliadin	40-80	4.60	3.25	15.4	26.3

Table 2 Molecular characteristics for different gliadins.

Gliadins are generally insoluble in water (Young, 2007). They are particularly insoluble close to their isoelectric point IEP=6-7, little soluble for basic pH and more soluble for acid pH. Gliadins show a maximum solubility in water solutions containing 50% to 70% in volume of alcohol (Martin, 1931). In our experiments, lyophilized γ- and ω–gliadins were dissolved in purified water solution or phosphate buffer (PB) solution at neutral pH. The PB solution contains 3.5 mg/mL Na_2HPO_4 and 3.0 mg/mL NaH_2PO_4 in purified water together with sodium azide (NaN_3) to avoid bacterial contamination. Solutions were stirred at 25-30°C using a small Teflon magnetic stirrer for about 15 h. After stirring, the solutions were centrifugated for 1/2 h at 1000 rpm. After centrifugation, the pellet was removed and the solutions were stored at 4°C for less than one week. The final protein concentration, as determined by UV adsorption, was of the order of 1 *mg/ml*. These solutions were then further diluted in PB, diluted with purified water containing acetic acid (AA) at pH= 3.5 or mixed with an ethanol (ETOH) - water mixture. The final concentration ranged from 0.001 to 0.1 *mg/ml*. Table 2 summarizes the solutions, final concentration C_f and adsorption times used in our experiments.

The protein was adsorbed on a freshly cleaved mica surface from a droplet of about 100 µl of solution that covered the entire surface area of about 1 cm^2. Adsorption times varied from few seconds up to 30 min during which the surface was kept in an enclosure to prevent solvent evaporation. Adsorption was arrested by dipping the entire sample in a beaker containing pure solvent (without any protein) for solutions (3-8) of Table 2. Samples prepared with PB solution (rows (1-2) and (9)

of Table 2) were dipped in distilled water to avoid the presence of phosphate salt on the surface which would crystallize in air and produce unnecessary topographic features in AFM images. The sample was mounted on a vertical support and dried in air (without using compressed air or nitrogen), letting the excess solvent flow down to the bottom edge of the surface, where it soaked a fiber-free paper towel used in clean-room applications. This procedure can be considered as an alternative to dip-coating useful for small volumes of solution, as it ensured that the solvent-air-solid contact line passes once at each point of the surface.

Exp.#	Gliadin type	Concentration C_f (mg/ml)	Solvent	Adsorption time (min)
1	γ	0.1	H_2O (100%)	1, 2
2	γ	0.05	Acetic Acid	5
3	γ	0.05	H_2O (90%) + ETOH (10%)	5
4	γ	0.05	H_2O (66%) + ETOH (33%)	2, 5, 10, 70
5	γ	0.05	H_2O (50%) + ETOH (50%)	5
6	ω	0.05	H_2O (66%) + ETOH (33%)	0.2, 0.5, 5,15
7	ω	0.001	Phosphate buffer	3

Table 3 Summary of protein solutions and adsorption times used in our experiments. C_f – final concentration, ETOH – ethanol.

Appendix A

Atomic Force Microscopy

The Atomic Force Microscope (AFM) creates a topographic image of the free surface of a sample. In AFM, a sharp tip is microfabricated at the free end of a Si or Si_3N_4 cantilever beam that is fixed at the other end to a rigid support (Fig.44). A laser beam focused on the free end of the cantilever is reflected through a mirror into a position-sensitive, two-quadrant photodetector. The interaction between the tip and the surface bends the cantilever vertically and influences its oscillations. This causes the laser beam to deviate and creates a difference between the intensities measured by each quadrant of the photodiode. The difference quantifies the vertical motion of the tip.

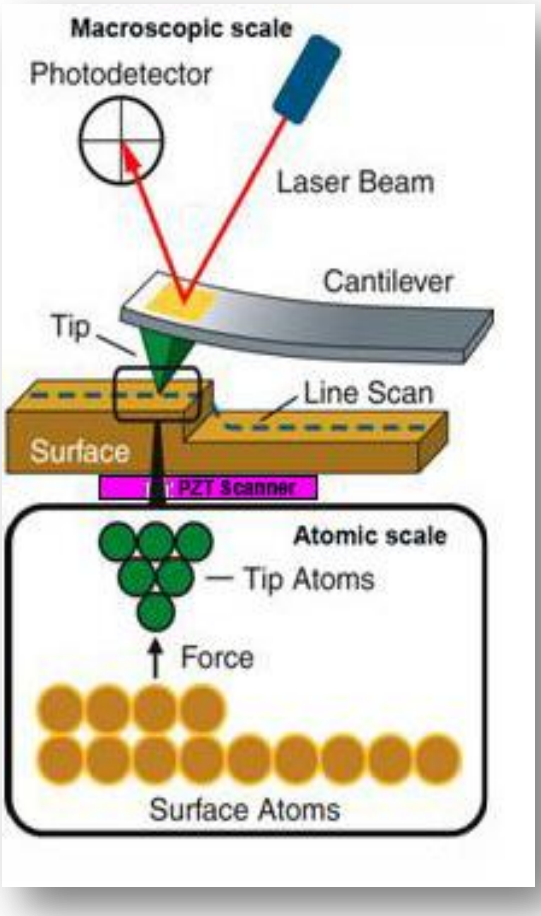

Fig. 44: Principle of atomic force microscopy.

In our study we used the AFM in *tapping mode* configuration. A stiff cantilever is forced to oscillate vertically near its resonance frequency, ν=340 *kHz*, by a

piezoelectric transducer connecting the cantilever fixed end to the AFM tip holder. The amplitude of free oscillations is typically 1-10 nm. Tip-sample interactions (typically Van der Waals, dipole-dipole interaction and electrostatic forces) generally cause the amplitude to decrease as the tip gets closer to the sample. An electronic servo system uses a piezoelectric vertical actuator – the scanner - to control the height of the cantilever above the sample. The servo adjusts the sample height to maintain a set cantilever oscillation amplitude as the tip is scanned over the sample. A tapping image is therefore produced by mapping the vertical displacement *z* of the scanner as a function of the *xy* position of the tip.

Tapping mode AFM was developed as a method to achieve high resolution without inducing destructive contact and frictional forces between the tip and the sample and can be operated both in air and fluid. With the tapping mode technique, one can obtain images of soft and fragile samples such as monolayers of polymers, surfactants or biomolecules as well as single macromolecules. The lateral (in-plane, xy) resolution of AFM images is determined by the curvature radius of the very end of the tip. The sharpest tips available commercially have a radius as small as 5 *nm*. Because the dimension of the interaction region between the tip and the sample is a fraction of the radius, these tips typically provide a lateral resolution of about 1 nm. The vertical (*z*) resolution is usually better than 1 nm and it is given by the position accuracy of the scanner actuator and the precision of the servo system.

AFM images may be affected by various artifacts mostly due to sample tilt, scanner motion and servo system. In our work, image that appeared tilted or bowl-shaped were corrected after recording by subtracting respectively a plane or a paraboloid from the whole image. After this, some images have been further processed by subtracting a different 2^{nd} order polynomial from each line ("flattening" process). The polynomial was calculated so that regions free of features, such as the top of a flat monolayer or uncoated regions of the mica substrate, appeared flat after processing. In all AMF images, dark/bright color indicate low/high topographic features referred to an arbitrary zero height (in black).

Results and discussion

(a) Water and buffer solutions

Figures 45 are representative of all image that we obtained for gliadin adsorbed from water and buffer solutions. Adsorbed proteins are assembled in globules of various sizes covering the substrate at various surface densities depending on the protein type, concentration, adsorption time and dipping-drying procedures. Preliminary attempts to find a correlation among these parameters did not provide a conclusive result: for example, proteins adsorbed from more concentrated solutions and/or for longer times did not always produce a higher surface coverage and/or globule size. Therefore, further experiments are required to elucidate the mechanisms of protein adsorption and aggregation on the surface in water solution.

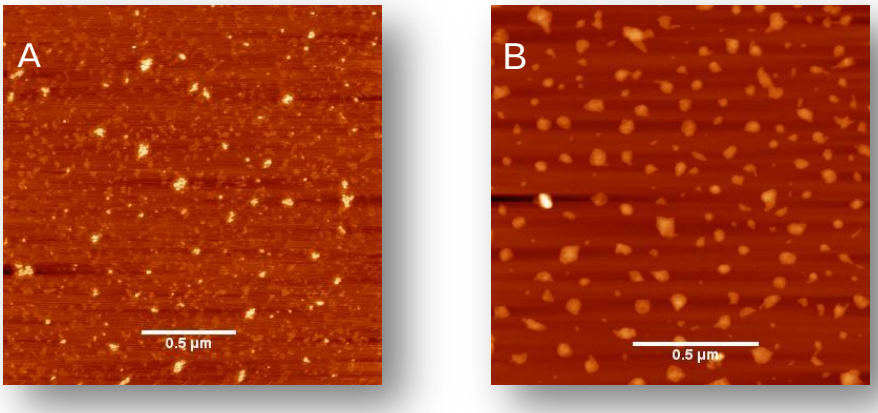

Fig. 45 (A) γ-gliadin adsorbed from purified water solution at concentration C=0.1 mg/ml (Table 2, row 1). (B) ω- gliadin adsorbed from phosphate buffer at C=0.001 mg/ml (Table 2, row 7).

(b) Water/Ethanol solutions

The factor most evidently and reproducibly affecting the adsorption and aggregation of gliadins on mica is the presence of alcohol in the solution. Figure 46 shows γ-gliadins adsorbed from a 1:2 volume mixture of ethanol and water at concentration 0.05 mg/ml and different adsorption times (Table 2, rows 4). After 70 min (Fig. 46B) the protein formed a continuous flat layer with irregular holes of different diameter and depth *h*=3.5-4.5 nm. The contour of the holes was slightly raised of about 1-2 nm with respect to the rest of the layer. Reducing the adsorption times or

changing the ethanol-water ratio (Table 2, rows 4,5) (images not shown) without changing the final concentration of the gliadin solution, the results were similar. When the adsorption time was reduced to 5 min (Fig. 46A), 1:2 ethanol-water solutions produced a discontinuous flat layer of height $h \approx 3.7$ nm covering less than 40% of the surface. Imaged obtained after short adsorption times of 2 min (Fig. 47A) and 5 min (Fig. 47B) showed a certain variability of surface coverage (compare Fig.47B and 47A) that we could not eliminate.

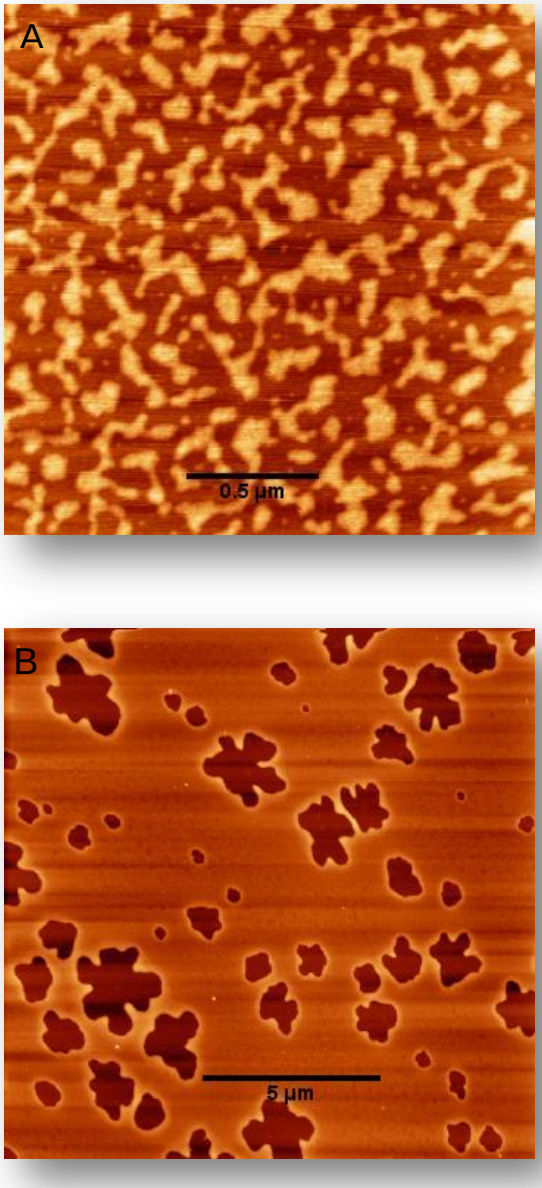

Fig. 46 AFM images of γ–gliadin adsorbed from 1:2 ethanol/water v/v solution for times (A) 5 min and (B) 70 min.

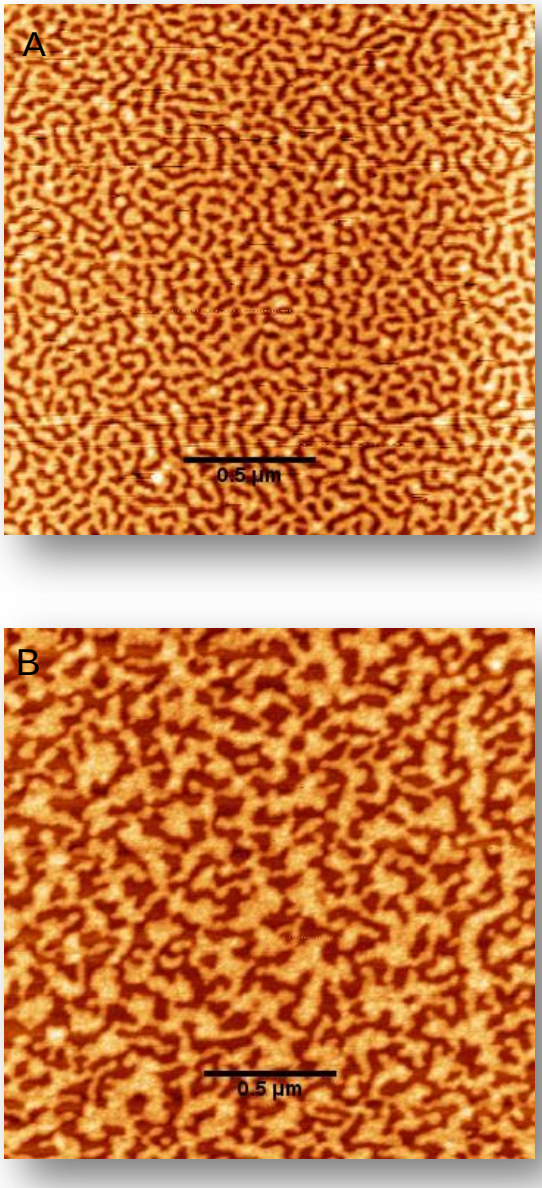

Fig. 47 AFM images of γ–gliadin adsorbed from 1:2 ethanol/water v/v solution for times (A) 2 min and (B) 5 min.

The layers of figures 46 and 47 have a thickness $h<4$ nm which is smaller than the length of a γ–gliadin molecule and comparable to its diameter (Table 1). Therefore, proteins appear to be adsorbed with their longest axis parallel to the substrate or they become flattened after adsorption. Moreover, our results indicate that: (a) protein-surface interaction in water-alcohol mixtures is stronger than in water solution without alcohol, as it produces a higher surface coverage; (b) protein-surface interaction in mixtures is somewhat stronger than protein-protein interactions, or the

latter have an anisotropic character, since adsorption leads to the formation of a layer reflecting the flat geometry of the surface, rather than an amorphous aggregate of proteins; (c) protein-protein interactions, either during or after adsorption, lead to the formation of a continuous layer, rather than a randomly adsorbed layer. Images of Fig.47 are reminiscent of the bilayers formed by amphiphilic surfactants and phospholipids, or the layered structures formed by diblock copolymers by phase separation on a solid surface. However, such systems often show multi-layer structures such as double bilayers with thicknesses multiples of the single thickness, whereas γ-gliadins only show a single thickness – another evidence that protein-protein interaction is weak.

On the contrary, ω–gliadins (Fig.48) adsorbed from an ethanol-water solutions (1:2 volume proportion, Table2, row 6) formed multilayered structures with non-multiple thicknesses. After 10 s of adsorption on mica (Fig. 48A), we observed circular objects with diameter $d \approx 250$ nm and an average height $h \approx 6.5$ nm. The flat background had an RMS roughness of about 0.3 nm. When the adsorption time was increased to 30 sec (Fig. 48B), the aggregates seemed to combine in larger circular objects with a two-layer appearance: a flat circular base with d_1=1 μm and uniform height h_1=1 nm, topped by a circular flat layer with an average diameter d_2= 500 nm and h_2=6 nm with respect to the mica substrate (i.e. wit a thickness h_2-h_1= 5 nm). Notice that the thickness h_1 of the layer in direct contact with the substrate is 6 times smaller than the thickness of the top layer. Moreover, the top layer seemed to grow with the adsorption time at a rate comparable to that of the bottom layer. This is further evidenced in Fig. 48C, where the aggregates formed after 5 min showed a wider bottom layer (h_1=1 nm) but also a wider, thicker and curved top layer. (h_2=7-9 nm). This is again in contrast with surfactant bilayers, where the growth of the top layer in time is delayed and slower than that of the bottom layer. As the aggregates grow to cover most of the mica substrate after an adsorption time of about 15 min, the surface appears as in Fig.48D: an incomplete, discontinuous layer of thickness h=5 nm on top of a complete layer. This structure is similar to that observed in Fig.47B for γ-gliadin, but with a lower surface coverage of about 10%.

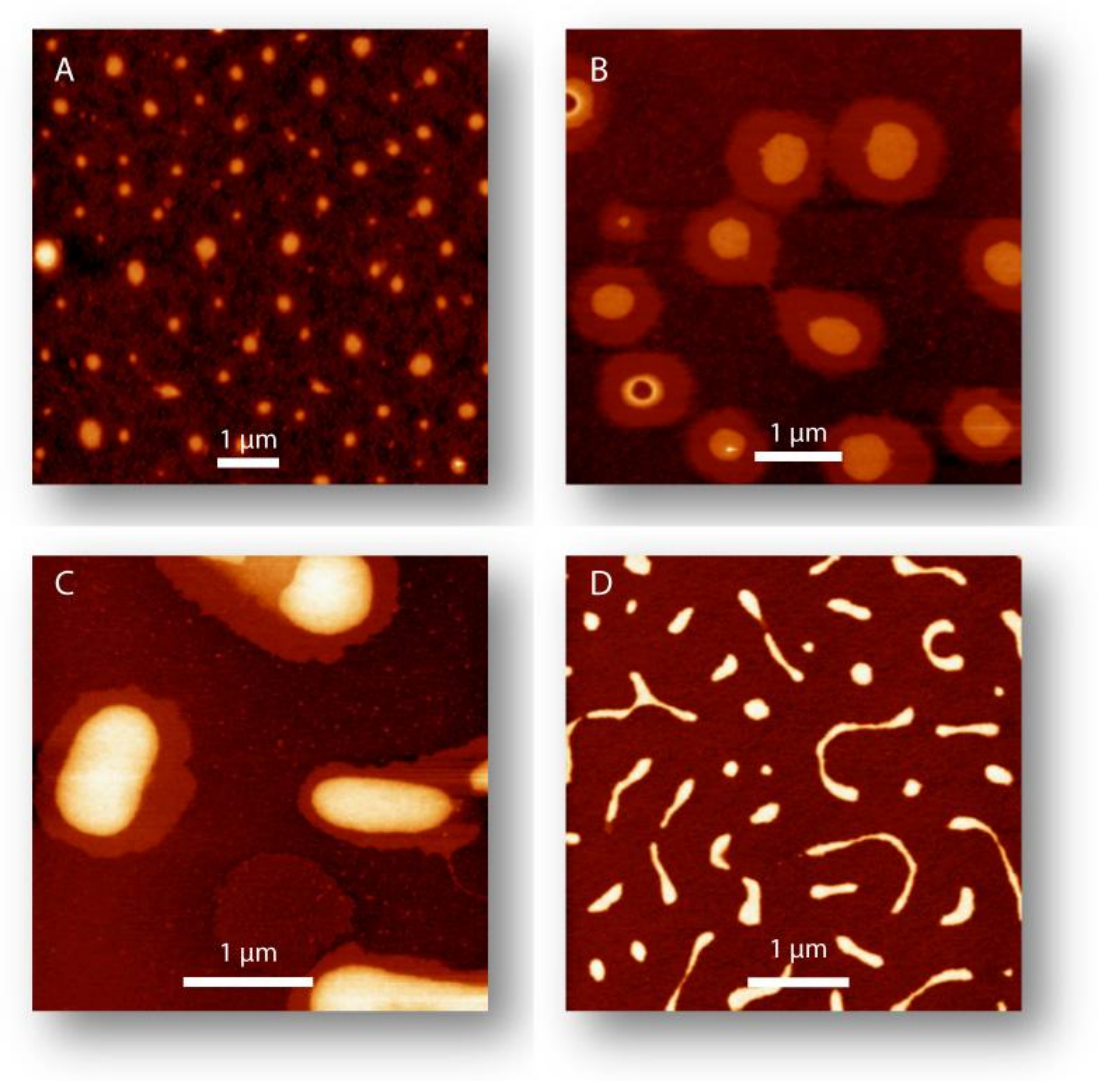

Fig. 48 AFM images of ω–gliadin adsorbed on mica from 1:2 ethanol-water solutions at several adsorption times: (A) 10 sec; (B) 30 sec; (C) 5 min; (D) 15 min.

Protein subunits aggregate at neutral pH whereas acidic pH≈3 favors aggregate disassembly. In fact, our experiments with acetic acid at pH =3.5 (Table 2, row 2) show AFM images with no protein adsorption (images not shown). The absence of adsorption could be explained by the low isoelectric point IEP≈3 of mica, which becomes very weakly charged at ph=3.5, so that electrostatic attraction of the protein is reduced.

Conclusion

Previous studies by dynamic light scattering on gliadins have shown that they form large aggregates in water solution with diameters > 100 nm (Amélie Banc, PhD Thesis, University of Bordeaux, 2007). Our attempt to visualize such aggregates by AFM was unsuccessful, because they did not adhere to the mica surface. We did observe sparse, small globular aggregates, but we could not correlate their size distribution and surface coverage to the relevant experimental parameters to explain the mechanisms of adsorption and aggregation. Nevertheless, our results may have a relevance when compared to the native biological environment of gliadins. In wheat grains, storage proteins interact with and pass through cell membranes made of phospholipids, carbohydrate and glycoprotein, which are generally negatively charged. The lack of significant adsorption of gliadin molecules (and aggregates) on negatively charged mica at neutral and acidic pH indicates that the non-specific part of the gliadin-membrane interaction is repulsive. Adhesion on the cell membrane may still occur via specific interactions (f.e. ligand-receptor interactions).

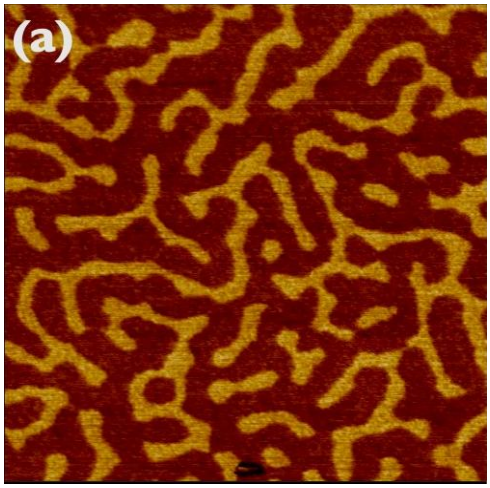

Fig. 49 (a) AFM image of PMMA-PS diblock copolymer on silicon

[adapted from reference http://ragan-group.eng.uci.edu/diblock.html].

The result obtained for water-ethanol solutions, although less relevant to biology, show interesting chemical-physical properties of gliadins that may be relevant to non-food applications as biocompatible molecules. In the presence of ethanol,

which reduces hydrophobic interactions, the protein-protein interaction is reduced. Aggregates are no longer globular as expected for strong isotropic protein-protein interactions, but they have a layered appearance indicating that aggregates are shaped by the anisotropic protein-surface interaction directed along the normal *z* to the surface. More important, the layering propagates along *z* across 2 or 3 layer (at least for ω-gliadins), which is a typical feature of molecules possessing an anisotropy in shape and/or an asymmetric composition such as liquid crystals or surfactants. In fact, images of adsorbed gliadins (Fig. 46 and 47) show interesting morphological analogies with the structures created by microphase separation of adsorbed amphiphilic surfactants and diblock copolymers (Fig.49). We believe that this analogy can be followed to identify the mechanisms underlying the formation of gliadin structures in ethanol solvents. Most likely there is a combination of molecular shape anisotropy, microphase separation, layer self-assembly via hydrophilic-hydrophobic interaction between protein portions having different compositions, and differential solvent evaporation. However, more experimental work is needed to pursue this program.

For the work carried out in this section I acknowledge Prof. R. Bartolino and Dr. B. Zappone.

Appendix B

Multiple Particle Tracking in *Xenopus Laevis* I stage oocytes

The Multiple Particle Tracking (MPT) technique find an important field of application in large cells such as oocytes where, during their growth, several organelles and molecules are displaced in specific territories of the cell instrumental for later embryonic development.

In this experiment measurements are performed in *Xenopus Laevis* I stage oocytes. We have investigated about biophysical mechanisms underlying the mitochondrial cloud (MC) ability to move towards the cortex and asked ourselves whether a relationship can be traced between MC migration and viscoelastic characteristics of the surrounding cytoplasm. The viscoelastic state may depend not only upon cytoskeleton constituents but also upon the presence of other cytoplasm components.

X. Laevis I stage oocytes

Xenopus laevis oogenesis is a continuous process that last about 1 year. It starts with mitosis of oogonia and then proceeds with meiosis of the oocytes. The oocytes develop in the ovary, a transparent sac from where the oocytes protrude in the ovary cavity. Six stages were determined based on the anatomy of the developing oocyte. Stage I oocytes have a diameter of 50-300μm and are transparent. A mitochondria-rich structure, the mitochondrial cloud is asymmetrically located at one side of the nuclear envelope. In the oocyte cytoplasm, microfilaments and microtubules slowly accumulate without apparent order. The cytoskeleton and in particular cytokeratin microfilaments surround and permeate the MC (Carotenuto, 2009).

Stage II oocytes range up to 450 μm in diameter and acquire some opacity. Stages I and II last about six mounts. Accumulation of nutrients (vitellogenesis) and pigment synthesis begins during stage III (the diameter of the oocytes is 450-600 μm). At the end of this stage the cytoskeleton starts a new polarized organization at the vegetal pole. This organization is accomplished in the whole cytoplasm in later stages of oogenesis (stages II-VI), when the pigment granules are gradually segregated in the animal hemisphere. The oocyte acquires the final dimension of about 1.2 *mm*.

Appendix B

Mitochondrial cloud in *X. Laevis*

X. laevis oogonia display a manifest polarity because of the asymmetric localization of both the fusome and the so-called primordial mitochondrial cloud (PMC). The mechanism underlying primary axis determination in *Xenopus* oocytes is strictly bound to this structure, that, in oocyte I, is recognized as mitochondrial cloud (Kloc, 2002) (King, 2005). The definitive MC is rich in active mitochondria (Wilding, 2001) and grows anchored to the nuclear envelope (Heasman, 1984). It contains germplasm mRNAs (Xcat2, Xdaz1, Xpat, DEADSouth, etc ...) and other molecules such as Xlsirts, Xotx1 mRNAs and Xwnt-11, the latter being implicated in the specification of dorso-ventrality (Tao, 2005). Cytokeratin, γ-tubulin and spectrin are as well present in the MC (Carotenuto R., 2000). Some mRNAs are entrapped in the germinal granules located in a endoplasmic reticulum-rich territory called METRO (Kloc, 1996) (Kloc, 1998a) (Chang, 2004). The MC migrates towards the cortex in the early oocyte with an unknown mechanism that directs the MC towards the cortex. At early stage II, the MC releases therein its content, thereby marking the vegetal pole.

In *X.laevis,* an interesting point in the study of MC trip to the vegetal pole is the detection of possible factors interacting with the MC during its migration into the future vegetal pole. As mentioned, during early oogenesis, the oocyte cytoskeleton gradually extends in the cytoplasm, surrounding the MC (Gard, 1999). In studying XNOA 36, a protein associated to the centrosome in mammalian cells (Bolivar, 1999), it was found that the actin–based cytoskeleton network binds specifically the mRNA of XNOA 36 and appears to hold the MC during its migration to the cortex.

Through in situ hybridization and immune staining, it was observed that, in oocytes of about 250 μm, a marked segregation of spectrin and of XNOA 36 mRNA is accomplished in half of the oocyte. Interestingly, the oocytes ability to contract appears later, following oocyte maturation. It was speculated that, in oocytes of late stage I, the asymmetric withdrawal of the cytoskeleton containing XNOA 36 mRNA might supply active force probably needed to drag the MC towards the cortex. However, this hypothesis is related to late stage of MC migration and presently is not supported by experimental data. Many questions can be asked at this point such as:

1) In the oocyte where the MC gradually travels to the cortex, is the sector where the MC migrates characterized by specific viscoelastic properties?

2) Are specific cytoskeleton proteins implicated in the MC anchoring and transport?

3) Does the distribution of such proteins and of their partners significantly vary during the long-lasting stage I of oogenesis?

4) Is the MC itself a signaling center interfering with the surrounding cytoplasm?

That the cytoskeleton might have important role in organelles or molecules anchoring and migration, was proved at later stages of oogenesis (stages II-III) when other mRNAs, such as Vg1 and VegT mRNAs (involved in body plan formation) migrate with a endoplasmic reticulum and microtubule-dependent mechanism, that directs them to the territory where the MC begins to be disaggregated (Yisraeli, 1990). The oocyte acquires a stable polarization at the end of stage III, when the polarized organization of microtubules initiated at the site of Vg1 and VegT migration, spreads in the whole oocyte. Later in oogenesis, a crown of 'radii' composed of microtubules, cytokeratin, spectrin and actin will connect the germinal vesicle to the cortex.

Sample and Instrumentation

A DIC microscope (*Leica* DM 5500B) supplied by a 100X oil immersion microscope objective and a charge-coupled-device (CCD) camera (Hamamatsu C5985) have been employed in the MPT setup. For this investigation, only premature I stage oocytes have been utilized. These cells are putted inside the same chamber used for starfish oocytes acquisition. Oocytes are maintained in a FS Ringer (100mM NaCl, 1mM MgCl2 , 1.8mM KCl, 2mM CaCl2 , 5mM HEPES pH 6.5) during measurements. The Brownian motion of endogenous granules with a diameter of about 400 *nm* has been recorded at a frame rate of 25 *fps* in movies of 20 *s*.

During acquisition of Brownian trajectories, we checked that oocytes were immobile. Endogenous particles within oocyte cytoplasm have been excellent probes because they were greater than the mesh-size of the cytoskeleton network (several tens of nano-meter, (Koster, 2009)) to satisfy the approximation of conti-

nuum medium in the Stoke-Einstein equation and also well contrasted with respect to the background, Fig.50. All measurements in the present experiment have made at room temperature (about 21°C).

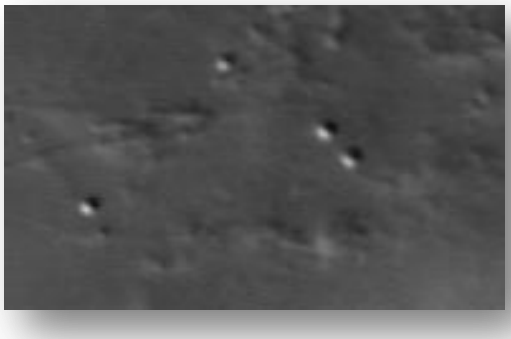

Fig. 50 Endogenous granules in oocytes cytoplasm.

Results

Multiple Particle Tracking technique has been applied in order to understand if the MC migration is governed by a viscoelastic change in the region where it moves.

Several trajectories are recorded for each oocyte and the MSD is calculated from each trajectory. About 50 oocytes have been analyzed. Figure 51 shows MSDs of only 150 trajectories collected from about 5 examined oocytes, while Fig.52 shows the ensemble average MSD over all oocytes. As can be seen, measurements display a large fluctuation, which is typical for heterogeneous media like cell cytoplasm.

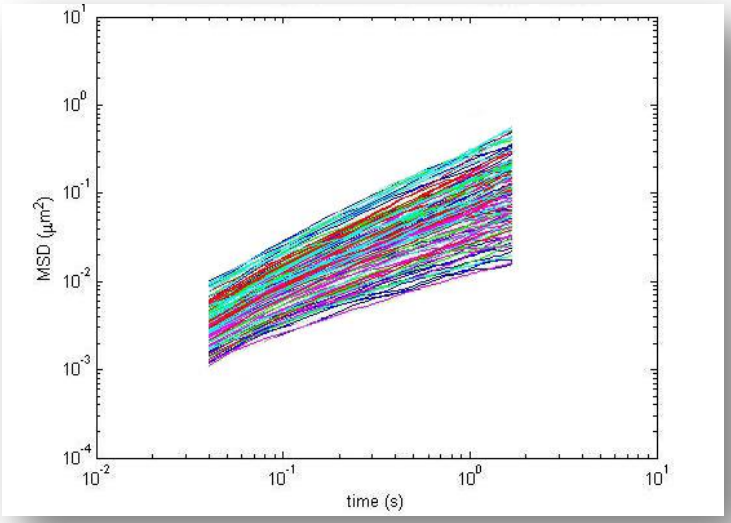

Fig. 51 MSDs of 150 trajectories from 5 analyzed oocytes.

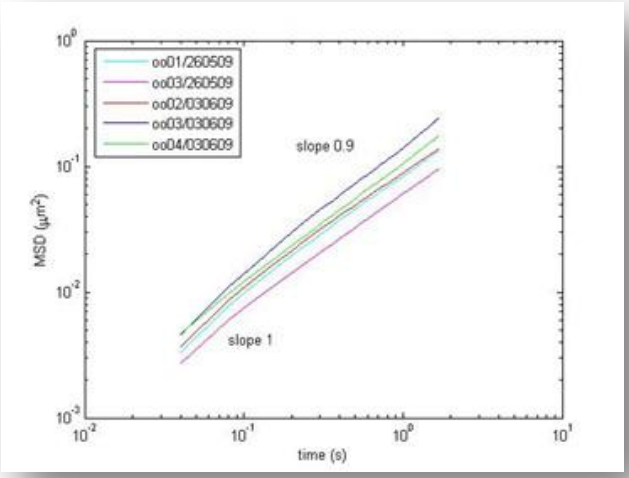

Fig. 52 Ensemble average MSD for 5 analyzed oocytes.

All curves of Fig.52 follow approximately the same viscoelastic trend: at short times trajectories freely diffuse (slope 1); at long times they begin sub-diffusion (slope 0.9). Evidently, as is typical for biological materials, oocytes are heterogeneous systems in which viscoelastic properties change locally even if in this case the

cytoplasm seems to be a predominantly viscous character both at short and long times.

The mitochondrial cloud starts to migrate from the nucleus to the cortex privileging a precise direction called ‘section 1’, as shown in Fig.53. MPT investigation has done in section 1 and in the opposite region, ‘section 2’, to understand if there were differences in the viscoelastic response of the two sections. A lower viscosity in section 1 with respect to section 2, for example, could be responsible of the motion in that direction because of the less fluid resistance.

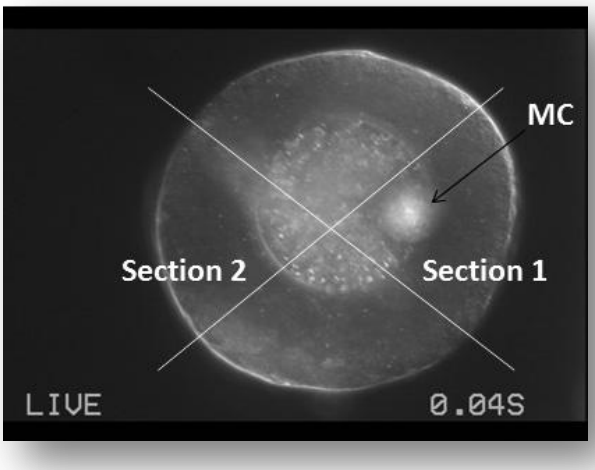

Fig. 53 X. Laevis oocyte divided in ‘section 1’ and ‘section 2’ for viscoelastic investigation; MC is the mitochondrial cloud.

In Fig.54 are represented the ensemble average of the MSDs obtained from the Brownian motion of endogenous grains presents in both cytoplasm sections of several oocytes. Magenta MSDs are related to granules present is the cytoplasm region where the MC migrates, section 1, while blue MSDs are related to granules present in section 2.

Appendix B

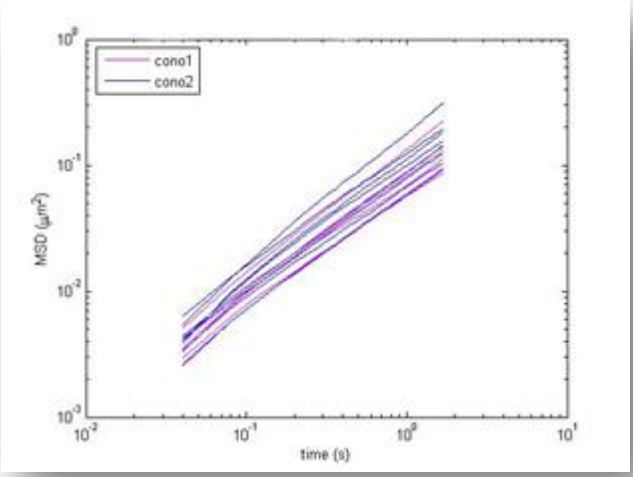

Fig. 54 Ensemble average MSDs in 'section 1' (magenta) and 'section 2' (blue) for several oocytes.

Differently from expectations, the viscoelastic behaviour of the cytoplasm region where the MC migrates is almost the same of that in section 2. All endogenous granules mainly show a viscous behaviour, for this purpose viscosity, η, has easily calculated for both cytoplasm section 1 and section 2. Viscosity values, obtained from the diffusion coefficients using the Stokes-Einstein formula $D=k_BT/6\pi\eta a$, range between $0.02 - 0.06\ Pa \cdot s$. In conclusion, the displacement of the mitochondrial cloud seems to be independent of the viscosity of the region it goes through.

For the work carried out in this section I acknowledge Dr. R. Carotenuto, Dr. M. Salemme and Leica for DIC microscope borrowing.

Bibliography

http://u759.curie.u-psud.fr/softwaresu759.html [Online]. - 17. TOMOJ Plugin, Institute national de la santé et de la recherce médicale, U759, France,.

Abkarian M. , M. Faivre, and A. Viallat Swinging of red blood cells under shear flow [Rivista]. - [s.l.] : Phys. Rev. Lett., 2007. - 188302 : Vol. 98.

Addas K.M., C.F. Schmidt, and J.X. Tang Microrheology of solutions of semiflexible biopolymer filaments using laser tweezers interferometry [Rivista]. - [s.l.] : Phys. Rev. E, 2004. - 021503 : Vol. 70.

A-Hassan E., W. F. Heinz, M. D. Antonik, N. P. D'Costa, S. Nageswaran,C. A. Schoenenberger, and J. H. Hoh. Relative microelastic [Rivista]. - [s.l.] : Biophys. J. , 1998. - 1564-1578 : Vol. 74.

Amblard F., B. Yurke, A. Pargellis and S. Leibler A magnetic manipuletor for studying local rheology and micromechanical properties of biological system [Rivista]. - [s.l.] : Rev. Sci. Instr., 1996. - 818-827 : Vol. 87.

Apgar J., Y. Tseng, E. Fedorov, M.B. Herwig, S.C. Almo, and D. Wirtz Multiple particle tracking of heterogeneities in solutions of actin filaments and actin bundles [Rivista]. - [s.l.] : Biophys. J., 2000. - 1095-1106 : Vol. 79.

Ashkin A. [Rivista]. - [s.l.] : Biophys. J., 1992. - 569-582 : Vol. 61.

Ashkin A. Acceleration and Trapping of Particles by Radiation Pressure [Rivista]. - [s.l.] : Phys. Rev. Lett., 1970. - 156-159 : Vol. 24.

Ashkin A., J. M. Dziedzic, J. E. Bjorkholm, and Steven Chu Observation of a single-beam gradient force optical trap for dielectric particles [Rivista]. - [s.l.] : Optics Letters, 1986. - 288-290 : Vol. 11 issue 5.

Askin A. [Rivista]. - [s.l.] : Biophys. J., 1992. - 569-582 : Vol. 61.

Bambardekar K., A. K. Dharmadhikari, J. A. Dharmadhikari, D. Mathur, and S. Sharma Measuring erythrocyte deformability with fluorescence, fluid forces, and optical trapping [Rivista]. - [s.l.] : J. Biomed. Opt., 2008. - 064021 : Vol. 13.

Bibliography

Banc A., † Bernard Desbat,‡ Denis Renard,§ Yves Popineau,§ Ce´cile Mangavel,§ and Laurence Navailles*,† Structure and Orientation Changes of ö- and ç-Gliadins at the Air-Water Interface: A PM-IRRAS Spectroscopy and Brewster Angle Microscopy Study [Rivista]. - [s.l.] : Langmuir, 2007. - 13066-13075 : Vol. 23.

Banc Amelie, Bernard Desbat, Denis Renard, Yves Popineau, Ccile Mangavel, and Laurence Navailles Structure and Orientation Changes of - and -Gliadins at the Air−Water [Rivista]. - [s.l.] : Langmuir, 2007. - 13066-13075 : Vol. 23(26).

Bausch A. R., F. Ziemann, A. A. Boulbitch, K. Jacobson, and E. Sackmann. Local measurements of viscoelastic parameters of adherent [Rivista]. - [s.l.] : Biophys. J., 1998. - 2038-2049 : Vol. 75.

Bausch A. R., W. Moller, and E. Sackmann. Measurement of local [Rivista]. - [s.l.] : Biophys. J. , 1999. - 573-579 : Vol. 76.

Bausch A.R., W. Moller, and E. Sackmann Measurements of local viscoelasticity and forces in living cells by magnetic tweezers [Rivista]. - [s.l.] : Biophys. J. , 1999. - 573-579 : Vol. 76.

Binnig G., Quate C. F. e Gerber C. Nanomechnaical force measurements of gliadin protein interaction [Rivista]. - [s.l.] : Phys. Rev. Lett., 1986. - 930–933 : Vol. 56.

Bird R. B., R. C. Armstrong, and O. Hassager, Dynamics of Polymeric Liquids [Rivista]. - [s.l.] : John Wiley and sons, New York, 1987.

Block S.M. A Laboratory Manual [Sezione di libro] // Cell Biology. - [s.l.] : Cold Spring Harbor Press, 1998. - Vol. chapter Constructing optical tweezers.

Bolivar J., Diaz I., Iglesias C., and Valdivia M. Molecular Cloning of a Zinc Finger Autoantigen Transiently Associated with Interphase Nucleolus and Mitotic Centromeres and Midbodies [Rivista]. - [s.l.] : J. Biol. Chem., 1999. - 36456-36464 : Vol. 274.

Braga P.C., Ricci D. Atomic force microscopy: biomedical methods and applications [Rivista]. - [s.l.] : Totowa, N.J.: Humana Press., 2004.

Bibliography

Bray D., and C. Thomas The actin content of fibroblasts [Rivista]. - [s.l.] : Biochem. J., 1975. - 221-228 : Vol. 147.

Breuer S. Micorscale diagnostic technique [Libro]. - [s.l.] : Springer.

Capitanio M., R. Cicchi, and F.S. Pavone Position control and optical manipulation for nanotechnology applications [Rivista]. - [s.l.] : Eur. Phys. J.B, 2005. - 1-8 : Vol. 46.

Carotenuto R. Vaccaro M.C., Capriglione t., Petrucci T. C., and Campanella C. Alfa- spectrin has a stage-specific asymmetrical localisation during Xenopus oogenesis [Rivista]. - [s.l.] : Mol.Rep. and Dev., 2000. - 229-239 : Vol. 55.

Carotenuto R., Petrucci T.C., Correas I., Vaccaro M.C., De Marco N., Dale B., Wilding M. Protein 4.1 and its interaction with other cytoskeletal proteins in Xenopus laevis oogenesis [Rivista]. - [s.l.] : European Journal of Cell Biology, 2009. - 343-356 : Vol. 88.

Cauvain S.P., L.S. Young. Technology of breadmaking [Libro]. - [s.l.] : Springer 2007.

Chae B.S., and E.M. Furst Probe surface chemistry dependence and local polymer network structu in F-actin micorheology [Rivista]. - [s.l.] : Langmiur, 2008. - 3084-3089 : Vol. 21 (7).

Chang P., Torres J., Lewis R.A., Mowry K.L., Houliston E., and King M. L. Localization of RNAs to the Mitochondrial Cloud in Xenopus laevis oocytes through Entrapment and Association with Endoplasmic Reticulum [Rivista]. - [s.l.] : Mol. Biol., 2004. - 4669-4681 : Vol. 15.

Cheezum M.K., W.F.Walker, and W.H. Guilford Quantitative comparison of algorithms for tracking single fluorescent particles [Rivista]. - [s.l.] : Biophys. J., 2001. - 2378-2388 : Vol. 81.

Chou Y.H., O. Skalli, and R.D. Goldman Intermediate filaments and cytoplasmic network: new connections and more functions [Rivista]. - [s.l.] : Curr. Opin. Cell Biol., 1997. - 49-53 : Vol. 9.

Bibliography

Citters K.M.V., B.D. Hoffman, G. Massiera, J.C. Crocker The role of F-actin and myosin in epithelial cell rheology [Rivista]. - [s.l.] : Biophys. J., 2006. - 3946-56 : Vol. 91.

Cojoc D. , E. Di Fabrizio, L. Businaro, S. Cabrini, F. Romanato, L. Vaccari, and M. Altissimo. Design and fabrication of diffractive optical elements for optical tweezers arrays by means of e-beam lithography. [Rivista]. - [s.l.] : Microelectr. Eng., 2002. - 963-969 : Vol. 61-62.

Cojoc D., E. Di Fabrizio, L. Businaro, F. Romanato, S. Cabrini,L. Vaccari Phase diffractive elements for three dimensional spot arrays generation [Rivista]. - 2001.

Cojoc D., E. Ferrari, V. Garbin, and E. Di Fabrizio Multiple optical tweezers for micro Raman spectroscopy [Rivista]. - [s.l.] : Proc. Soc. Photo. Opt. Instrum. Eng., 2005. - 64-75 : Vol. 5930.

Cojoc D., Emiliani, V., Ferrari, E., Malureanu, R., Cabrini, S., Proietti, R. Z. and Di Fabrizio E. Multiple optical trapping by means of diffractive optical elements. [Rivista]. - [s.l.] : Japanese Journal of Applied Physics, 2004. - 3910-3915 : Vol. 43 (6B).

Cojoc D., Garbin, V., Ferrari, E., Businaro, L., Romanato, F. and Di Fabrizio, E. Laser trapping and micro-manipulation using optical vortices. [Rivista]. - [s.l.] : Microelectronic Engineering, 2005. - 125-131 : Vol. 78-79.

Cojoc D., V. Emiliani, E. Ferrari, R. Malureanu, S. Cabrini, R.Z. Proietti, and E. Di Fabrizio. Multiple optical trapping by means of diffractive optical elements. [Rivista]. - [s.l.] : Japan J. Appl. Phys., 2004. - 3910–3915 : Vol. 43.

Cojoc D., V. Emiliani, E. Ferrari, V. Garbin, E. Di Fabrizio Dynamic multiple beads manipulation on x-y-z directions [Rivista]. - [s.l.] : SPIE, 2004 (2). - 126-136 : Vol. 5514.

Crick F. H. C., and A. F. W. Hughes. The physical properties of [Rivista]. - [s.l.] : Exp. Cell, 1950. - 37-80 : Vol. 1.

Crocker J.C., and B.D. Hoffman Multiple particle tracking and two-point microrheology [Rivista]. - [s.l.] : Methods in Cell Biol., 2007. - 141-178 : Vol. 83.

Bibliography

Crocker J.C., and D.G. Grier Methods of digital video microscopy for colloidal studies [Rivista]. - [s.l.] : J. Coll. Inter. Sci., 1996. - 298-310 : Vol. 179.

Crocker J.C., M.T. Valentine, E.R. Weeks, T. Gisler, P.D. Kaplan, Y.G. Yodh, D.A. Weitz Two point microrheology of inhomogeneous soft materials [Rivista]. - [s.l.] : Phys. Rev. Lett., 2000. - 888-891 : Vol. 85.

Crocker J:C: [Rivista].

Curtis J E, Koss B A and Grier D G Dynamic holographic optical tweezers [Rivista]. - [s.l.] : Opt. Commun., 2002. - 69-175 : Vol. 207 .

Curtis J.E. , B.A. Koss, and D.G. Grier. Dynamic holographic optical tweezers [Rivista]. - [s.l.] : Opt. Commun., 2002. - 169-175 : Vol. 297.

Daily B., E. L. Elson, and G.I. Zahalank Cell poking: determination of the elastic area compressibility modulus of the erytrocyte membrane [Rivista]. - [s.l.] : Biophys. J., 1984. - 661-682 : Vol. 45.

Daniels B.R., B.C. Masi, D. Wirtz Probing single cell micromechnaics in vivo: the microrheology oc C.Elegans developing embryos [Rivista]. - [s.l.] : Biophys. J., 2006. - 4712-4719 : Vol. 90.

Dasgupta B. R., S.-Y. Tee, J. C. Crocker, B. J. Frisken, and D. A. Weitz [Rivista]. - [s.l.] : Phys. Rev. E, 2002. - 051505 : Vol. 65.

Dholakia K. , and P. Reece Optical manipulation takes hold [Rivista]. - [s.l.] : Nano Today, 2006. - 18-27 : Vol. 1.

Doi M.S.F and Edwards The theory of polymer dynamics [Rivista]. - [s.l.] : Clarendon Press, Oxford, 1994.

Dufresne E R and Grier D G Optical tweezer arrays and optical substrates created with diffractive optical elements [Rivista]. - [s.l.] : Rev. Sci. Instrum., 1998. - 1974-1977 : Vol. 69 .

Dufresne E R, Spalding G C, Dearing M T, Sheets S A and Grier D G Computer generated holographic optical tweezer arrays [Rivista]. - [s.l.] : Rev. Sci. Instrum., 2001. - 1810-1816 : Vol. 72 .

Dufresne E.R., G.C. Spalding, M.T. Dearing, S.A. Sheets, and D.G. Grier. Computer-generated holographic optical tweezer arrays. [Rivista]. - [s.l.] : Rev. Sci. Inst., 2001. - 1810-1816 : Vol. 78.

Eichinger L., B. Koppel, A. A. Noegel, M. Schleicher, M. Schliwa, K. Mechanical perturbation [Rivista]. - [s.l.] : Biophys. J. , 1996. - 1054-1060 : Vol. 70.

Einstain A. Investiagtion on the theroy of Brownian movements [Rivista]. - [s.l.] : R. Furth editor. Dover, New York, 1956.

Emiliani V., Cojoc, D., Ferrari, E., Garbin, V., Durieux, C., Coppey-Moisan, M. and Di Fabrizio, E. Wave front engineering for microscopy of living cells. [Rivista]. - [s.l.] : Optics Express, 2005. - 1395-1405 : Vol. 13.

Emiliani V., D. Cojoc, E. Ferrari, V. Garbin, C. Durieux, M. Coppey- Wave front engineering for microscopy of living cells. [Rivista]. - [s.l.] : Opt. Exp., 2005. - 1395-1405 : Vol. 13.

Fabry B., G.N. Maksym, J.P. Butler, M. Glogauer, D. Navajas, and J.J. Fredberg Scaling the microrheology of living cells [Rivista]. - [s.l.] : Phys. Rev. Lett., 2001. - 1481021 : Vol. 87.

Fallman E. ,and O. Axner. Design for fully steerable dual-trap optical tweezers. [Rivista]. - [s.l.] : Applied oPTICS, 1997. - 21072113 : Vol. 36.

Fauver M. , E. J. Seibel, J. R. Rahn, M. G. Meyer, F. W. Patten, T. Neumann, and A. C. Nelson Three-dimensional imaging of single isolated cell nuclei using optical projection tomography [Rivista]. - [s.l.] : Opt. Express, 2005. - 4210-4223 : Vol. 13.

Felder S., and E. L. Elson Mechanics of fibroblast locomotion: [Rivista]. - [s.l.] : J. Cell Biol., 1990. - 2513–2526 : Vol. 111.

Ferrari E., Emiliani, V., Cojoc, D., Garbin, V., Zahid, M., Durieux, C., Coppey-Moisan, M.and Di Fabrizio E. Biological samples micro-manipulation by means of

optical tweezers. [Rivista]. - [s.l.] : Microelectronic Engineering, 2005. - 575-581 : Vol. 78-79.

Garbin V., Cojoc, D., Ferrari, E., Di Fabrizio, E., Overvelde, M., van der Meer, S. M., de Jong, N., Lohse, D. and Versluis, M. Combined optical micromanipulation and high speed imaging reveals changes in microbubble dynamics near a boundary. [Rivista]. - [s.l.] : Applied Physics Letters, 2007.

Garbin V., Cojoc, D., Ferrari, E., Proietti, R. Z., Cabrini, S. and Di Fabrizio, E. Optical micro-manipulation using Laguerre-Gaussian beams. [Rivista]. - [s.l.] : Japanese Journal of Applied Physics, 2005. - 5773-5776 : Vol. 44 (7B).

Gard D.L. Confocal Microscopy and 3-D Reconstruction of the cytoskeleton of Xenopus oocyte [Rivista]. - [s.l.] : Microscopy Research and Technique, 1999. - 388-414 : Vol. 44.

Guigas G., C. Kalla, M. Weiss Probing the nanoscale viscoelasticity of intracellular fluids in living cells [Rivista]. - [s.l.] : Biophys. J., 2007. - 316-323 : Vol. 93.

Heasman J., Quarmby, J., and Wylie, C.C. The mitochondrial cloud of Xenopus oocytes: The source of germinal granule material [Rivista]. - [s.l.] : Dev. Biol. , 1984. - 458-469 : Vol. 105.

Heil-Chapdelaine R.A., J.O. Joann Characterization of changes in F-actin during maturation of starfish oocytes [Rivista]. - [s.l.] : Develop. Biolog., 1996. - 204-216 : Vol. 177.

Hiller G., and K. Weber Radioimmunoassay for tubulin: a quantitative comparison of the tubulin content of different established tissue culture cells and tissues [Rivista]. - [s.l.] : Cell, 1978. - 795-804 : Vol. 14.

Hiramoto §Y. Mechanical properties of the protoplasm of the sea urchin egg. I Unfertilized egg, II Fertilized egg [Rivista]. - [s.l.] : Exp. Cell Res., 1969. - 201-218 : Vol. 56.

Hiramoto Y., Mechanical properties of starfish oocytes [Rivista]. - [s.l.] : Dev. Growth Differ., 1976. - 205-209 : Vol. 18.

Bibliography

Hochmuth R. M. Measuring the mechanical properties of individual human blood cells [Rivista]. - [s.l.] : J. Biomech. Eng., 1993. - 515-519 : Vol. 115.

Hoffman B. D., G. Massiera, K.M.V. Citters, J.C. Crocker The consensus mechanics of ultured mammalian cells [Rivista]. - [s.l.] : Proc. Natl. Acad. Sci USA , 2006. - 10259-64 : Vol. 103.

Hongshun Y., Yifen W., Shaojuan L., HongjieA.Yunfei L.Fusheng C. Application of Atomic Force Microscopy as a Nanotechnology Tool in Food Science [Rivista]. - [s.l.] : JOURNAL OF FOOD SCIENCE, 2007. - 4 : Vol. 72.

Jiang G.Y., A.H.Huang, Y.F. Cai, M. Tanase, M.P. Sheetz Rigidity sensing at the leading edge through integrins and RPTP [Rivista]. - [s.l.] : Biophys. J., 2006. - 1804-1809 : Vol. 90.

Jones R. W., Taylor, N. W. and Senti, F. R. Electrophoresis and Fractionation of Wheat Gluten [Rivista]. - [s.l.] : Archives of Biochemistry and Biophysics, 1959. - 363-376 : Vol. 84.

K. C. Neumann and S. M. Block Optical trapping [Rivista]. - [s.l.] : Rev. Sci. Instrum. , 2004. - 2787-2809 : Vol. 75.

K. Castelino S. Satyanarayana, and M. Sitti Manufacturing of two and three-dimensional micro/nanostructures by integrating optical tweezers with chemical assembly [Rivista]. - [s.l.] : Robotica, 2005. - 435-439 : Vol. 23.

Karen E.K., A.C. Rowat, J. Liu, T.E. Angelini, C.P. Brangwynne, G.H. Koenderink and D. Weitz The cell as material [Rivista]. - [s.l.] : Curr. Opin. in Cell Biol., 2007. - 101-107 : Vol. 19.

Kasza K.E.,A.C.Rowat, J. Liu, T.E. Angelini, C.P. Brangwynne, G.H. Koenderink, D.A. Weitz The cell as material [Rivista]. - [s.l.] : Curr. Opin. Cell Biol., 2008. - 101-107 : Vol. 19.

King M. L., Messit T. J., Mowry K. L. Putting RNAs in the right place at the right time: RNA localisation in the frog oocyte [Rivista]. - [s.l.] : Bio-Cell, 2005. - 19-33 : Vol. 97.

Bibliography

Kloc M., Larabell C. and Etkin, L.D. Elaboration of the Messeger Transport Organizer pathway for localisation of RNA to the vegetal cortex of Xenopus oocytes [Rivista]. - [s.l.] : Dev. Biol., 1996. - 119-133 : Vol. 180.

Kloc M., Larabell C., Chan A.P. and Etkin, L.D. Contribution of METRO pathway localized molecules to the organisation of germ cell lineage [Rivista]. - [s.l.] : Mech. Dev., 1998a. - 81-93 : Vol. 75.

Kloc M., Zearfoss N.R., Etkin L.D. Mechanisms of subcellular mRNA localization [Rivista]. - [s.l.] : Cell, 2002. - 533-544 : Vol. 108.

Kole T.P., T. Tseng, I. Jiang, J.L. Katz, and D. Wirtz Intracellular mechanics of migrating fibroblasts [Rivista]. - [s.l.] : Molecular biology of the cell, 2005. - 328-338 : Vol. 16.

Kole T.P., T. Tseng, L. Huang, J.L. Katz, and D. Wirtz Rho kinase regulates the intracellular micromechanical response of adherent cells to rho activation [Rivista]. - [s.l.] : Molecular biology of the cell, 2004. - 3475-3484 : Vol. 15.

Koster S. and Thomas Pfohl An In Vitro Model System forcytoskeletal confinement [Sezione di libro]. - [s.l.] : Cell Motility and the Cytoskeleton, 2009.

Kuo S. C., and M. P. Sheetz. Optical tweezers in cell biology. [Rivista]. - [s.l.] : Trends Cell Biol, 1992. - 116-118 : Vol. 2.

Kyozuka K., J.T. Chun, A. Puppo, G. Gragnaniello, E. Garante, L. Santella Actin cytoskeleton modulates calcium signaling during maturation of starfish oocytes [Rivista]. - [s.l.] : Dev. Biol., 2008. - 426-35 : Vol. 320.

Lai S.K., D.E. O'Hanlon, S. Harrold, S.T. Man, Y.Y. Wang, R. Cone, and J. Hanes Rapid trANSPORT OF LARGE POLYMERIC NANOPARTICLES IN FRESH UNDILUITED HUMAN MUCUS [Rivista]. - [s.l.] : PNAS, 2007. - 5 : Vol. 104.

Larson The Structure and Rheology of Complex Fluids [Rivista]. - [s.l.] : Oxford University Press, 1999.

Bibliography

Leach J. , G. Sinclair, P. Jordan, J. Courtial, and M.J. Padgett. 3d manipulation of particles into crystal structures using holographic optical tweezers. [Rivista]. - [s.l.] : Opt. Expr., 2004. - 220-226 : Vol. 12.

Levine A.J. and T.C. Lubensky [Rivista]. - [s.l.] : Phys. Rev. E, 2001. - 041510 : Vol. 63.

Liesener J., M. Reicherter, T. Haist, and H.J. Tiziani. Multi-functional optical tweezers using computer-generated holograms. [Rivista]. - [s.l.] : Opt. Commun., 2000. - 77-82 : Vol. 185.

Limpert E. W.A. Stahel, and M. Abbt Log-normal distributions across the scinces: keys and clues [Rivista]. - [s.l.] : BioScience, 2001. - 341-352 : Vol. Vol. 51 No. 5..

Luby-Phelps K. Cytoarchiteture and physical properties of cytoplasm: volume, viscosity, diffusion, intracellular surface area [Rivista]. - [s.l.] : Inter. Rew. of Cyt., 2000. - 189-221 : Vol. 192.

Luby-Phelps K., D.L. Taylor, and F. Lanni Probing the structure of cytoplasm [Rivista]. - [s.l.] : The Journal of cell biology, 1986. - 2015-2022 : Vol. 102.

MacKintosch F.C., and C.F. Schmidt Microrheology [Rivista]. - [s.l.] : Curr. Opin. Colloid Interface Sci., 1999. - 300-307 : Vol. 4.

MacKintosh F.C., and C.F. Schmidt Microrheology [Rivista]. - [s.l.] : Curr. Opin. Colloid Interface Sci., 1999. - 300-307 : Vol. 4.

Martin W. M. Electro kinetic Properties of Proteins. I. Isoelectric Point and Solubility of Wheat Proteins in Aqueous Solutions of Ethanol [Rivista]. - 1931 : Journal of Physical Chemistry. - 2065-90 : Vol. 35.

Mason T.G., and D.A. Weitz Optical measurements of frequency-dependent linear viscoleastic moduli of complex fluids [Rivista]. - [s.l.] : Phys. Rev. Lett., 1995. - 1250-1253 : Vol. 74.

Mason T.G., H. Gang, and D.A. Weitz Diffusing wave spectroscopy measurements of viscoleasticity of complex fluids [Rivista]. - [s.l.] : Opt. Soc. Am. A, 1997b. - 139-149 : Vol. 14.

Bibliography

Mason T.G., K. Ganesan, J. van Zanten, D. Wirtz, S.C. Kuo Particle tracking microrheology of complex fluids [Rivista]. - [s.l.] : Phys. Rev. Lett., 1997a. - 3282-3285 : Vol. 79.

McGrath J.L., J.H. Hartwig, and S.C. Kuo The mechanics of F-actin microenvironments depend on chemistry of probing surfaces [Rivista]. - [s.l.] : Biophys. J., 2000. - 3258-3266 : Vol. 79.

McGrath J.L., J.H.Hartwig, adn S.C. Kuo [Rivista]. - [s.l.] : Biophys. J., 2000. - 3258-3266 : Vol. 79.

McMaster T.J., M.J. Miles, D.D. Kasardat, P.R. Shewry, A.S. Tatham. Atomic Force microscopy of a-gliadin fibrils and in situ degradation [Rivista]. - [s.l.] : Journal of Cereal Science, 1999. - 281-286 : Vol. 31.

Moradi A. R., E. Ferrari, V. Garbin, E. Di Fabrizio, and D. Cojoc Strength control in multiple optical traps generated by means of diffractive optical elements [Rivista]. - [s.l.] : Opt. Adv. Mat.-Rapid Comm., 2007. - 158-161 : Vol. 1.

Moradi A., E. FERRARI, V. GARBIN, E. DI FABRIZIO, D. COJOC Strength control in multiple optical traps generated by means of diffractive optical elements [Rivista]. - [s.l.] : OPTOELECTRONICS AND ADVANCED MATERIALS, 2007. - 158-161 : Vol. 1, #4.

Moradi A.-R., Ferrari, E., Garbin, V., Di Fabrizio, E. and Cojoc, D. Strength control in multiple optical traps generated by means of diffractive optical elements. [Rivista]. - [s.l.] : Journal of Optoelectronics and Advanced Materials, 2007.

Morris V.J., Kirby A.R., Gunning A.P. Atomicforcemicroscopy for biologists [Libro]. - [s.l.] : London: Imperial College Press., 1999.

Nicklas R. B. Measurements of the force produced by the mitotic [Rivista]. - [s.l.] : J. Cell Biol. , 1983. - 542-548 : Vol. 97.

Paananen A. , K. Tappura, A. S. Tatham, R. Fido, P. R. Shewry, M. Miles, T. J. McMaster Nanomechanical Force measurements on gliadin protein interaction [Rivista]. - [s.l.] : Wiley InterScience, 2006. - Vol. DOI 10.1002/bip.20603.

Palmer A., J. Xu, and D. Wirtz High-frequency viscoleasticity of crosslinked actin filament networks measured by diffusing wave spectroscopy [Rivista]. - [s.l.] : Rheologica Acta., 1998. - 97-106 : Vol. 37.

Panorchan P., J.S.H. Lee, B.R. Daniels, T.P. Kole, Y. Tseng, D. Denis Wirtz Probing cellular mechanical responses to stimuli using ballistic intracellular nanorheology in cell mechanics [Rivista]. - [s.l.] : Meth. Cell Biol., 2003. - 115-140 : Vol. 83.

Peterman E.J.G., M.A.V. Dijk, L.C. Kapitein and C.F. Schmidt [Rivista]. - [s.l.] : Rev. Sci. Instrum., 2003. - 3246 : Vol. 74.

Petersen N. O., W. B. McConnaughey, and E. L. Elson Dependence of locally measured cellular deformability on position on the cell , temeprature and cytocalcin B [Rivista]. - [s.l.] : Proc. Natl. Acad. Sci. USA. , 1982. - 5327-5331 : Vol. 79.

Petka W.A., J.L. Harden, K.P. McGrath, D. Wirtz, and D.A. Tirrell Reversible hydrogels from self-assembling artificial proteins [Rivista]. - [s.l.] : Science, 1998. - 389-392 : Vol. 281.

Plamer A., T.G. Mason, J. Xu, S.C. Kuo, D. Wirtz Diffusing wave spectroscopy microrheology of actin filament network [Rivista]. - [s.l.] : Biophys. J., 1999. - 1063-1071 : Vol. 76.

R.G. Larson The Structure and Rheology of Complex Fluids [Rivista]. - [s.l.] : Oxford University Press, 1999.

Radmacher M., M. Fritz, C. M. Kacher, J. P. Cleveland, and P. K. Measuring the viscoelastic properties of human platelets [Rivista]. - [s.l.] : Biophys. J. , 1996. - 556-567 : Vol. 70.

Rahman A. Correlations in the motion of atoms in liquid nitrogen [Rivista]. - [s.l.] : Phys. Rev., 1964. - A405-A411 : Vol. Vol.136..

Ratneshwar L. and Scott A. J. Bilogical application of atomic force microscopy [Rivista]. - [s.l.] : Am J Physiol Cell Physiol, 1994. - C1-21 : Vol. 266 (1).

Reicherter M, Haist T, Wagemann E and Tiziani H Optical particle trapping with computer-generated holograms written on a liquid-crystal display [Rivista]. - [s.l.] : Opt. Lett., 1999. - 608-610 : Vol. 24.

Reicherter M., T. Haist, E.U. Wagemann, and H.J. Tiziani. Optical particle trapping with computer-generated holograms written on a liquid-crystal display. [Rivista]. - [s.l.] : Opt. Lett., 1999. - 608-610 : Vol. 24.

S. K. Mohanty A. Uppal, and P. K. Gupta Self-rotation of red blood cells in optical tweezers: prospects for high throughput malaria diagnosis [Rivista]. - [s.l.] : Biotechnol. Lett. , 2004. - 971-974 : Vol. 26.

Savin T. Doyle, P. S. Static and Dynamic Errors in Particle Tracking Microrheology [Rivista]. - [s.l.] : Biophysical Journal. , 2005. - 623-638 : Vol. 88.

Sbalzarini I.F., and P. Koumoutsakos Feature point tracking and trajectory analysis for video imaging in cell biology [Rivista]. - [s.l.] : J. Struct. Biol., 2005. - 182-95 : Vol. 151.

Schmidt C. E., A. F. Horwitz, D. A. Lauffenburger, and M. P. Sheetz. Integrin-cytoskeletal interactions in migrating fibroblasts are dynamic, [Rivista]. - [s.l.] : J. Cell Biol., 1993. - 977–991 : Vol. 123.

Schnurr B., F. Gittes, F.C. MacKintosh, and C.F. Schmidt [Rivista]. - [s.l.] : Macromolecules, 1997. - 7781 : Vol. 30.

Schroeder T.E., and S.A. Stricker Morphological changes during maturation of starfis oocytes: surface ultra structure and cortical actin [Rivista]. - [s.l.] : Develop. Biol., 1983. - 373-384 : Vol. 98.

Shewry P.R., Tatham A.S. The prolamin storage proteins of cereal seeds: Structure and evolution [Rivista]. - [s.l.] : Biochem J, 1990. - 1-12 : Vol. 267.

Solomon Lu Q. and M. J. [Rivista]. - [s.l.] : Phys. Rev. E, 2002. - 061504 : Vol. 66.

Strick T.R., M.N. Dessinger, G. Charvin, N.H. Dekker, J:F: Allemand, nD. Bensimon, and V. Croquette Stetching of macromolecules and protein [Rivista]. - [s.l.] : Rep. Prog. Phys., 2003. - 1-45 : Vol. 66.

Svoboda K., and S.M. Block Biological applications of optical forces [Rivista]. - [s.l.] : Annu. Rev. Biophys. Biomol. Struct., 1994. - 247-285 : Vol. 23.

Svoboda K., C. F. Schmidt, D. Branton, and S. M. Block Conformation and elasticity of the isolated red blood cell membrane skeleton [Rivista]. - [s.l.] : Biophys. J., 1992. - 784-793 : Vol. 63.

Tao Q., Yokota C., Puck H., Kofron M., Birsoy B., Yan D., Asashima M., Wylie C.C. and Heasman J. Maternal Wnt11 Activates the Canonical Wnt Signaling Pathway required for Axis Formation in Xenopus Embryos [Rivista]. - [s.l.] : Cell, 2005. - 857-871 : Vol. 120.

Tatham A.S. , N.H. THOMSON, T.J. MCMASTER, A.D.L. HUMPHRIS, M. J. MILES, P.R. SHEWRY Scanning Probe Microscopy Studies of Cereal Seed Storage Protein structures [Rivista]. - [s.l.] : Scanning, 1999. - 293-298 : Vol. 21.

Tatham A.S., Shewry P.R. The S-poor prolamins of wheat, barley and rye [Rivista]. - [s.l.] : J. Cereal Sci, 1995. - 1-16 : Vol. 22.

Thoumine O., and A. Ott. Time scale dependent viscoelastic and [Rivista]. - [s.l.] : J. Cell Sci., 1997. - 2109-2116 : Vol. 110.

Tormen M., Carpentiero, A., Vaccari, L., Altissimo, M., Ferrari, E., Cojoc, D. and Di Fabrizio, E. Fabrication of three-dimensional stamps for embossing techniques by lithographically controlled isotropic wet etching. [Rivista]. - [s.l.] : Journal of Vaccum Science and Technology B, 2005. - 2920-2924 : Vol. 23(6).

Tseng Y. and D. Wirtz, [Rivista]. - [s.l.] : Biophys. J., 2001. - 1643-1656 : Vol. 81.

Tseng Y., and D. Wirtz Mechanics and multiple particle traching microeterogeneity of alpha-actinin-cross-linked actin filament networks [Rivista]. - [s.l.] : Biophys.J., 2001. - 1643-1656 : Vol. 81.

Tseng Y., T.P. Kole, D. Wirtz Micromechanical mapping of live cells bu Multiple-Particle Tracking microrheology [Rivista]. - [s.l.] : Biophys. J., 2002. - 3162-3176 : Vol. 83.

Valberg P. A., and D. F. Albertini Cytoplasmic motions, rheology, [Rivista]. - [s.l.] : J. Cell Biol., 1985. - 130-140 : Vol. 101.

Valberg P.A., and H.A. Feldman Magnetic particle motions within living cells. Measurements of cytoplamsic viscosity and motile activity. [Rivista]. - [s.l.] : Biophys. J. , 1987. - 551-561 : Vol. 52.

Valdberg P.A., and J.P. Butler Magnetic particle motions within living cells. Physical theroy and techniques [Rivista]. - [s.l.] : Biophys. J., 1987. - 537-550 : Vol. 52.

Valentine M.T., P.D. Kaplan, D. Thota, J.C. Crocker, T. Gisler, R.K. Prud'homme, M. Beck and D.A. Weitz Investigating the microenvironements ofinhomogeneous soft materials with multiple particle tracking [Rivista]. - [s.l.] : Phys. Rev. E, 2001. - 061506 : Vol. 64.

Valentine M.T., Z.E. Perlman, M.L. Gardel, J.H. Shin, P. Matsudaira, T.J. Mitchison, D.A. Weitz Colloid surface chemistry critical affect multiple particle tracking measurements of biomaterials [Rivista]. - [s.l.] : Biophys. J., 2004. - 4004-4014 : Vol. 84.

Valentine M.Y., Z.E. Perlman, T.J. Mitchison, D.A. Weitz Mechanical proprerties of Xenopus egg cytoplasmic extracts [Rivista]. - [s.l.] : Biophys. J., 2005. - 680-689 : Vol. 88.

Vansteenkiste S. O. [et al.] [Rivista]. - [s.l.] : Prog. Surf. Sci., 1998. - 95–136 : Vol. 57.

Wagner O., J. Zinke, P. Dancker, W. Grill, and J. Bereiter-Hahn Viscoelastic properties of f-actin, microtubules, f-actin/alfa-actinin, and f-actin/Hexokinase determined in microliter volumes with anovel nondestructive method [Rivista]. - [s.l.] : Biophys. J., 1999. - 2784-2796 : Vol. 76.

Waigh T.A. Microrheology of complex fluids [Rivista]. - [s.l.] : Rep. Prog. Phys., 2005. - 685-742 : Vol. 68.

Wang N., J. P. Butler, and D. E. Ingber. Mechanotransduction [Rivista]. - [s.l.] : Science, 1993. - 1124-1127 : Vol. 260.

Wang Y.Y., S.K. Lai, J.S. Suk, A. Pace, R. Cone, and J. Hanes Addressing the PEG mucoadhesivity paradox to engineer nanoparticles that slip through the human mucus barrier [Rivista]. - [s.l.] : Angew. Che. Int. Ed., 2008. - 1-5 : Vol. 47.

Weihs D., T.G. Mason, M.A. Teittell Bio-microrheology: a frontier in micorrheology [Rivista]. - [s.l.] : Biophys. J., 2006. - 4296-4305 : Vol. 91.

Wilding M, Carotenuto R, Infante V, Dale B, Marino M, Di Matteo L, Campanella C. Confocal Analysis of the Activity of mitochondria contained within the 'mitochondrial cloud' during oogenesis of Xenopus laevis [Rivista]. - [s.l.] : Zygote, 2001. - 347-351 : Vol. 9.

Yamada S., D. Wirtz, S. Kuo Mechanics of living cells measured by laser tracking microrheology [Rivista]. - [s.l.] : Biophys. J., 2000. - 1736-1747 : Vol. 78.

Yang H., Y. Wang, S. Lai, H. An, Y. Li, F. Chen Application of Atomic Force Microscopy as a Nanotechnology Tool in Food Science [Rivista]. - [s.l.] : JOURNAL OF FOOD SCIENCE, 2007. - 4 : Vol. 72.

Yisraeli J., Sokol S. and Melton D.A. A two-step model for the localization of maternal mRNA in Xenopus oocytes: involvement of microtubules and microfilaments in the translocation and anchoring of Vg1 RNA [Rivista]. - [s.l.] : Development, 1990. - 289-298 : Vol. 108.

Yokokawa M., Yoshimura S., Takeyasu K. The observation of biological samples by atomic force microscopy [Rivista]. - [s.l.] : Protein, Nucleic Acid and Enzyme, 2004. - 11: 1607-1614 : Vol. 49.

Ziemann F., J. Radler and E. Sackmann Local measurements of viscoleastic moduli of entangled actin network using an oscillating magnetic bead micro-rheometer [Rivista]. - [s.l.] : Biophys. J., 1994. - 2210-2216 : Vol. 66.

List of publications

- **"Spectroscopical and mechanical characterization of normal and thalassemic red blood cells by Raman Tweezers."**

  Anna Chiara De Luca, Giulia Rusciano, Rosanna Ciancia, Vincenzo Martinelli, Giuseppe Pesce, Bruno Rotoli, Lara Selvaggi, and Antonio Sasso

  Optics Express, Vol. 16, Issue 11, pp. 7943-7957 (2008)

- **"Mechanical changes of living oocytes at maturation investigated by multiple particle tracking."**

  Pesce, Giuseppe; Selvaggi, Lara; Caporali, Antonio; de Luca, Anna Chiara; Puppo, Agostina; Rusciano, Giulia; Sasso, Antonio

  Applied Physics Letters, Volume 95, Issue 9, (2009)

- **"Optimized multi-view imaging improves the observation of optically manipulated non-spherical particles."**

  L. Selvaggi, E. Ferrari, A.R. Moradi, S.C. Santucci, P. Beuzer and D. Cojoc

  Journal of Optics, under submission.

- **"Multiple Particle Tracking to investigate viscoelastic properties in living cells."**

  Lara Selvaggi, Rosa Carotenuto, Carmen Vaccaro, Antonio Sasso, Chiara Campanella

  Methods in cell biology (book), Elsevier. Under submission.